

Measurement of the CKM angle γ using $B_s^0 \rightarrow D_s K \pi\pi$ decays

P. d'Argent¹, E. Gersabeck², M. Kecke¹, M. Schiller³

¹*Physikalisches Institut, Ruprecht-Karls-Universität Heidelberg, Heidelberg, Germany*

²*School of Physics and Astronomy, University of Manchester, Manchester, United Kingdom*

³*School of Physics and Astronomy, University of Glasgow, Glasgow, United Kingdom*

Abstract

We present the first measurement of the weak phase $2\beta + \gamma$ obtained from a time-dependent (amplitude) analysis of $B_s^0 \rightarrow D_s K \pi\pi$ decays using proton-proton collision data corresponding to an integrated luminosity of **xxx** fb⁻¹ recorded by the LHCb detector.

Contents

| | | |
|----------|---|-----------|
| 1 | Introduction | 1 |
| 2 | Formalism | 2 |
| 2.1 | Decay rates and CP-observables | 2 |
| 2.2 | Amplitude model | 3 |
| 2.2.1 | Form Factors and Resonance Lineshapes | 4 |
| 2.2.2 | Spin Densities | 5 |
| 2.3 | Validation | 8 |
| 3 | Data samples and event selection | 12 |
| 3.1 | Stripping and Trigger selection | 12 |
| 3.2 | Offline selection | 12 |
| 3.2.1 | Physics background vetoes | 13 |
| 3.2.2 | Training of multivariate classifier | 14 |
| 3.2.3 | Final selection | 14 |
| 3.3 | Simulation | 15 |
| 4 | Fits to invariant mass distributions of signal and normalization channel | 17 |
| 4.1 | Signal models for $m(D_s\pi\pi\pi)$ and $m(D_sK\pi\pi)$ | 17 |
| 4.2 | Background models for $m(D_s\pi\pi\pi)$ | 18 |
| 4.3 | Background models for $m(D_sK\pi\pi)$ | 18 |
| 4.4 | Fit to $B_s^0 \rightarrow D_s\pi\pi\pi$ candidates | 20 |
| 4.5 | Fit to $B_s^0 \rightarrow D_sK\pi\pi$ candidates | 20 |
| 4.6 | Extraction of signal weights | 20 |
| 5 | Flavour Tagging | 22 |
| 5.1 | OS tagging calibration | 23 |
| 5.2 | SS tagging calibration | 23 |
| 5.3 | Tagging performance comparison between the signal and normalization channel | 23 |
| 5.4 | Combination of OS and SS taggers | 24 |
| 6 | Acceptance | 27 |
| 6.1 | MC corrections | 27 |
| 6.1.1 | Truth matching of simulated candidates | 27 |
| 6.1.2 | PID efficiencies | 28 |
| 6.1.3 | BDT efficiencies | 29 |
| 6.1.4 | Tracking efficiencies | 30 |
| 6.2 | Decay-time acceptance | 31 |
| 6.2.1 | Comparison of acceptance in subsamples | 32 |
| 6.2.2 | Results | 34 |
| 6.3 | Phasespace acceptance | 38 |

| | |
|--|-----------|
| 7 Decay-time Resolution | 39 |
| 7.1 Calibration for Run-I data | 40 |
| 7.2 Calibration for Run-II data | 41 |
| 7.3 Cross-checks | 44 |
| 7.3.1 Kinematic dependence | 44 |
| 7.3.2 DTF constraints | 44 |
| 8 Production and Detection Asymmetries | 45 |
| 8.1 B_s Production Asymmetry | 45 |
| 8.2 $K^-\pi^+$ Detection Asymmetry | 46 |
| 9 Time dependent fit | 49 |
| 9.1 sFit to $B_s^0 \rightarrow D_s \pi\pi\pi$ data | 49 |
| 9.2 sFit to $B_s^0 \rightarrow D_s K\pi\pi$ data | 52 |
| 10 Time dependent amplitude fit | 53 |
| 10.1 Signal Model Construction | 53 |
| 10.2 Results | 54 |
| A Stripping and Trigger cuts | 56 |
| B Details of multivariate classifier | 57 |
| C Detailed mass fits | 59 |
| D Decay-time Resolution fits | 63 |
| E Spin Amplitudes | 67 |
| F Considered Decay Chains | 68 |
| G MC corrections | 69 |
| H Data distributions | 74 |
| H.1 Comparison of signal and calibration channel | 74 |
| H.2 Comparison of Run-I and Run-II data | 76 |
| H.3 Comparison of D_s final states | 78 |
| H.4 Comparison of trigger categories | 80 |
| H.5 Comparison of B_s and B_d decays | 82 |
| References | 83 |

1 Introduction

The weak phase γ is the least well known angle of the CKM unitary triangle. A key channel to measure γ is the time-dependent analysis of $B_s^0 \rightarrow D_s K$ decays [1, 2]. To measure the weak CKM phase $\gamma \equiv \arg[-(V_{ud}V_{ub}^*)/(V_{cd}V_{cb}^*)]$, a decay with interference between $b \rightarrow c$ and $b \rightarrow u$ transitions is needed [1]. This note present the first measurement of γ using $B_s^0 \rightarrow D_s K\pi\pi$ decays, where the $K\pi\pi$ subsystem is dominated by excited kaon states such as the $K_1(1270)$ and $K_1(1400)$ resonances. To account for the non-constant strong phase across the phasespace, one can either perform a time-dependent amplitude fit or select a suitable phase-space region and introduce a coherence factor as additional hadronic parameter to the fit. This analysis is based on the first observation of the $B_s^0 \rightarrow D_s K\pi\pi$ decay by LHCb [3, 4], where the branching ratio is measured relative to $B_s^0 \rightarrow D_s \pi\pi\pi$.

12 2 Formalism

13 2.1 Decay rates and CP-observables

14 In the following, we choose a convention in which $\Delta\Gamma_s = \Gamma_L - \Gamma_H < 0$ and $\Delta m_s =$
 15 $m_H - m_L > 0$, where the indices H and L refer to the heavy and light mass eigenstates
 16 of the B_s meson. We assume $|q/p| = 1$ for the complex coefficients p and q which relate
 17 the B_s meson mass eigenstates to the flavour eigenstates.

$$A(B_s^0 \rightarrow D_s^- K^+ \pi\pi) \equiv A(x) = \sum_i a_i A_i(x) \quad (2.1)$$

$$A(B_s^0 \rightarrow D_s^+ K^- \pi\pi) \equiv \bar{A}(\bar{x}) = \sum_i \bar{a}_i \bar{A}_i(\bar{x}) \quad (2.2)$$

$$A(\bar{B}_s^0 \rightarrow D_s^- K^+ \pi\pi) = \bar{A}(x) \text{ (Assuming no direct CPV)} \quad (2.3)$$

$$A(\bar{B}_s^0 \rightarrow D_s^+ K^- \pi\pi) = A(\bar{x}) \text{ (Assuming no direct CPV)} \quad (2.4)$$

18 The full time-dependent amplitude pdf is given by:

$$\begin{aligned} P(x, t, q_t, q_f) \propto & [(|A(x)|^2 + |\bar{A}(x)|^2) \cosh\left(\frac{\Delta\Gamma t}{2}\right) \\ & + q_t q_f (|A(x)|^2 - |\bar{A}(x)|^2) \cos(m_s t) \\ & - 2\text{Re}(A(x)^* \bar{A}(x) e^{-iq_f(\gamma-2\beta_s)}) \sinh\left(\frac{\Delta\Gamma t}{2}\right) \\ & - 2q_t q_f \text{Im}(A(x)^* \bar{A}(x) e^{-iq_f(\gamma-2\beta_s)}) \sin(m_s t)] e^{-\Gamma t} \end{aligned} \quad (2.5)$$

19 where $q_t = +1, -1, 0$ for events tagged as B_s^0 , \bar{B}_s^0 or untagged events and $q_f = +1$ (-1) for
 20 $D_s^- K^+ \pi\pi$ ($D_s^+ K^- \pi\pi$) final states. Integrating over the phasespace, we get

$$\int P(x, t, q_t, q_f) dx \propto [\cosh\left(\frac{\Delta\Gamma t}{2}\right) + q_t q_f C \cos(m_s t) + \kappa D_{q_f} \sinh\left(\frac{\Delta\Gamma t}{2}\right) - q_t \kappa S_{q_f} \sin(m_s t)] e^{-\Gamma t} \quad (2.6)$$

21 where the same convention for the CP coefficients as for the $B_s \rightarrow D_s K$ analysis is used:

$$C = \frac{1 - r^2}{1 + r^2} \quad (2.7)$$

$$D_{q_f} = -\frac{2r \cos(\delta - q_f(\gamma - 2\beta_s))}{1 + r^2} \quad (2.8)$$

$$S_{q_f} = q_f \frac{2r \sin(\delta - q_f(\gamma - 2\beta_s))}{1 + r^2} \quad (2.9)$$

22 The coherence factor κ , the strong phase difference δ and the ratio of the suppressed
 23 ($b \rightarrow u$) over favored ($b \rightarrow c$) decay mode are defined as:

$$\kappa e^{i\delta} \equiv \frac{\int A(x)^* \bar{A}(x) dx}{\sqrt{\int |A(x)|^2 dx} \sqrt{\int |\bar{A}(x)|^2 dx}} \quad (2.10)$$

$$r \equiv \frac{\sqrt{\int |\bar{A}(x)|^2 dx}}{\sqrt{\int |A(x)|^2 dx}}. \quad (2.11)$$

²⁴ In the limit of only one contributing resonance $\kappa \rightarrow 1$.

²⁵

²⁶ 2.2 Amplitude model

²⁷ The differential decay rate of a B_s meson with mass, m_{B_s} , decaying into four pseudoscalar
²⁸ particles with four-momenta $p_i = (E_i, \vec{p}_i)$ ($i = 1, 2, 3, 4$) is given by

$$d\Gamma = \frac{1}{2m_{B_s}} |A(\mathbf{x})|^2 d\Phi_4, \quad (2.12)$$

²⁹ where the transition amplitude $A(\mathbf{x})$, describes the dynamics of the interaction, $d\Phi_4$
³⁰ is the four-body phase space element [5], and \mathbf{x} represents a unique set of kinematic
³¹ conditions within the phase space of the decay. Each final state particle contributes three
³² observables, manifesting in their three-momentum, summing up to twelve observables in
³³ total. Four of them are redundant due to four-momentum conservation and the overall
³⁴ orientation of the system can be integrated out. The remaining five independent degrees
³⁵ of freedom unambiguously determine the kinematics of the decay. Convenient choices
³⁶ for the kinematic observables include the invariant mass combinations of the final state
³⁷ particles

$$\begin{aligned} m_{ij}^2 &= (p_i + p_j)^2, \\ m_{ijk}^2 &= (p_i + p_j + p_k)^2 \end{aligned} \quad (2.13)$$

³⁸ or acoplanarity and helicity angles. It is however important to take into account that,
³⁹ while m_{12}^2, m_{23}^2 are sufficient to fully describe a three-body decay, the obvious extension
⁴⁰ to four-body decays with m_{ij}^2, m_{ijk}^2 requires additional care, as these variables alone are
⁴¹ insufficient to describe the parity-odd moments possible in four-body kinematics.

⁴² In practice, we do not need to choose a particular five-dimensional basis, but use the
⁴³ full four-vectors of the decay in our analysis. The dimensionality is handled by the phase
⁴⁴ space element which can be written in terms of any set of five independent kinematic
⁴⁵ observables, $\mathbf{x} = (x_1, \dots, x_5)$, as

$$d\Phi_4 = \phi_4(\mathbf{x}) d^5x, \quad (2.14)$$

⁴⁶ where $\phi_4(\mathbf{x}) = \left| \frac{\partial \Phi_4}{\partial(x_1, \dots, x_5)} \right|$ is the phase space density. In contrast to three-body decays,
⁴⁷ the four-body phase space density function is not flat in the usual kinematic variables.
⁴⁸ Therefore, an analytic expression for ϕ_4 is taken from Ref. [6].

⁴⁹ The total amplitude for the $B_s \rightarrow h_1 h_2 h_3 h_4$ decay is given by the coherent sum
⁵⁰ over all intermediate state amplitudes $A_i(\mathbf{x})$, each weighted by a complex coefficient
⁵¹ $a_i = |a_i| e^{i\phi_i}$ to be measured from data,

$$A(\mathbf{x}) = \sum_i a_i A_i(\mathbf{x}). \quad (2.15)$$

⁵² To construct $A_i(\mathbf{x})$, the isobar approach is used, which assumes that the decay process
⁵³ can be factorized into subsequent two-body decay amplitudes [7–9]. This gives rise to
⁵⁴ two different decay topologies; quasi two-body decays $B_s \rightarrow (R_1 \rightarrow h_1 h_2) (R_2 \rightarrow h_3 h_4)$

55 or cascade decays $B_s \rightarrow h_1$ [$R_1 \rightarrow h_2$ ($R_2 \rightarrow h_3 h_4$)]. In either case, the intermediate state
 56 amplitude is parameterized as a product of form factors B_L , included for each vertex
 57 of the decay tree, Breit-Wigner propagators T_R , included for each resonance R , and an
 58 overall angular distribution represented by a spin factor S ,

$$A_i(\mathbf{x}) = B_{L_{B_s}}(\mathbf{x}) [B_{L_{R_1}}(\mathbf{x}) T_{R_1}(\mathbf{x})] [B_{L_{R_2}}(\mathbf{x}) T_{R_2}(\mathbf{x})] S_i(\mathbf{x}). \quad (2.16)$$

59 2.2.1 Form Factors and Resonance Lineshapes

60 To account for the finite size of the decaying resonances, the Blatt-Weisskopf penetration
 61 factors, derived in Ref. [10] by assuming a square well interaction potential with radius
 62 r_{BW} , are used as form factors, B_L . They depend on the breakup momentum q , and the
 63 orbital angular momentum L , between the resonance daughters. Their explicit expressions
 64 are

$$\begin{aligned} B_0(q) &= 1, \\ B_1(q) &= 1/\sqrt{1 + (q r_{\text{BW}})^2}, \\ B_2(q) &= 1/\sqrt{9 + 3(q r_{\text{BW}})^2 + (q r_{\text{BW}})^4}. \end{aligned} \quad (2.17)$$

65 Resonance lineshapes are described as function of the energy-squared, s , by Breit-Wigner
 66 propagators

$$T(s) = \frac{1}{M^2(s) - s - i m_0 \Gamma(s)}, \quad (2.18)$$

67 featuring the energy-dependent mass $M(s)$ (defined below), and total width, $\Gamma(s)$. The
 68 latter is normalized to give the nominal width, Γ_0 , when evaluated at the nominal mass
 69 m_0 , *i.e.* $\Gamma_0 = \Gamma(s = m_0^2)$.

70 For a decay into two stable particles $R \rightarrow AB$, the energy dependence of the decay
 71 width can be described by

$$\Gamma_{R \rightarrow AB}^{(2)}(s) = \Gamma_0 \frac{m_0}{\sqrt{s}} \left(\frac{q}{q_0} \right)^{2L+1} \frac{B_L(q)^2}{B_L(q_0)^2}, \quad (2.19)$$

72 where q_0 is the value of the breakup momentum at the resonance pole [11].

73 The energy-dependent width for a three-body decay $R \rightarrow ABC$, on the other hand, is
 74 considerably more complicated and has no analytic expression in general. However, it can
 75 be obtained numerically by integrating the transition amplitude-squared over the phase
 76 space,

$$\Gamma_{R \rightarrow ABC}^{(3)}(s) = \frac{1}{2\sqrt{s}} \int |A_{R \rightarrow ABC}|^2 d\Phi_3, \quad (2.20)$$

77 and therefore requires knowledge of the resonant substructure. The three-body amplitude
 78 $A_{R \rightarrow ABC}$ can be parameterized similarly to the four-body amplitude in Eq. (2.16). In
 79 particular, it includes form factors and propagators of intermediate two-body resonances.

80 Both Eq. (2.19) and Eq. (2.20) give only the partial width for the decay into a specific
 81 channel. To obtain the total width, a sum over all possible decay channels has to be
 82 performed,

$$\Gamma(s) = \sum_i g_i \Gamma_i(s), \quad (2.21)$$

83 where the coupling strength to channel i , is given by g_i . Branching fractions \mathcal{B}_i are related
 84 to the couplings g_i via the equation [12]

$$\mathcal{B}_i = \int_{s_{min}}^{\infty} \frac{g_i m_0 \Gamma_i(s)}{|M^2(s) - s - i m_0 \sum_j g_j \Gamma_j(s)|^2} ds. \quad (2.22)$$

85 As experimental values are usually only available for the branching fractions, Eq. (2.22)
 86 needs to be inverted to obtain values for the couplings. In practice, this is solved by
 87 minimizing the quantity $\chi^2(g) = \sum_i [\mathcal{B}_i - \mathcal{I}_i(g)]^2 / \Delta \mathcal{B}_i^2$, where $\mathcal{I}_i(g)$ denotes the right-
 88 hand side of Eq. (2.22).

89 The treatment of the lineshape for various resonances considered in this analysis is
 90 described in what follows. The nominal masses and widths of the resonances are taken
 91 from the PDG [12] with the exceptions described below.

92 For the broad scalar resonance σ , the model from Bugg is used [13]. Besides $\sigma \rightarrow \pi\pi$
 93 decays, it includes contributions from the decay modes $\sigma \rightarrow KK$, $\sigma \rightarrow \eta\eta$ and $\sigma \rightarrow \pi\pi\pi\pi$
 94 as well as dispersive effects due to the channel opening of the latter. We use the Gournaris-
 95 Sakurai parametrization for the $\rho(770)^0 \rightarrow \pi\pi$ propagator which provides an analytical
 96 description of the dispersive term, $M^2(s)$ [14]. The energy-dependent width of the $f_0(980)$
 97 resonance is given by the sum of the partial widths into the $\pi\pi$ and KK channels [15],

$$\Gamma_{f_0(980)}(s) = g_{\pi\pi} \Gamma_{f_0(980) \rightarrow \pi\pi}^{(2)}(s) + g_{KK} \Gamma_{f_0(980) \rightarrow KK}^{(2)}(s), \quad (2.23)$$

98 where the coupling constants $g_{\pi\pi}$ and g_{KK} , as well as the mass and width are taken from
 99 a measurement performed by the BES Collaboration [16]. The total decay widths for
 100 both the $f_2(1270)$ and the $f_0(1370)$ meson take the channels $\pi\pi$, KK , $\eta\eta$ and $\pi\pi\pi\pi$ into
 101 account. While the two-body partial widths are described by Eq. (2.19), a model for
 102 the partial width for a decay into four pions is taken from Ref. [17]. The corresponding
 103 branching fractions are taken from the PDG [12]. The nominal mass and width of the
 104 $f_0(1370)$ resonance are taken from an LHCb measurement [18]. Equation (2.19) is used
 105 for all other resonances decaying into a two-body final state.

106 Some particles may not originate from a resonance but are in a state of relative orbital
 107 angular momentum. We denote such non-resonant states by surrounding the particle
 108 system with brackets and indicate the partial wave state with an subscript; for example
 109 $(\pi\pi)_S$ refers to a non-resonant di-pion S -wave. The lineshape for non-resonant states is
 110 set to unity.

111 2.2.2 Spin Densities

112 The spin amplitudes are phenomenological descriptions of decay processes that are required
 113 to be Lorentz invariant, compatible with angular momentum conservation and, where
 114 appropriate, parity conservation. They are constructed in the covariant Zemach (Rarita-
 115 Schwinger) tensor formalism [19–21]. At this point, we briefly introduce the fundamental
 116 objects of the covariant tensor formalism which connect the particle’s four-momenta to
 117 the spin dynamics of the reaction and give a general recipe to calculate the spin factors
 118 for arbitrary decay trees. Further details can be found in Refs. [22, 23].

119 A spin- S particle with four-momentum p , and spin projection λ , is represented by the
 120 polarization tensor $\epsilon_{(S)}(p, \lambda)$, which is symmetric, traceless and orthogonal to p . These
 121 so-called Rarita-Schwinger conditions reduce the a priori 4^S elements of the rank- S tensor

122 to $2S + 1$ independent elements in accordance with the number of degrees of freedom of a
123 spin- S state [20, 24].

124 The spin projection operator $P_{(S)}^{\mu_1 \dots \mu_S \nu_1 \dots \nu_S}(p_R)$, for a resonance R , with spin $S =$
125 $\{0, 1, 2\}$, and four-momentum p_R , is given by [23]:

$$\begin{aligned} P_{(0)}^{\mu\nu}(p_R) &= 1 \\ P_{(1)}^{\mu\nu}(p_R) &= -g^{\mu\nu} + \frac{p_R^\mu p_R^\nu}{p_R^2} \\ P_{(2)}^{\mu\nu\alpha\beta}(p_R) &= \frac{1}{2} \left[P_{(1)}^{\mu\alpha}(p_R) P_{(1)}^{\nu\beta}(p_R) + P_{(1)}^{\mu\beta}(p_R) P_{(1)}^{\nu\alpha}(p_R) \right] - \frac{1}{3} P_{(1)}^{\mu\nu}(p_R) P_{(1)}^{\alpha\beta}(p_R), \end{aligned} \quad (2.24)$$

126 where $g^{\mu\nu}$ is the Minkowski metric. Contracted with an arbitrary tensor, the projection
127 operator selects the part of the tensor which satisfies the Rarita-Schwinger conditions.

128 For a decay process $R \rightarrow AB$, with relative orbital angular momentum L , between
129 particle A and B , the angular momentum tensor is obtained by projecting the rank- L
130 tensor $q_R^{\nu_1} q_R^{\nu_2} \dots q_R^{\nu_L}$, constructed from the relative momenta $q_R = p_A - p_B$, onto the spin- L
131 subspace,

$$L_{(L)\mu_1 \dots \mu_L}(p_R, q_R) = (-1)^L P_{(L)\mu_1 \dots \mu_L \nu_1 \dots \nu_L}(p_R) q_R^{\nu_1} \dots q_R^{\nu_L}. \quad (2.25)$$

132 Their $|\vec{q}_R|^L$ dependence accounts for the influence of the centrifugal barrier on the transition
133 amplitudes. For the sake of brevity, the following notation is introduced,

$$\begin{aligned} \varepsilon_{(S)}(R) &\equiv \varepsilon_{(S)}(p_R, \lambda_R), \\ P_{(S)}(R) &\equiv P_{(S)}(p_R), \\ L_{(L)}(R) &\equiv L_{(L)}(p_R, q_R). \end{aligned} \quad (2.26)$$

134 Following the isobar approach, a four-body decay amplitude is described as a product
135 of two-body decay amplitudes. Each sequential two-body decay $R \rightarrow A B$, with relative
136 orbital angular momentum L_{AB} , and total intrinsic spin S_{AB} , contributes a term to the
137 overall spin factor given by

$$\begin{aligned} S_{R \rightarrow AB}(\mathbf{x}|L_{AB}, S_{AB}; \lambda_R, \lambda_A, \lambda_B) &= \varepsilon_{(S_R)}(R) X(S_R, L_{AB}, S_{AB}) L_{(L_{AB})}(R) \\ &\times \Phi(\mathbf{x}|S_{AB}; \lambda_A, \lambda_B), \end{aligned} \quad (2.27)$$

138 where

$$\Phi(\mathbf{x}|S_{AB}; \lambda_A, \lambda_B) = P_{(S_{AB})}(R) X(S_{AB}, S_A, S_B) \varepsilon_{(S_A)}^*(A) \varepsilon_{(S_B)}^*(B). \quad (2.28)$$

139 Here, a polarization vector is assigned to the decaying particle and the complex conjugate
140 vectors for each decay product. The spin and orbital angular momentum couplings are
141 described by the tensors $P_{(S_{AB})}(R)$ and $L_{(L_{AB})}(R)$, respectively. Firstly, the two spins S_A
142 and S_B , are coupled to a total spin- S_{AB} state, $\Phi(\mathbf{x}|S_{AB})$, by projecting the corresponding
143 polarization vectors onto the spin- S_{AB} subspace transverse to the momentum of the
144 decaying particle. Afterwards, the spin and orbital angular momentum tensors are
145 properly contracted with the polarization vector of the decaying particle to give a Lorentz
146 scalar. This requires in some cases to include the tensor $\varepsilon_{\alpha\beta\gamma\delta} p_R^\delta$ via

$$X(j_a, j_b, j_c) = \begin{cases} 1 & \text{if } j_a + j_b + j_c \text{ even} \\ \varepsilon_{\alpha\beta\gamma\delta} p_R^\delta & \text{if } j_a + j_b + j_c \text{ odd} \end{cases}, \quad (2.29)$$

¹⁴⁷ where $\varepsilon_{\alpha\beta\gamma\delta}$ is the Levi-Civita symbol and j refers to the arguments of X defined in
¹⁴⁸ Eqs. 2.27 and 2.28. Its antisymmetric nature ensures the correct parity transformation
¹⁴⁹ behavior of the amplitude. The spin factor for a whole decay chain, for example $R \rightarrow$
¹⁵⁰ $(R_1 \rightarrow AB)(R_2 \rightarrow CD)$, is obtained by combining the two-body terms and performing a
¹⁵¹ sum over all unobservable, intermediary spin projections

$$\sum_{\lambda_{R_1}, \lambda_{R_2}} S_{R \rightarrow R_1 R_2}(\mathbf{x}|L_{R_1 R_2}; \lambda_{R_1}, \lambda_{R_2}) S_{R_1 \rightarrow AB}(\mathbf{x}|L_{AB}; \lambda_{R_1}) S_{R_2 \rightarrow CD}(\mathbf{x}|L_{CD}; \lambda_{R_2}), \quad (2.30)$$

¹⁵² where $\lambda_R = \lambda_A = \lambda_B = \lambda_C = \lambda_D = 0$, $S_{AB} = S_{CD} = 0$ and $S_{R_1 R_2} = L_{R_1 R_2}$, as only
¹⁵³ pseudoscalar initial/final states are involved.

¹⁵⁴ The spin factors for all decay topologies considered in this analysis are explicitly given
¹⁵⁵ in Appendix E.

156 2.3 Validation

157 The amplitude fit is performed by using the amplitude analysis tool **MINT2**. It was
 158 previously applied to analyze $D^0 \rightarrow 4\pi$ and $D^0 \rightarrow KK\pi\pi$ decays [25] which have an
 159 identical general spin structure (*i.e.* scalar to four scalar decay) then $B_s \rightarrow D_s K\pi\pi$ decays.
 160 In the course of the $D^0 \rightarrow hhhh$ analysis, the implementation of the amplitudes were
 161 extensively cross-checked against other available tool such as **qft++** [26], **AmpGen** [27] and
 162 were possible **EVTGEN** [28]. Since no additional line shapes or spin factors are needed for
 163 this analysis, we consider the amplitude calculation as fully validated.

164 This does, however, not apply to the full time-dependent amplitude pdf which is newly
 165 implemented for this analysis. To cross-check it, we use **EVTGEN** to generate toy events
 166 with time-dependent CP violation according to the **SSD_Cp** event model [28]. Since this
 167 event model does not allow for multiple interfering resonances, we generate only the decay
 168 chain $B_s \rightarrow D_s (K_1(1400) \rightarrow K^*(892)\pi)$. Table 2.1 lists the generated input parameters.
 169 The toy data set is fitted with our **MINT2** implementation of the full time-dependent
 170 amplitude pdf and the phasespace-integrated pdf.

171 The CP coefficients $C, D, \bar{D}, S, \bar{S}$ are the fit parameters in case of the phasespace-
 172 integrated pdf, while the full pdf determines $x_{\pm} = r \cos(\delta \pm (\gamma - 2\beta_s))$ and $y_{\pm} = r \sin(\delta \pm$
 173 $(\gamma - 2\beta_s))$. The fit parameters are converted to the physical observables $r, \kappa, \delta, \gamma$ using
 174 the **GammaCombo** package [29]. As shown in Tab. 2.2, 2.3 and 2.4, the fit results are
 175 in excellent agreement with the generated input values. The 1-CL contours are shown
 176 in Figs. 2.1 and 2.2. The phasespace-integrated fit is, in addition, performed with the
 177 **B2DX** fitter used for the $B_s \rightarrow D_s K$ analysis yielding identical results. Note though that
 178 some parts of the **B2DX** fitter have been taken over to our **MINT2** fitter, such that the
 179 implementations are not fully independent.

Table 2.1: Input values used to generate **EVTGEN** toy events according to the **SSD_Cp** event model.

| | |
|----------------|--------------------------|
| τ | 1.5 ps |
| $\Delta\Gamma$ | -0.1 ps^{-1} |
| Δm_s | 17.757 ps^{-1} |
| r | 0.37 |
| κ | 1 |
| δ | 10.0° |
| γ | 71.1° |
| β_s | 0.0° |

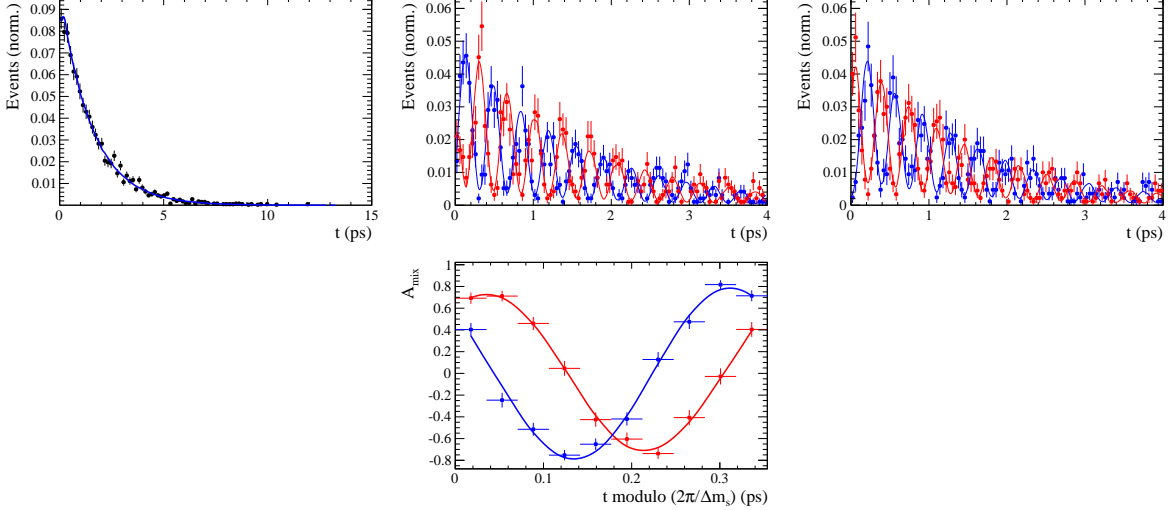


Figure 2.1: Time distribution of $B_s \rightarrow D_s K \pi\pi$ events generated with EVTGEN (points with error bars) and MINT2 fit projections (blue solid line).

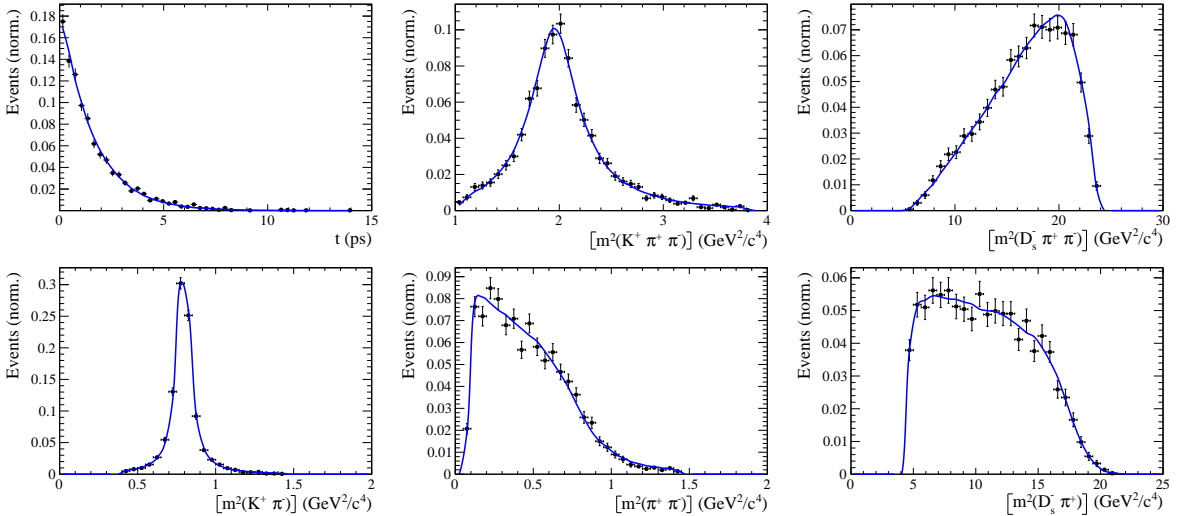


Figure 2.2: Time and invariant mass distributions of $B_s \rightarrow D_s K \pi\pi$ events generated with EVTGEN (points with error bars) and MINT2 fit projections (blue solid line).

Table 2.2: Result of the phasespace-integrated fit to EVTGEN toy events.

| | Generated | Fit result | Pull(σ) |
|-----------|-----------|--------------------|------------------|
| C | 0.759 | 0.763 ± 0.026 | 0.2 |
| D | -0.314 | -0.376 ± 0.227 | -0.3 |
| \bar{D} | -0.101 | -0.261 ± 0.246 | -0.7 |
| S | -0.570 | -0.626 ± 0.035 | 1.6 |
| \bar{S} | -0.643 | -0.669 ± 0.035 | -0.7 |

Table 2.3: Result of the time-dependent amplitude fit to EVTGEN toy events.

| | Generated | Fit result | Pull(σ) |
|-------|-----------|--------------------|------------------|
| x_- | 0.179 | 0.135 ± 0.050 | -0.9 |
| y_- | -0.324 | -0.307 ± 0.022 | 0.8 |
| x_+ | 0.057 | 0.102 ± 0.065 | 0.6 |
| y_+ | 0.366 | 0.394 ± 0.023 | 1.3 |

Table 2.4: Results for the physical observables obtained from fits to EVTGEN toy events.

| | Generated | Full PDF | Phasespace integrated |
|----------|--------------|-------------------|-----------------------|
| r | 0.370 | 0.379 ± 0.021 | 0.379 ± 0.017 |
| κ | 1.0 | 1.0 | 1.000 ± 0.059 |
| δ | 10.0° | 9.0 ± 5.1 | 5.9 ± 6.0 |
| γ | 71.1° | 67.3 ± 5.9 | 75.1 ± 6.9 |

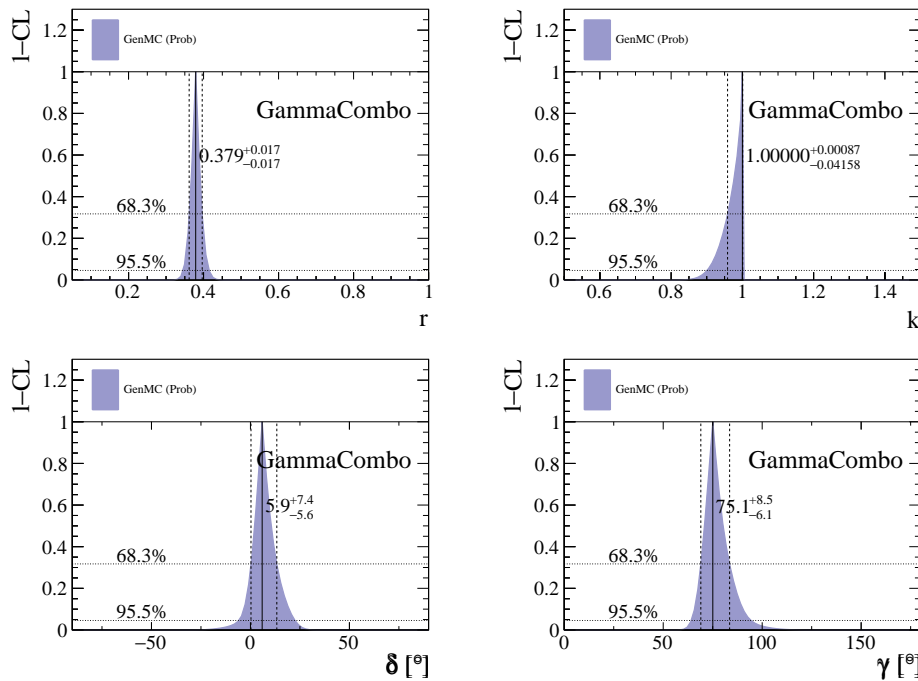


Figure 2.3: The 1-CL contours for the physical observable $r, \kappa, \delta, \gamma$ obtained with the phasespace integrated fit to the EVTGEN toy sample.

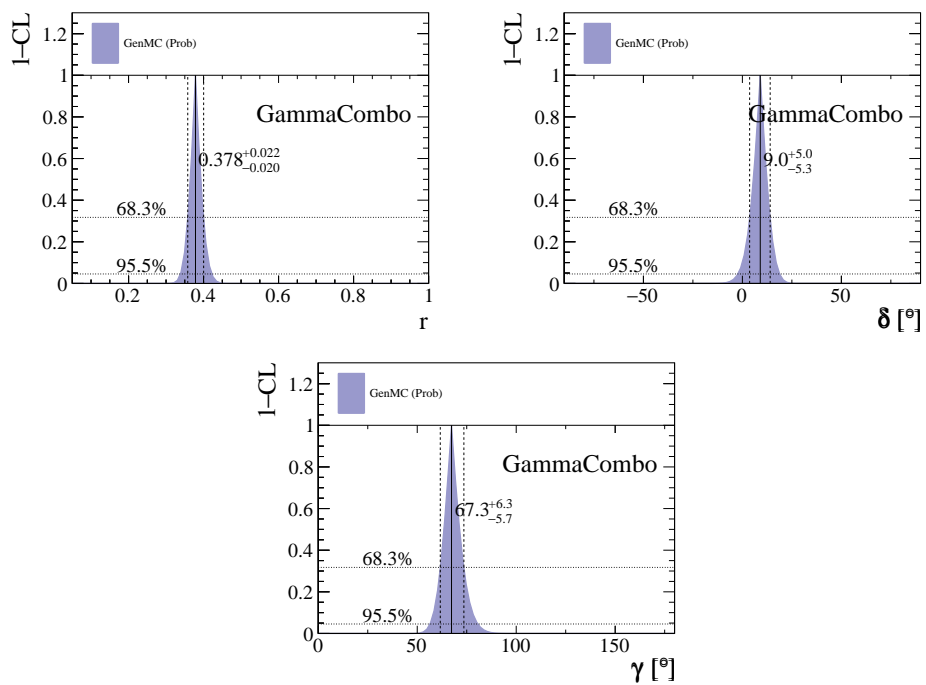


Figure 2.4: The 1-CL contours for the physical observable r, δ, γ obtained with the time-dependent amplitude fit fit to the **EVTGEN** toy sample.

180

3 Data samples and event selection

181

3.1 Stripping and Trigger selection

182 The dataset used for this analysis corresponds to 1 fb^{-1} of proton-proton collision data
183 collected in 2011 with a centre of mass energy $\sqrt{s} = 7 \text{ TeV}$, 2 fb^{-1} collected in 2012 with
184 $\sqrt{s} = 7 \text{ TeV}$ and 2 fb^{-1} collected in 2015/2016 with $\sqrt{s} = 13 \text{ TeV}$. Candidate $B_s^0 \rightarrow D_s K \pi \pi$
185 ($B_s^0 \rightarrow D_s \pi \pi \pi$) decays are reconstructed using the `B02DKPiPiD2HHHPIDBeauty2CharmLine`
186 (`B02DPiPiPiD2HHHPIDBeauty2CharmLine`) line of the `BHadronCompleteEvent` stream of
187 `Stripping21r1` (2011), `Stripping21` (2012), `Stripping24r1` (2015) and `Stripping28r1p1` (2016).
188 Both stripping lines employ the same selection cuts, listed in Appendix A, except for
189 the PID requirement on the bachelor kaon/pion. We reconstruct the $B_s^0 \rightarrow D_s h \pi \pi$ decay
190 through two different final states of the D_s meson, $D_s \rightarrow K K \pi$ and $D_s \rightarrow \pi \pi \pi$. Of those,
191 $D_s \rightarrow K K \pi$ is the most prominent final state, while $\mathcal{BR}(D_s \rightarrow \pi \pi \pi) \approx 0.2 \cdot \mathcal{BR}(D_s \rightarrow$
192 $K K \pi)$ holds for the other one.

193 Events that pass the stripping selection are further required to fulfill the following
194 trigger requirements: at the hardware stage, the B_s^0 candidates are required to be TOS
195 on the `L0Hadron` trigger or TIS on `L0Global`; at Hlt1, B_s^0 candidates are required to be
196 TOS on the `Hlt1TrackAllL0` (`Hlt1TrackMVA` or `Hlt1TwoTrackMVA`) trigger line for Run-I
197 (Run-II) data; at Hlt2, candidates have to be TOS on either one of the 2, 3 or 4-body
198 topological trigger lines or the inclusive ϕ trigger. More details on the used HLT lines are
199 given in Appendix A.

200 Due to a residual kinematic dependence on whether the event is triggered by
201 `L0Hadron` or not and on the data taking condition, the analysis is performed
202 in four disjoint categories: [`Run-I,L0-TOS`], [`Run-I,L0-TIS`], [`Run-II,L0-TOS`] and
203 [`Run-II,L0-TIS`], where for simplicity we denote L0-TOS as `L0Hadron-TOS` and L0-TIS as
204 (`L0Global-TIS` and not `L0Hadron-TOS`).

205

3.2 Offline selection

206 A two-fold approach is used to isolate the $B_s^0 \rightarrow D_s K \pi \pi$ candidates from data passing
207 the stripping line. First, further one-dimensional cuts are applied to reduce the level of
208 combinatorial background and to veto some specific physical background. This stage is
209 specific to the respective final state in which the D_s meson is reconstructed, since different
210 physical backgrounds, depending on the respective final state, have to be taken into
211 account. After that, a multivariate classifier is trained which combines the information
212 of several input variables, including their correlation, into one powerful discriminator
213 between signal and combinatorial background. For this stage, all possible D_s final states
214 are treated equally.

215 In order to clean up the sample and to align the Run-I to the slightly tighter Run-2
216 stripping selection, we apply the following loose cuts to the b hadron:

- 217 • DIRA > 0.99994
- 218 • min IP $\chi^2 < 20$ to any PV,
- 219 • FD $\chi^2 > 100$ to any PV,
- 220 • Vertex $\chi^2/\text{nDoF} < 8$,

221 The most prominent final state used in this analysis is $B_s^0 \rightarrow D_s(\rightarrow KK\pi)K\pi\pi$, where
 222 the D_s decay can either proceed via the narrow ϕ resonance, the broader K^{*0} resonance, or
 223 non resonant. Depending on the decay process being resonant or not, we apply additional
 224 PID requirements on this final state:

225 • resonant case:

- 226 – $D_s^+ \rightarrow \phi\pi^+$, with $|M(K^+K^-) - m_\phi| < 20 \text{ MeV}/c^2$: no additional requirements,
 227 since ϕ is narrow and almost pure K^+K^- .
- 228 – $D_s^+ \rightarrow \bar{K}^{*0}K^+$, with $|M(K^-\pi^+) - m_{K^{*0}}| < 75 \text{ MeV}/c^2$: $\text{DLL}_{K\pi} > 0$ for kaons,
 229 since this resonance is more than ten times broader than ϕ .

230 • non resonant case: $\text{DLL}_{K\pi} > 5$ for kaons, since the non resonant category has
 231 significant charmless contributions.

232 For the $D_s \rightarrow \pi\pi\pi$ final state, we apply global PID requirements:

- 233 • $\text{DLL}_{K\pi} < 10$ for all pions.
- 234 • $\text{DLL}_{p\pi} < 10$ for all pions.

235 3.2.1 Physics background vetoes

236 Additionally, we veto various physical backgrounds, which have either the same final state
 237 as our signal decay, or can contribute via a single misidentification of $K \rightarrow \pi$ or $K \rightarrow p$.
 238 In the following, the vetoes are ordered by the reconstructed D_s final state they apply to:

239 1. All:

- 240 (a) $B_s^0 \rightarrow D_s^+D_s^-$: $|M(K\pi\pi) - m_{D_s}| > 20 \text{ MeV}/c^2$.
- 241 (b) $B_s^0 \rightarrow D_s^-K^+K^-\pi^+$: possible with single missID of $K^- \rightarrow \pi^-$, rejected by
 242 requiring π^- to fulfill $\text{DLL}_{K\pi} < 5$.

243 2. $D_s \rightarrow KK\pi$

- 244 (a) $B^0 \rightarrow D^+(\rightarrow K^+\pi^-\pi^+)K\pi\pi$: possible with single missID of $\pi^+ \rightarrow K^+$, vetoed
 245 by changing particle hypothesis and recompute $|M(K^+\pi^-\pi^+) - m_{D_p}| > 30$
 246 MeV/c^2 , or the K^+ has to fulfill $\text{DLL}_{K\pi} > 10$.
- 247 (b) $\Lambda_b^0 \rightarrow \Lambda_c^+(\rightarrow pK^-\pi^+)K\pi\pi$: possible with single missID of $p \rightarrow K^+$, vetoed by
 248 changing particle hypothesis and recompute $M(pK^-\pi^+) - m_{\Lambda_c^+} > 30 \text{ MeV}/c^2$,
 249 or the K^+ has to fulfill $(\text{DLL}_{K\pi} - \text{DLL}_{p\pi}) > 5$.
- 250 (c) $D^0 \rightarrow KK$: D^0 combined with a random π can fake a $D_s \rightarrow KK\pi$ decay and
 251 be a background to our signal, vetoed by requiring $M(KK) < 1840 \text{ MeV}/c^2$.

252 3. $D_s \rightarrow \pi\pi\pi$

- 253 (a) $D^0 \rightarrow \pi\pi$: combined with a random π can fake a $D_s \rightarrow \pi\pi\pi$ decay and be a
 254 background to our signal, vetoed by requiring both possible combinations to
 255 have $M(\pi\pi) < 1700 \text{ MeV}/c^2$.

256 **3.2.2 Training of multivariate classifier**

257 We use TMVA [30] to train a multivariate discriminator, which is used to further improve
258 the signal to background ratio. The following variables are used for the training:

- 259 ● max(ghostProb) over all tracks
- 260 ● cone(p_T) asymmetry of every track, which is defined to be the difference between the
261 p_T of the π/K and the sum of all other p_T in a cone of radius $r = \sqrt{(\Delta\Phi)^2 + (\Delta\eta)^2}$
262 < 1 rad around the signal π/K track.
- 263 ● min(IP χ^2) over the X_s daughters
- 264 ● max(DOCA) over all pairs of X_s daughters
- 265 ● min(IP χ^2) over the D_s daughters
- 266 ● D_s and B_s^0 DIRA
- 267 ● D_s FD significance
- 268 ● max($\cos(D_s h_i)$), where $\cos(D_s h_i)$ is the cosine of the angle between the D_s and
269 another track i in the plane transverse to the beam
- 270 ● B_s^0 IP χ^2 , FD χ^2 and Vertex χ^2

271 Various classifiers were investigated in order to select the best performing discriminator.
272 Consequently, a boosted decision tree with gradient boost (BDTG) is chosen as nominal
273 classifier. We use truth-matched MC as signal input. Simulated signal candidates are
274 required to pass the same trigger, stripping and preselection requirements, that were used
275 to select the data samples. For the background we use events from the high mass sideband
276 ($m_{B_s^0 \text{ candidate}} > 5600$ MeV/ c^2) of our data samples.

277 The distributions of the input variables for signal and background and the BDTG
278 output distribution are shown in the appendix.

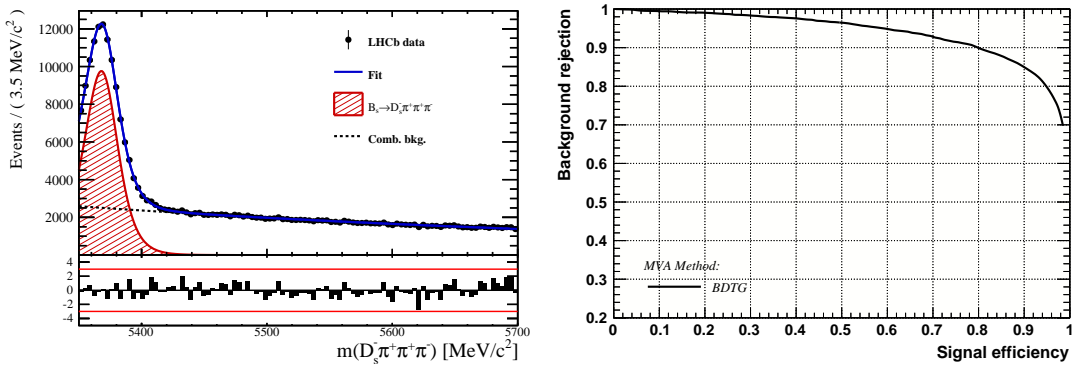


Figure 3.1

279 **3.2.3 Final selection**

Table 3.1: Offline selection requirements for $D_s \rightarrow 3h$ candidates.

| | Description | Requirement |
|------------------------------------|---|---|
| $D_s \rightarrow hh\bar{h}$ | $m(hh\bar{h})$ | $= m_{D_s} \pm 20$ MeV |
| $D_s^- \rightarrow KK\pi^-$ | D^0 veto | $m(KK) < 1840$ MeV |
| $D_s^- \rightarrow \phi\pi^-$ | $m(KK)$ PIDK(K^+) PIDK(K^-) PIDK(π^-) χ_{FD}^2 FD in z D^- veto Λ_c veto | $= m_\phi \pm 20$ MeV > -10 > -10 < 20 > 0 > -1 $m(K^+K_\pi^-\pi^-) \neq m(D^-) \pm 30$ MeV PIDK(K^-) > 0 $m(K^+K_p^-\pi^-) \neq m(\Lambda_c) \pm 30$ MeV PIDK(K^-) – PIDp(K^-) > 0 |
| $D_s^- \rightarrow K^*(892)K^-$ | $m(KK)$ $m(K^+\pi^-)$ PIDK(K^+) PIDK(K^-) PIDK(π^-) χ_{FD}^2 FD in z D^- veto Λ_c veto | $\neq m_\phi \pm 20$ MeV $= m_{K^*(892)} \pm 75$ MeV > -10 > -5 < 10 > 2 > 0 $m(K^+K_\pi^-\pi^-) \neq m(D^-) \pm 30$ MeV PIDK(K^-) > 5 $m(K^+K_p^-\pi^-) \neq m(\Lambda_c) \pm 30$ MeV PIDK(K^-) – PIDp(K^-) > 5 |
| $D_s^- \rightarrow (KK\pi^-)_{NR}$ | $m(KK)$ $m(K^+\pi^-)$ PIDK(K^+) PIDK(K^-) PIDK(π^-) χ_{FD}^2 FD in z D^- veto Λ_c veto | $\neq m_\phi \pm 20$ MeV $\neq m_{K^*(892)} \pm 75$ MeV > 5 > 5 < 10 > 5 > 0 $m(K^+K_\pi^-\pi^-) \neq m(D^-) \pm 30$ MeV PIDK(K^-) > 20 $m(K^+K_p^-\pi^-) \neq m(\Lambda_c) \pm 30$ MeV PIDK(K^-) – PIDp(K^-) > 5 |
| $D_s \rightarrow \pi\pi\pi$ | PIDK(π) PIDp(π) D^0 veto χ_{FD}^2 FD in z | < 10 < 10 $m(\pi^+\pi^-) < 1700$ MeV > 9 > 0 |
| $D_s^- \rightarrow K^-\pi^+\pi^-$ | PIDK(K) PIDK(π) PIDp(π) D^0 veto χ_{FD}^2 FD in z | > 10 < 5 < 10 $m(K^-\pi^+) < 1750$ MeV > 9 > 0 |

3.3 Simulation

Table 3.2: Offline selection requirements for $B_s \rightarrow D_s K\pi\pi(D_s\pi\pi\pi)$ candidates.

| | Description | Requirement |
|-------------------------------------|----------------------------|---|
| $B_s \rightarrow D_s h\pi\pi$ | $m(D_s h\pi\pi)$ | $> 5200 \text{ MeV}$ |
| | χ^2_{vtx}/ndof | < 8 |
| | DIRA | > 0.99994 |
| | χ^2_{FD} | > 100 |
| | χ^2_{IP} | < 20 |
| | χ^2_{DTF}/ndof | < 15 |
| | t | $> 0.4 \text{ ps}$ |
| | δt | $< 0.15 \text{ ps}$ |
| | Phasespace region | $m(h\pi\pi) < 1.95 \text{ GeV}$ $m(h\pi) < 1.2 \text{ GeV}$ $m(\pi\pi) < 1.2 \text{ GeV}$ |
| | Wrong PV veto | $\text{nPV} = 1 \parallel \min(\Delta\chi^2_{IP}) > 20$ |
| $X_s^+ \rightarrow K^+\pi^+\pi^-$ | PIDK(K) | > 10 |
| | PIDK(π^+) | < 10 |
| | PIDK(π^-) | < 5 |
| | Semi.-lep. veto | $\text{isMuon}(K^+) = 0$ |
| | | |
| $X_s^+ \rightarrow \pi^+\pi^+\pi^-$ | PIDK(π^+) | < 5 |
| | PIDK(π^-) | < 10 |
| | Semi.-lep. veto | $\text{isMuon}(\pi^+) = 0$ |

281 **4 Fits to invariant mass distributions of signal and**
 282 **normalization channel**

283 In order to properly model the invariant mass distribution of $B_s^0 \rightarrow D_s K\pi\pi$ and $B_s^0 \rightarrow$
 284 $D_s \pi\pi\pi$ candidates, the expected signal shape, as well as the expected shape for the
 285 combinatorial and physical background has to be known. This model can then be used to
 286 fit the distributions and obtain signal sWeights [31], which are employed to suppress the
 287 residual background that is still left in the sample, for the time-dependent amplitude fit.

288 **4.1 Signal models for $m(D_s \pi\pi\pi)$ and $m(D_s K\pi\pi)$**

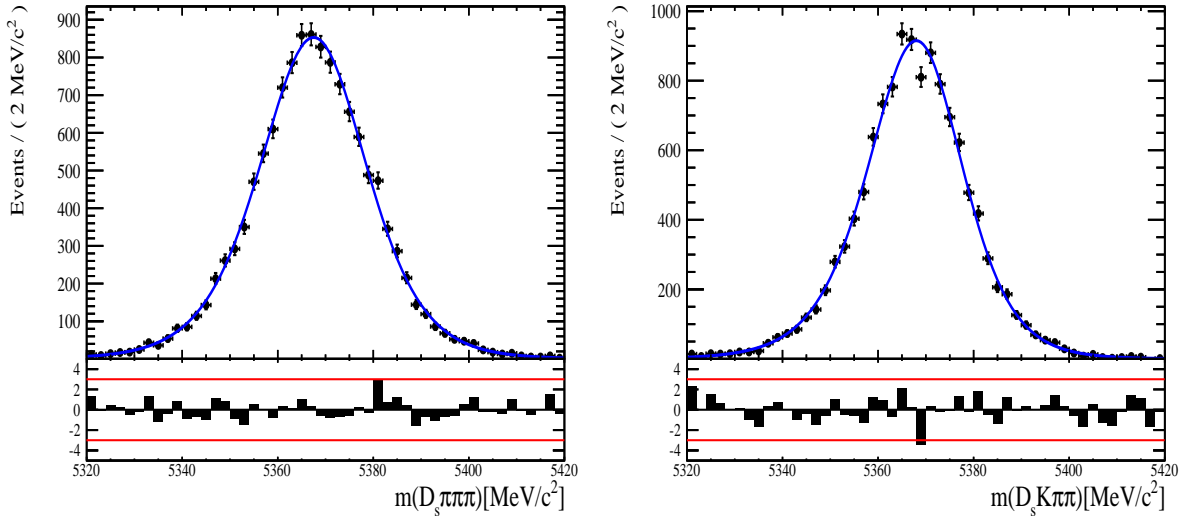


Figure 4.1: Invariant mass distributions of simulated (left) $B_s^0 \rightarrow D_s \pi\pi\pi$ and (right) $B_s^0 \rightarrow D_s K\pi\pi$ events. A fit of a RooJohnsonSU function to each distribution is overlaid.

289 The mass distribution of $B_s^0 \rightarrow D_s K\pi\pi$ signals is modeled using a Johnson SU
 290 function [32], which is a gaussian function with a Landau-like tail on one side,

$$J(m_{B_s^0}; \mu, \sigma, \gamma, \delta) = \frac{\delta}{\sigma 2\pi \sqrt{1 + (\frac{m_{B_s^0} - \mu}{\sigma})^2}} \exp\left(-\frac{1}{2}[\gamma + \delta \operatorname{Argsh}(\frac{m_{B_s^0} - \mu}{\sigma})]^2\right). \quad (4.1)$$

291 The sign of γ in Eq. 4.1 determines whether the tail is located at lower ($\gamma > 0$)
 292 or higher ($\gamma < 0$) invariant mass values than the mean μ of the gaussian function and
 293 δ describes the (a)symmetry of the fitted distribution. Higher values of δ result in a
 294 more symmetric, gaussian-like function. Another Johnson SU function function is used
 295 to account for the contribution of the $B^0 \rightarrow D_s K\pi\pi$ decay, which is also present in
 296 the $m(D_s K\pi\pi)$ spectrum. The width, as well as the tail parameters are fixed to values
 297 obtained by a fit to the invariant mass distribution of simulated events shown in Fig 4.1.
 298 A linear scaling factor for the mean μ and width σ is floated in the fit to account for
 299 possible differences between the simulation and real data.

300 The same approach is used to describe the invariant mass distribution of $B_s^0 \rightarrow D_s \pi\pi\pi$

301 candidates. A Johnson SU function is used to model the signal, the parameters are
302 determined by a fit to the invariant mass of simulated $B_s^0 \rightarrow D_s\pi\pi\pi$ decays, shown in
303 Fig 4.1. A scale factor for the width and the mean is floated to account for differences
304 between data and MC.

305 4.2 Background models for $m(D_s\pi\pi\pi)$

306 Different background sources arise in the invariant mass spectrum of candidates in the
307 normalization mode.

308 The following backgrounds have to be accounted for:

- 309 • Combinatorial background: This contribution arises from either a real D_s , which is
310 paired with random tracks to form the B_s^0 candidates, or via real X_d 's, which are
311 combined with three tracks that fake a D_s candidate to form a fake B_s^0 .
- 312 • Partially reconstructed $B^0/B_s^0 \rightarrow D_s^*\pi\pi\pi$ decays, with $D_s^* \rightarrow D_s\gamma$ or $D_s^* \rightarrow D_s\pi^0$,
313 where the γ/π^0 is not reconstructed in the decay chain.

314 In both cases of combinatorial background, the distribution in the invariant mass of
315 B_s^0 candidates is expected to be smooth and decrease with higher masses. Therefore, one
316 exponential function is used to model these contributions.

317 The shape of the $B_s^0 \rightarrow D_s^*\pi\pi\pi$ contribution is expected to be peaking in the $m(D_s\pi\pi\pi)$
318 spectrum, with large tails due to the missing momentum, which is carried away by the π^0
319 or γ . The pion or photon from $D_s^* \rightarrow D_s(\gamma/\pi^0)$ is excluded from the reconstruction. We
320 model the shape of this contribution using the sum of three bifurcated Gaussian functions.
321 The shape parameters, as well as the yield of this contribution, are directly determined
322 on data from a fit to the $m(D_s\pi\pi\pi)$ invariant mass distribution.

323 4.3 Background models for $m(D_sK\pi\pi)$

324 For the signal channel, the following background sources have to be considered:

- 325 • Combinatorial background: same contributions as discussed in Sec. 4.2.
- 326 • Partially reconstructed $B_s^0 \rightarrow D_s^*K\pi\pi$ decays, with $D_s^* \rightarrow D_s\gamma$ or $D_s^* \rightarrow D_s\pi^0$,
327 where the γ/π^0 is not reconstructed in the decay chain.
- 328 • Partially reconstructed $B^0 \rightarrow D_s^*K\pi\pi$ decays, with $D_s^* \rightarrow D_s\gamma$ or $D_s^* \rightarrow D_s\pi^0$,
329 where the γ/π^0 is not reconstructed in the decay chain.
- 330 • Misidentified $B_s^0 \rightarrow D_s\pi\pi\pi$ decays, where one of the pions is wrongly identified as a
331 kaon $\pi \rightarrow K$.
- 332 • Misidentified, partially reconstructed $B_s^0 \rightarrow D_s^*\pi\pi\pi$ decays, where one of the pions
333 is wrongly identified as a kaon $\pi \rightarrow K$ and the γ/π^0 from $D_s^* \rightarrow D_s\gamma/\pi^0$ is not
334 reconstructed.

335 The combinatorial background is expected to be non-peaking in the spectrum of the
336 invariant mass of $B_s^0 \rightarrow D_sK\pi\pi$ candidates. An exponential function is used to model
337 this contribution.

338 The shape of the partially reconstructed background without misID is taken from our
 339 normalization channel, where it can be directly fitted by the sum of three bifurcated
 340 Gaussian functions as described above. In the signal mass fit, all shape parameters for
 341 the $B_s^0 \rightarrow D_s^* K\pi\pi$ background are fixed to the input values from our normalization fit.

342 For the contribution of the $B^0 \rightarrow D_s^* K\pi\pi$ background, the same shape is used but
 343 the means μ_i of the bifurcated gaussians are shifted down by $m_{B_s^0} - m_{B^0}$ [?]. The yields
 344 of both contributions are directly determined in the nominal fit.

345 To determine the shape of misidentified $B_s^0 \rightarrow D_s\pi\pi\pi$ candidates in the $m(D_s K\pi\pi)$
 346 spectrum, we take a truth-matched signal MC sample of our normalization channel. We
 347 then use the PIDCalib package to determine the $\pi \rightarrow K$ fake rate. For every candidate
 348 in our MC sample, a (momentum) p and (pseudorapidity) η -dependent event weight is
 349 computed and assigned. We flip the particle hypothesis from pion to kaon for the π with
 350 the biggest miss-ID weight for each event and recompute the invariant B_s^0 mass. This
 351 distribution is then modeled using two Crystal Ball functions. The distribution and the
 352 fit are shown in Fig. 4.2(left).

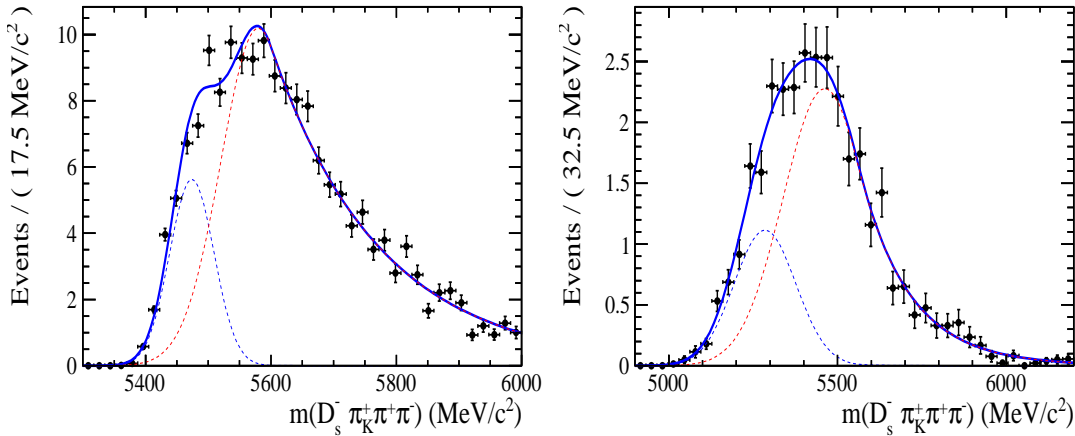


Figure 4.2: Invariant mass distribution of (left) simulated $B_s^0 \rightarrow D_s\pi\pi\pi$ events, where one of the π 's is reconstructed as a K and the misID probability for each event is taken into account. The corresponding distribution for simulated $B_s^0 \rightarrow D_s^*\pi\pi\pi$ events, where the γ/π^0 from the D_s^* is excluded from reconstruction, is shown on the right. The solid, black curve on each plot corresponds to the fit consisting of two Crystal Ball functions.

353 The expected yield of misidentified $B_s^0 \rightarrow D_s\pi\pi\pi$ candidates in the $m(D_s K\pi\pi)$ spec-
 354 trum is computed by multiplying the fake probability of $\propto 3.2\%$, which is derived from
 355 PIDCalib, by the yield of $B_s^0 \rightarrow D_s\pi\pi\pi$ signal candidates, determined in the nominal
 356 mass fit of our normalization channel.

357 In the same way as mentioned above, we can determine the rate of misidentified, partially
 358 reconstructed $B_s^0 \rightarrow D_s^*\pi\pi\pi$ decays in our sample of $B_s^0 \rightarrow D_s K\pi\pi$ decays using PIDCalib
 359 and a MC sample of $B_s^0 \rightarrow D_s^*\pi\pi\pi$ events. The invariant mass distribution we obtain
 360 when we exclude the γ/π^0 , flip the the particle hypothesis $\pi \rightarrow K$ and apply the event
 361 weights given by the fake rate, is shown in Fig. 4.2 (right). The fit of two Crystal Ball
 362 functions to this distribution is overlaid. The yield of this contribution is determined
 363 from the yield of $B_s^0 \rightarrow D_s^*\pi\pi\pi$ candidates in the nominal mass fit of our normalization
 364 channel, multiplied by the misID probability of $\propto 3.6\%$.

365 4.4 Fit to $B_s^0 \rightarrow D_s\pi\pi\pi$ candidates

366 An unbinned maximum likelihood fit is performed simultaneously to the invariant mass
 367 distribution of $B_s^0 \rightarrow D_s\pi\pi\pi$ candidates. As discussed in Sec. ??, the fit is given
 368 as a Johnson SU signal model for the B_s^0 and B^0 signal, the sum of three bifurcated
 369 Gaussian functions to model the partially reconstructed $B_s^0 \rightarrow D_s^*\pi\pi\pi$ background and
 370 an Exponential function to account for combinatorial background. The invariant mass
 371 distribution and the fit is shown in Fig. 4.3. All simultaneously performed fits to the
 372 $m(D_s\pi\pi\pi)$ distribution, ordered by the respective D_s final state, can be found in the
 373 Appendix ???. The obtained yields are summarized in Table 4.1.

374 4.5 Fit to $B_s^0 \rightarrow D_sK\pi\pi$ candidates

375 The shape of the invariant mass distribution of $B_s^0 \rightarrow D_sK\pi\pi$ candidates is described by
 376 Johnson SU functions for the B^0 and B_s^0 signal, two sums of three bifurcated Gaussians
 377 for the $B_s^0/B^0 \rightarrow D_s^*K\pi\pi$ partially reconstructed background contributions and two
 378 sums of double Crystal Ball functions for the single misID $B_s^0 \rightarrow D_s\pi\pi\pi$ and the partially
 379 reconstructed, misidentified $B_s^0 \rightarrow D_s^*\pi\pi\pi$ decays. A simultaneous unbinned maximum
 380 likelihood fit is performed and the result is shown in Fig. 4.3. All simultaneously performed
 381 fits to the $m(D_sK\pi\pi)$ distribution, ordered by the respective D_s final state, can be found
 382 in the Appendix ???. The obtained yields are summarized in Table 4.1.

383 4.6 Extraction of signal weights

384 The sPlot technique [31] is used to extract signal weights from the fits to the invariant
 385 mass distributions of our signal and normalization channel. This statistical tool assigns
 386 a weight to every event, according to its position in the respective mass distribution,
 387 given the fitted signal and background models. The weights can then be used to suppress
 388 the background components in every other observable distribution of interest. Figure ??
 389 shows the distribution of weights across the invariant mass spectra of $B_s^0 \rightarrow D_s\pi\pi\pi$ and
 390 $B_s^0 \rightarrow D_sK\pi\pi$ candidates.

| fit component | yield 2011 | yield 2012 | yield 2015 | yield 2016 |
|--|----------------|-----------------|----------------|-----------------|
| $m(D_sK\pi\pi)$ | | | | |
| $B_s^0 \rightarrow D_sK\pi\pi$ | 392 ± 25 | 860 ± 38 | 309 ± 21 | 1984 ± 55 |
| $B^0 \rightarrow D_sK\pi\pi$ | 276 ± 26 | 692 ± 41 | 261 ± 23 | 1385 ± 58 |
| $B^0/B_s^0 \rightarrow D_s^*K\pi\pi$ | 7 ± 25 | 171 ± 75 | 114 ± 25 | 893 ± 84 |
| $B_s^0 \rightarrow D_s^{(*)}\pi\pi\pi$ | 63 ± 0 | 158 ± 0 | 53 ± 0 | 314 ± 0 |
| combinatorial | 1482 ± 53 | 2884 ± 100 | 605 ± 43 | 4261 ± 133 |
| $m(D_s\pi\pi\pi)$ | | | | |
| $B_s^0 \rightarrow D_s\pi\pi\pi$ | 9183 ± 105 | 22083 ± 166 | 7574 ± 95 | 43773 ± 245 |
| $B^0 \rightarrow D_s\pi\pi\pi$ | 289 ± 58 | 716 ± 95 | 229 ± 54 | 968 ± 147 |
| $B_s^0 \rightarrow D_s^*\pi\pi\pi$ | 3640 ± 130 | 9086 ± 232 | 3047 ± 110 | 17827 ± 421 |
| combinatorial | 4991 ± 154 | 11127 ± 271 | 3728 ± 126 | 24589 ± 500 |

Table 4.1: Summary of yields obtained from the fits to Run1 and Run2 data.

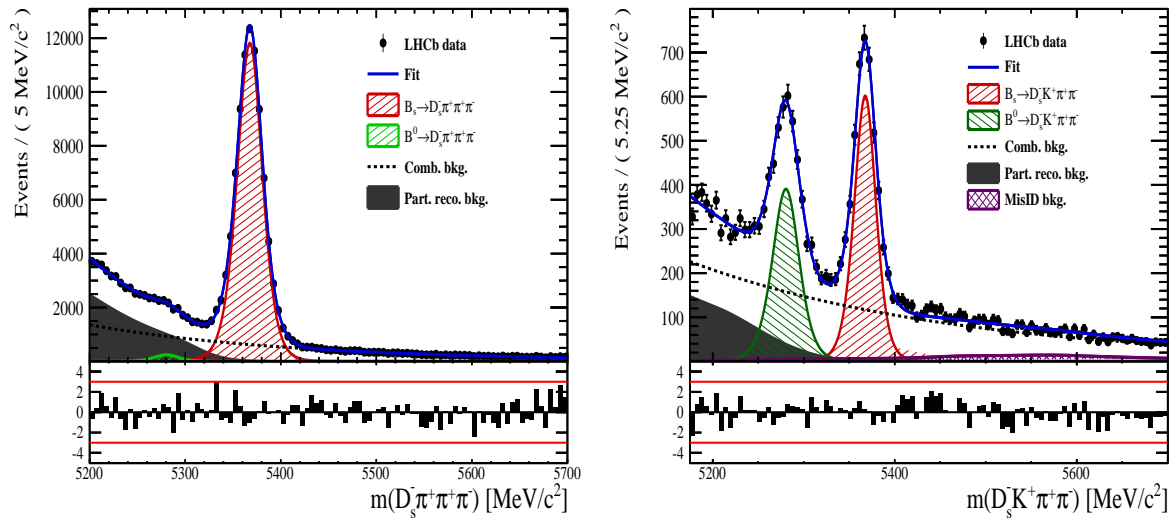


Figure 4.3: Invariant mass distribution of (left) $B_s^0 \rightarrow D_s \pi \pi \pi$ and (right) $B_s^0 \rightarrow D_s K \pi \pi$ candidates for Run1 and Run2 data. The respective fit described in the text is overlaid.

391 5 Flavour Tagging

392 To successfully perform a time- and amplitude-dependent measurement of γ , the identifi-
 393 cation of the initial state flavour of the B_s^0 meson is crucial. In the presented analysis,
 394 a number of flavour tagging algorithms are used that either determine the flavour of
 395 the non-signal b-hadron produced in the event (opposite site, OS), or they use particles
 396 produced in the fragmentation of the signal candidate B_s^0/\bar{B}_s^0 (same side, SS).
 397 For the same side, the algorithm searching for the charge of an additional kaon that accom-
 398 panies the fragmentation of the signal candidate is used (SS-nnetKaon). For the opposite
 399 site, four different taggers are chosen: The Two algorithms that use the charge of an
 400 electron or a muon from semileptonic B decays (OS- e,μ), the tagger that uses the charge
 401 of a kaon from a $b \rightarrow c \rightarrow s$ decay chain (OS-nnetKaon) and the algorithm that determines
 402 the B_s^0/\bar{B}_s^0 candidate flavour from the charge of a secondary vertex, reconstructed from
 403 the OS b decay product (OS-VtxCharge). All four taggers are then combined into a signal
 404 OS tagger.
 405 Every single tagging algorithm is prone to misidentify the signal candidate at a certain
 406 mistag rate $\omega = (\text{wrongtags})/(\text{alltags})$. This might be caused by particle misidentifica-
 407 tion, flavour oscillation of the neutral opposite site B-meson or by tracks that are wrongly
 408 picked up from the underlying event. For every signal B_s^0/\bar{B}_s^0 candidate, each tagging
 409 algorithm predicts a mistag probability η , which is calculated using a combination of
 410 inputs such as the kinematics of the tagging particles. The inputs are then combined
 411 to a predicted mistag using neural networks. These are trained on simulated samples
 412 of $B_s^0 \rightarrow D_s^- \pi^+$ (SS algorithm) and $B^+ \rightarrow J/\psi K^+$ (OS algorithms) decays. For the
 413 presented analysis, the measurable CP-violating coefficients are damped by the tagging
 414 dilution D , that depends on the mistag rate:

$$D = 1 - 2\omega. \quad (5.1)$$

415 This means that the statistical precision, with which these coefficients can be measured,
 416 scales as the inverse square root of the effective tagging efficiency,

$$\epsilon_{eff} = \epsilon_{tag}(1 - 2\omega)^2, \quad (5.2)$$

417 where ϵ_{tag} is the fraction of events that have a tagging decision. The flavour
 418 tagging algorithms are optimised for highest ϵ_{eff} on data, using the $B_s^0 \rightarrow D_s^- \pi^+$ and
 419 $B^+ \rightarrow J/\psi K^+$ samples.

420 Utilizing flavour-specific final states, the predicted mistag η of each tagger has to be
 421 calibrated to match the observed mistag ω on the data sample. For the calibration, a
 422 linear model of the form

$$\omega(\eta) = p_0 + p_1 \cdot (\eta - \langle \eta \rangle), \quad (5.3)$$

423 where the values of p_0 and p_1 are determined using the $B_s^0 \rightarrow D_s \pi \pi \pi$ normalization
 424 mode and $\langle \eta \rangle$ is the average estimated mistag probability $\langle \eta \rangle = \sum_{i=1}^{N_{cand}} (\eta_i)/N_{cand}$.
 425 Following this model, a perfectly calibrated tagger would lead to $\omega(\eta) = \eta$ and one would
 426 expect $p_1 = 1$ and $p_0 = \langle \eta \rangle$. Due to the different interaction cross-sections of oppositely
 427 charged particles, the tagging calibration parameters depend on the initial state flavour of
 428 the B_s^0 . Therefore, the flavour asymmetry parameters Δp_0 , Δp_1 and $\Delta \epsilon_{tag}$ are introduced.
 429 For this analysis, the calibrated mistag is treated as per-event variable, giving a larger

weight to events that are less likely to have an incorrect tag. This adds one additional observable to the time- and amplitude-dependent fit.
 The tagging calibration is determined using a time-dependent fit to the full $B_s^0 \rightarrow D_s\pi\pi\pi$ sample, where the mixing frequency Δm_s is fixed to the nominal PDG value [33]. The calibration procedure for the OS tagging algorithms (Sec.5.1) and the SS kaon tagger (Sec.5.2) is applied on the full Run I and 2015 and 2016 Run II $B_s^0 \rightarrow D_s\pi\pi\pi$ data sample, which is selected following the steps described in Sec. 3. The similar selection ensures as close as possible agreement between the $B_s^0 \rightarrow D_s\pi\pi\pi$ and $B_s^0 \rightarrow D_sK\pi\pi$ samples in terms of the decay kinematics, which are crucial for the flavour tagging. Section 5.3 shows the compatibility of both samples. After applying the calibration, the response of the OS and SS taggers are combined, which is shown in Sec. 5.4.

5.1 OS tagging calibration

The responses of the OS electron, muon, neural net kaon and the secondary vertex charge taggers are combined for the mistag calibration. Figure ?? shows the distribution of the predicted OS mistag for signal candidates from $B_s^0 \rightarrow D_s\pi\pi\pi$. The extracted calibration parameters and tagging asymmetries are summarized in Table 5.1 and the measured tagging power for the OS combination is $\epsilon_{eff,OS} = 4.81\%$.

| p_0 | p_1 | $<\eta>$ | ϵ_{tag} | Δp_o | Δp_1 | $\epsilon_{eff} [\%]$ |
|-------------------|-------------------|----------|-------------------|-------------------|-------------------|---|
| 0.025 ± 0.005 | 0.944 ± 0.048 | 0.347 | 0.517 ± 0.002 | 0.028 ± 0.005 | 0.037 ± 0.045 | $4.81 \pm 0.04 (\text{stat}) \pm 0.37 (\text{cal})$ |

Table 5.1: Calibration parameters and tagging asymmetries of the OS tagger extracted from $B_s^0 \rightarrow D_s\pi\pi\pi$ decays.

5.2 SS tagging calibration

The SS neural net kaon tagger can be calibrated using the flavour-specific $B_s^0 \rightarrow D_s\pi\pi\pi$ decay. It's development, performance and calibration is described in detail in [34]. Figure ?? shows the distribution of the predicted mistag of the neural net kaon tagger. The extracted calibration parameters and tagging asymmetries are summarized in Table 5.2 and the measured tagging power for this algorithm is $\epsilon_{eff,SS} = 3.22\%$.

| p_0 | p_1 | $<\eta>$ | ϵ_{tag} | Δp_o | Δp_1 | $\epsilon_{eff} [\%]$ |
|-------------------|-------------------|----------|-------------------|--------------------|-------------------|---|
| 0.008 ± 0.004 | 1.086 ± 0.059 | 0.381 | 0.571 ± 0.002 | -0.017 ± 0.004 | 0.135 ± 0.058 | $3.22 \pm 0.03 (\text{stat}) \pm 0.26 (\text{cal})$ |

Table 5.2: Calibration parameters and tagging asymmetries of the SS tagger extracted from $B_s^0 \rightarrow D_s\pi\pi\pi$ decays.

5.3 Tagging performance comparison between the signal and normalization channel

To justify the usage of the tagging calibration, obtained using the $B_s^0 \rightarrow D_s\pi\pi\pi$ sample, for our signal decay, the performance of the taggers in the two decay channels needs to be compatible. This is verified using both, simulated signal samples of both decays and

458 sweighted data, to compare the similarity of the mistag probabilities, tagging decisions
 459 and kinematic observables that are correlated with the tagging response, on simulation
 460 and data.

461 The distributions of the predicted mistag probability η for the OS combination and the
 462 SS kaon tagger are shown in Fig. ?? (simulation) and Fig. 5.1 (data).

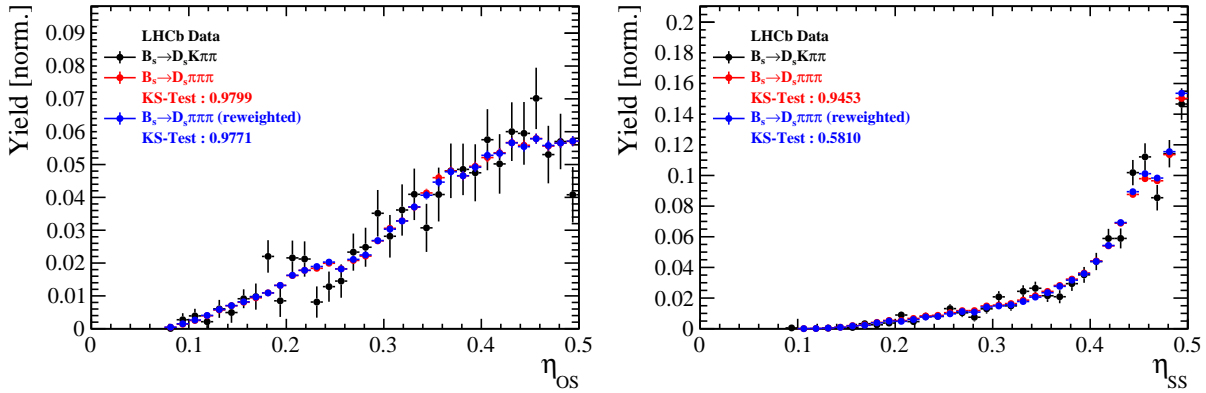


Figure 5.1: Distributions of the predicted mistag η for the OS combination (left) and the SS kaon tagger (right) for signal candidates in the $B_s^0 \rightarrow D_s K\pi\pi$ (black) and $B_s^0 \rightarrow D_s \pi\pi\pi$ (red) data samples.

463 Both, data and simulated samples, show good agreement between the signal and
 464 normalization channel. Compatibility is also seen in Fig. ??, which shows the comparison
 465 of the tagging decision distributions of the OS and SS tagger for sweighted data.

466 Fig. ?? shows the signal data distributions of the transverse B_s^0 momentum p_T , the
 467 pseudorapidity η of the signal candidate and the number of reconstructed tracks per event.
 468 Sufficient agreement is observed.

469 To justify the portability of the flavour tagging calibration obtained from $B_s^0 \rightarrow D_s \pi\pi\pi$
 470 to the $B_s^0 \rightarrow D_s K\pi\pi$ channel, besides the good agreement of the distributions shown
 471 above, the dependence of the measured mistag ω on the predicted mistag η has to be
 472 compatible in both channel. This dependence is shown in Fig. 5.2 for simulated signal
 473 events of both channels, where good agreement is observed.

474 5.4 Combination of OS and SS taggers

475 In the time- and amplitude-dependent fit to $B_s^0 \rightarrow D_s K\pi\pi$ data, the obtained tagging
 476 responses of the OS and SS tagger will be combined after the calibration described in the
 477 previous sections is applied. Events that acquire a mistag probability greater than 0.5 after
 478 the calibration will have their tagging decision flipped. For events where only one of the
 479 two taggers fired, the combination of the tagging decision is trivial. In those events where
 480 both taggers made a decision, we use the standard combination of taggers [35] provided
 481 by the flavour tagging group. In the nominal fit, the calibrated mistags ω are combined
 482 event by event for the OS and SS tagger, thus adding one variable to observable to the
 483 fit procedure. This ensures that the uncertainties of the OS and SS tagging calibration
 484 parameters are propagated properly to the combined tagging response for each event.
 485 The tagging performance for the combined tagger in the categories SS tagged only, OS
 486 tagged only and SS+OS tagged, are shown in Tab. ?? for the signal and normalization

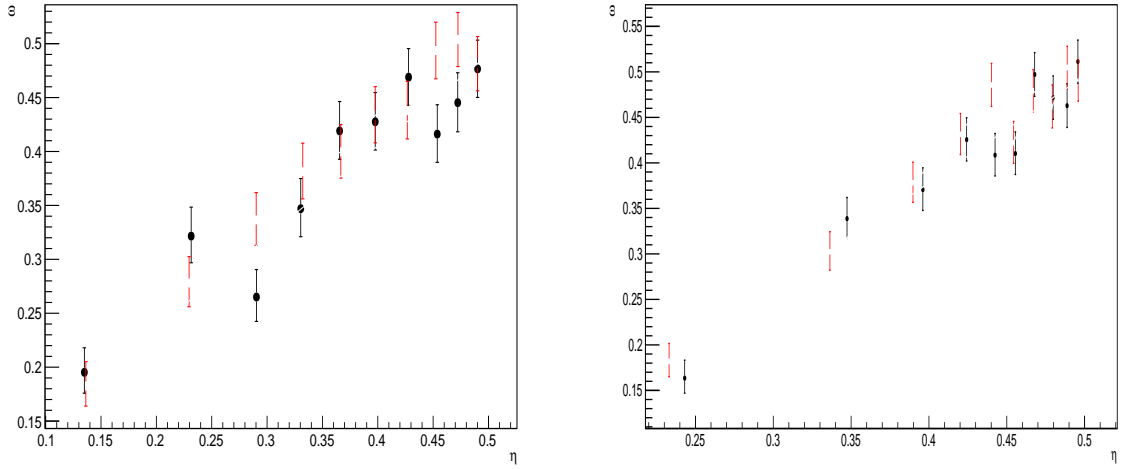


Figure 5.2: Dependence of the observed mistag ω on the predicted mistag η for the (left) OS combination and the (right) SS kaon tagger, found in the simulated $B_s^0 \rightarrow D_s K\pi\pi$ (black) and $B_s^0 \rightarrow D_s \pi\pi\pi$ (red) signal samples.

487 channel. The distribution of the observed mistag ω as a function of the combined mistag
 488 probability η for $B_s^0 \rightarrow D_s \pi\pi\pi$ decays is shown in Fig. 5.3.

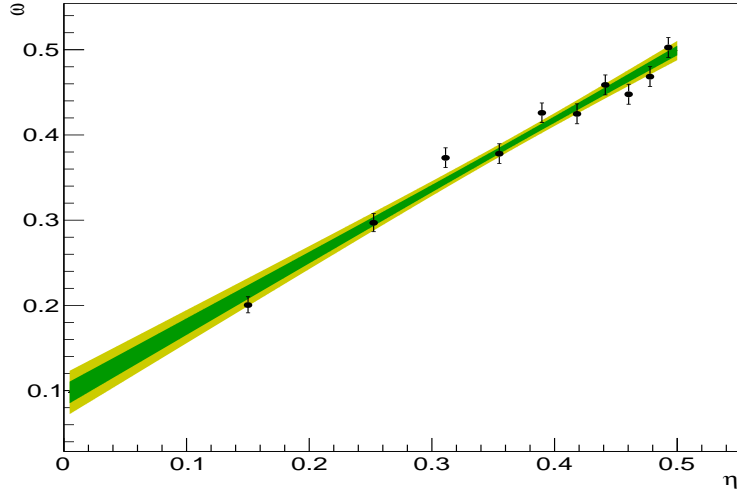


Figure 5.3: Distribution of the predicted combined mistag probability η versus the observed mistag ω for $B_s^0 \rightarrow D_s \pi\pi\pi$ signal candidates. The fit with a linear polynomial, used to determine p_0 and p_1 is overlaid.

Table 5.3: The flavour tagging performances for only OS tagged, only SS tagged and both OS and SS tagged events for Run-I data.

| $B_s \rightarrow D_s \pi\pi\pi$ | $\epsilon_{tag} [\%]$ | $\langle \omega \rangle [\%]$ | $\epsilon_{eff} [\%]$ |
|---------------------------------|-----------------------|-------------------------------|-----------------------|
| Only OS | 10.51 ± 0.08 | 37.59 ± 1.03 | 0.96 ± 0.14 |
| Only SS | 43.27 ± 0.18 | 42.22 ± 0.65 | 2.17 ± 0.32 |
| Both OS-SS | 24.77 ± 0.22 | 36.12 ± 0.78 | 2.90 ± 0.27 |
| Combined | 78.55 ± 0.30 | 39.68 ± 0.75 | 6.03 ± 0.44 |

Table 5.4: The flavour tagging performances for only OS tagged, only SS tagged and both OS and SS tagged events for Run-II data.

| $B_s \rightarrow D_s \pi\pi\pi$ | $\epsilon_{tag} [\%]$ | $\langle \omega \rangle [\%]$ | $\epsilon_{eff} [\%]$ |
|---------------------------------|-----------------------|-------------------------------|-----------------------|
| Only OS | 11.32 ± 0.07 | 35.65 ± 0.77 | 1.28 ± 0.12 |
| Only SS | 41.66 ± 0.14 | 44.64 ± 0.37 | 1.13 ± 0.12 |
| Both OS-SS | 27.17 ± 0.20 | 35.43 ± 0.64 | 3.32 ± 0.24 |
| Combined | 80.15 ± 0.25 | 40.25 ± 0.54 | 5.73 ± 0.29 |

489 6 Acceptance

490 6.1 MC corrections

491 6.1.1 Truth matching of simulated candidates

492 We use the `BackgroundCategory` tool to truth match our simulated candidates. Candidates
 493 with background category (`BKGCAT`) 20 or 50 are considered to be true signal. Background
 494 category 60 is more peculiar since it contains both badly reconstructed signal candidates
 495 and ghost background. This is due to the fact that the classification algorithms identifies
 496 all tracks for which less than 70% of the reconstructed hits are matched to generated
 497 truth-level quantities as ghosts. In particular for signal decays involving many tracks (as
 498 in our case), this arbitrary cutoff is not 100% efficient. Moreover, the efficiency is expected
 499 to depend on the kinematics which would lead to a biased acceptance determination if
 500 candidates with `BKGCAT`= 60 would be removed.

501 We therefore include `BKGCAT`= 60 and statistically subtract the ghost background by
 502 using the `sPlot` technique. The `sWeights` are calculated from a fit to the reconstructed B_s
 503 mass. The signal contribution is modeled as described in Sec. 4.1 and the background
 504 with a polynomial. The fit is performed simultaneously in two categories; the first includes
 505 events with `BKGCAT` = 20 or 50 and the second events with `BKGCAT` = 60. To account
 506 for the different mass resolution we use a different σ for each category, while the mean
 507 and the tail parameters are shared between them. The background component is only
 508 included for the second category.

509 A significant fraction of 8% of the true signal candidates are classified as ghosts, while
 510 only 20% of the events classified with `BKGCAT`= 60 are indeed genuine ghosts.

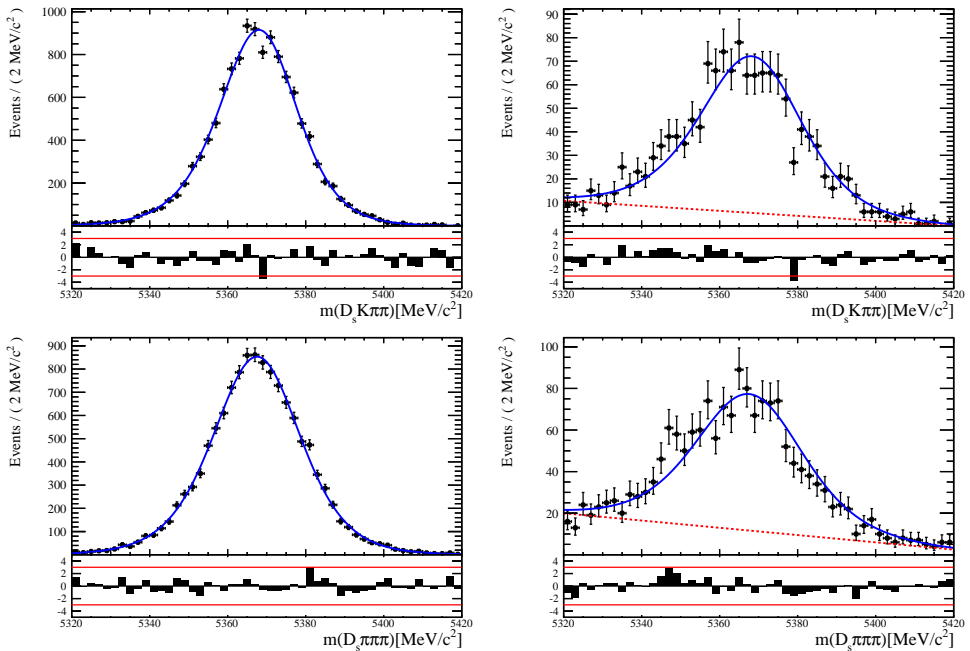


Figure 6.1: The reconstructed B_s mass distribution for simulated $B_s \rightarrow D_s K\pi\pi$ (top) and $B_s \rightarrow D_s \pi\pi\pi$ (bottom) decays classified with `BKGCAT` = 20 or 50 (left) and `BKGCAT` = 60 (right) after the full selection.

511 6.1.2 PID efficiencies

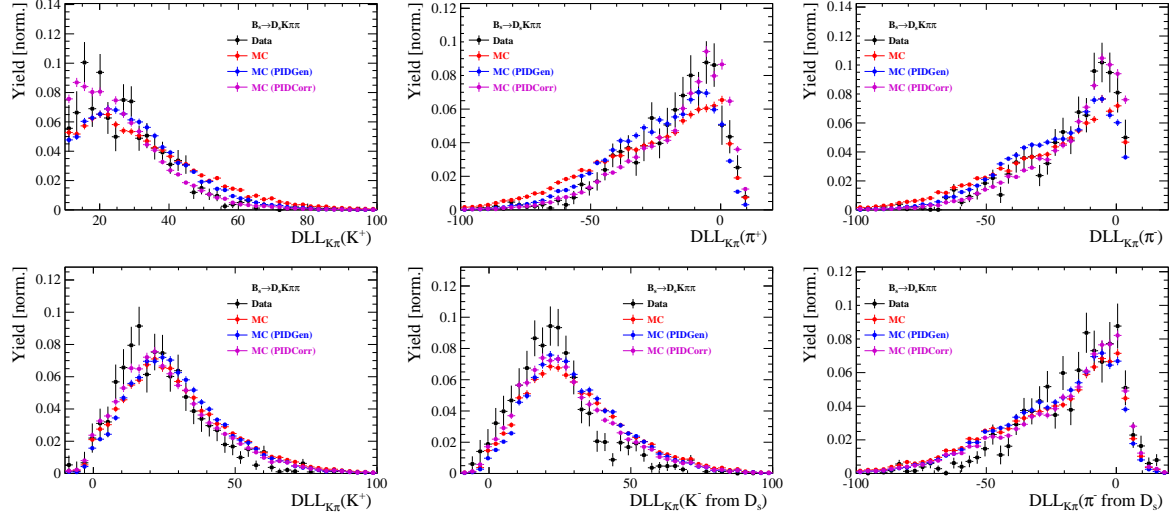


Figure 6.2

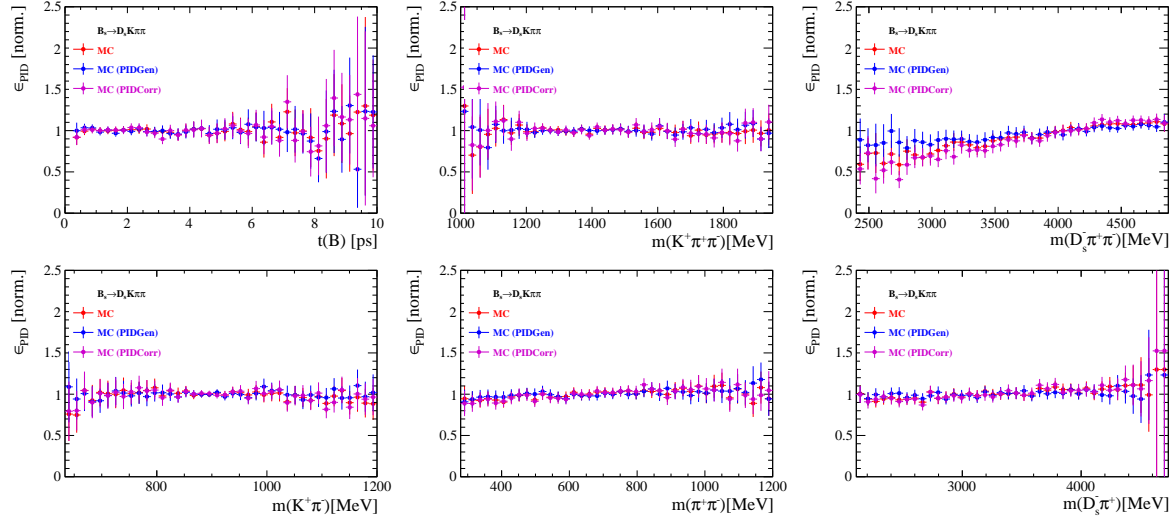


Figure 6.3

512 6.1.3 BDT efficiencies

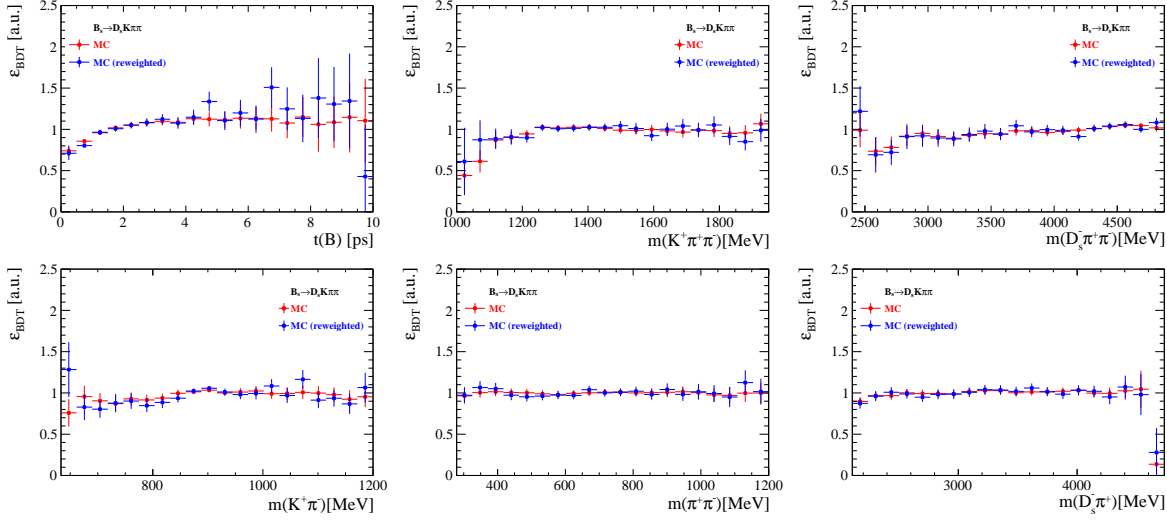


Figure 6.4

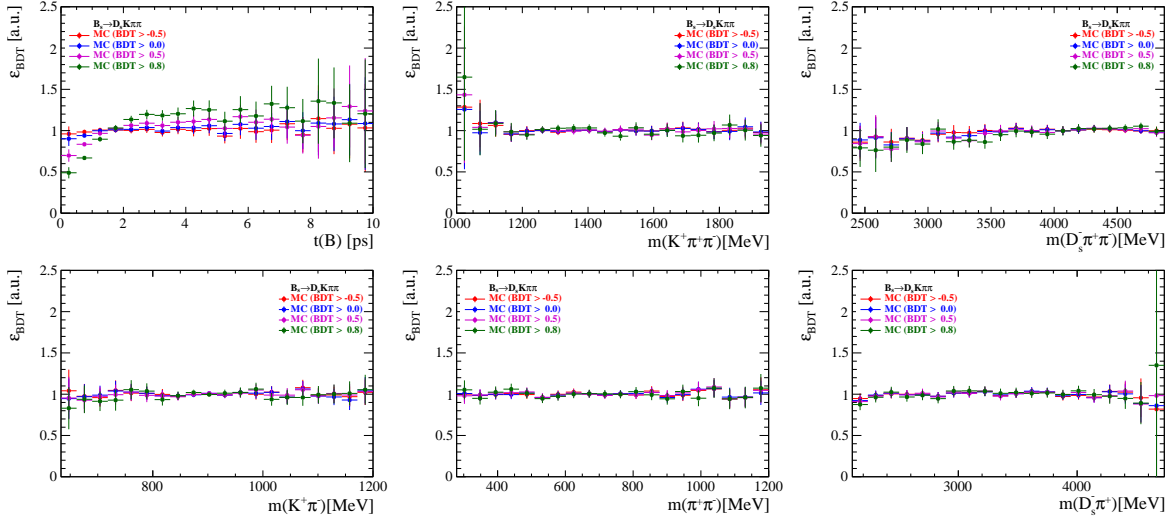


Figure 6.5

⁵¹³ 6.1.4 Tracking efficiencies

514 **6.2 Decay-time acceptance**

515 The decay-time distribution of the B_s^0 mesons is sculpted due to the geometry of the LHCb
 516 detector and the applied selection cuts, which are described in Section 3. In particular,
 517 any requirement on the flight distance (FD), the impact parameter (IP) or the direction
 518 angle (DIRA) of the B_s^0 mesons, as well as the direct cut on the lifetime, will lead to a
 519 decay-time dependent efficiency $a(t)$. This efficiency will distort the theoretically expected,
 520 time-dependent decay rate

$$\frac{\Gamma(t)^{observed}}{dt} = \frac{\Gamma(t)^{theory}}{dt} \cdot a(t), \quad (6.1)$$

521 and has to be modelled correctly, in order to describe the observed decay rate. We
 522 use our control channel for this measurement, because for $B_s^0 \rightarrow D_s K\pi\pi$ decays the
 523 decay-time acceptance is correlated with the CP-observables which we aim to measure.
 524 Therefore, floating the CP-observables and the acceptance shape at the same time is
 525 not possible. Hence, a fit to the decay-time distribution of $B_s^0 \rightarrow D_s \pi\pi\pi$ candidates is
 526 performed and the obtained acceptance shape is corrected by the difference in shape found
 527 for the $B_s^0 \rightarrow D_s K\pi\pi$ and $B_s^0 \rightarrow D_s \pi\pi\pi$ MC.

528 A PDF of the form

$$\mathcal{P}(t', \vec{\lambda}) = \left[(e^{\Gamma_s t} \cdot \cosh(\frac{\Delta\Gamma_s t}{2}) \times \mathcal{R}(t - t')) \right] \cdot \epsilon(t', \vec{\lambda}), \quad (6.2)$$

529 is fit to the decay time distribution of $B_s^0 \rightarrow D_s \pi\pi\pi$ candidates in data. Since the
 530 fit is performed untagged, the PDF shown in Eq. 6.2 contains no terms proportional
 531 to Δm_s . The values for Γ_s and $\Delta\Gamma_s$ are fixed to the latest HFAG results [36]. The
 532 decay-time acceptance $\epsilon(t', \vec{\lambda})$ is modelled using the sum of cubic polynomials $v_i(t)$, so
 533 called Splines [37]. The polynomials are parametrised by so-called knots which determine
 534 their boundaries. Knots can be set across the fitted distribution to account for local
 535 changes in the acceptance shape. Using more knots is equivalent to using more base
 536 splines which are defined on a smaller sub-range. In total, $n + 2$ base splines $v_i(t)$ are
 537 needed to describe an acceptance shape which is parametrised using n knots.

538 For fits shown in the following, the knots have been placed at $t = [0.5, 1.0, 1.5, 2.0, 3.0, 9.5] ps$. To accommodate these 6 knot positions, 8 basic splines
 539 v_i , $i = [1, \dots, 8]$ are used. Since a rapid change of the decay time acceptance at low
 540 decay times due to the turn-on effect generated by the lifetime and other selection cuts is
 541 expected, more knots are placed in that regime. At higher decay times we expect linear
 542 behavior, with a possible small effect due to the VELO reconstruction. Therefore fewer
 543 knots are used. Furthermore, v_7 is fixed to 1 in order to normalize the overall acceptance
 544 function. To stabilise the last spline, v_8 is fixed by a linear extrapolation from the two
 545 previous splines:

$$v_N = v_{N-1} + \frac{v_{N-2} - v_{N-1}}{t_{N-2} - t_{N-1}} \cdot (t_N - t_{N-1}). \quad (6.3)$$

547 Here, $N = 8$ and t_{N-1} corresponds to the knot position associated with v_{N-1} .

548 6.2.1 Comparison of acceptance in subsamples

549 It is possible that the decay-time dependent efficiency deviates in different subsamples of
 550 our data. In particular, the acceptance could differentiate in subsamples with different
 551 final state kinematics, such as the run I & run II sample, the various D_s final states and
 552 the ways an event is triggered at the L0 stage. To investigate possible deviations, the
 553 full selected $B_s^0 \rightarrow D_s\pi\pi\pi$ sample is split into subsamples according to the categories
 554 mentioned above (run, D_s state, L0 trigger). For each subsample, the fit procedure
 555 described at the beginning of this chapter, using the pdf given by Eq. 6.2, is repeated
 556 and the obtained values for the spline coefficients v_i are compared. Figure 6.6 shows the
 557 comparison of the obtained spline coefficients for the different D_s final states.

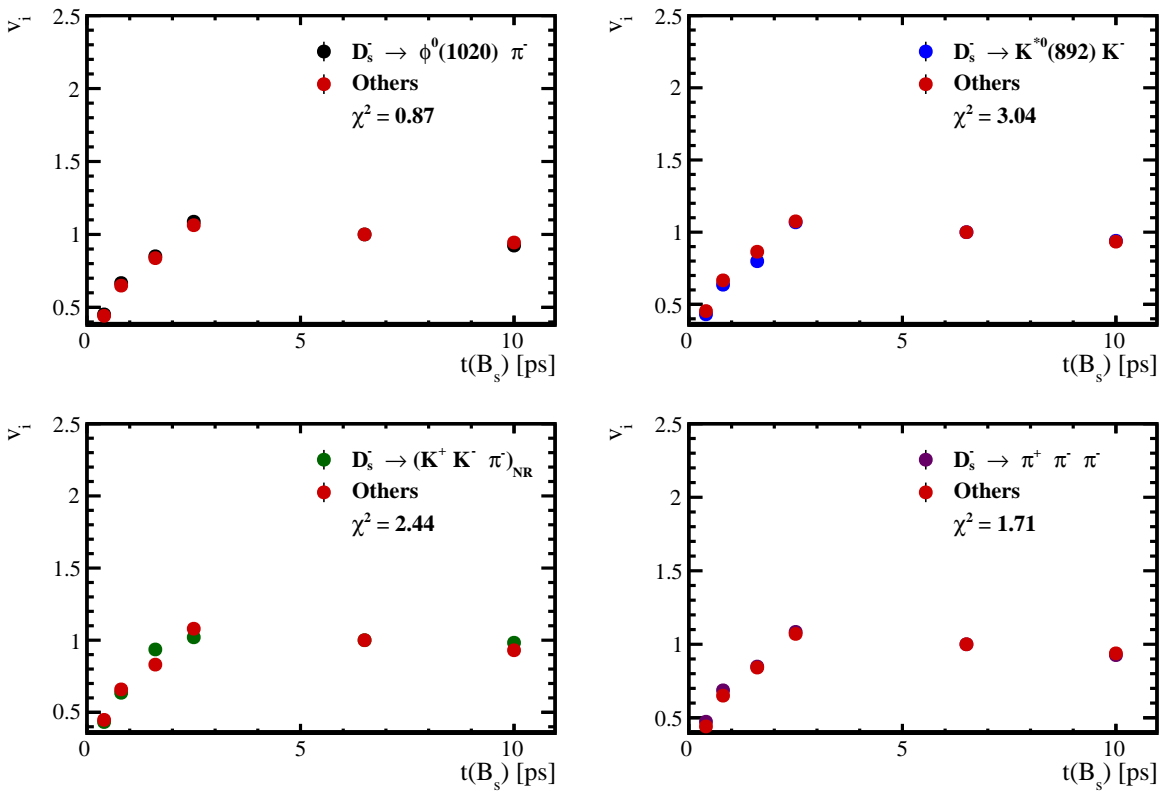


Figure 6.6: Comparison of the spline coefficients obtained from time-dependent fits to the $B_s^0 \rightarrow D_s\pi\pi\pi$ subsamples of different D_s final states. The comparison of one particular D_s state against all other states is shown.

558 Investigating the obtained spline coefficients from different D_s final states, good
 559 agreement is observed between all four channels and no need to distinguish between
 560 different final states in the time-dependent amplitude fit is found.

561 The comparison between spline coefficients for the different runs and L0 trigger categories
 562 is shown in Figure 6.7.

563 Significant deviations between spline coefficients obtained from the two different runs
 564 and L0 trigger categories can be observed. The deviations are most pronounced in the
 565 (0 – 5) ps region, where the majority of statistics is found. Therefore, the time-dependent
 566 efficiency has to be treated separately for the runs and L0 categories. This is achieved by

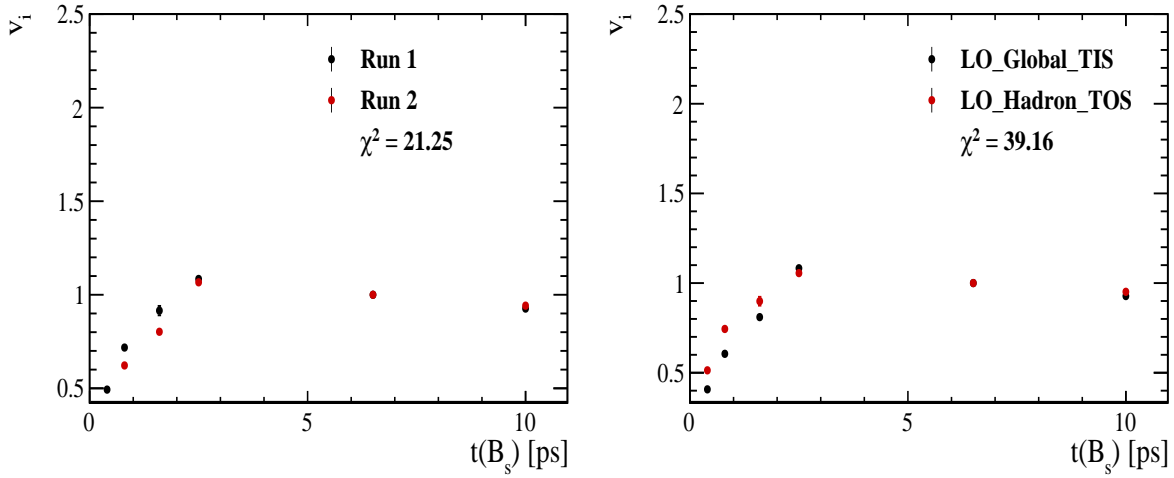


Figure 6.7: Comparison of the spline coefficients obtained from time-dependent fits to the $B_s^0 \rightarrow D_s \pi \pi \pi$ subsamples of (left) the different runs and (right) L0 trigger categories.

567 implementing a simultaneous fit, where the acceptance description is allowed to vary in
 568 the subsamples.

569 **6.2.2 Results**

570 The nominal fit to $B_s^0 \rightarrow D_s\pi\pi\pi$ data using this configuration is shown in Figure ??.
571 Note that the normalization of the splines in the following figures is not in scale. The fit
572 parameters obtained from the described fits to data and simulation are summarised in
573 Table 6.4.

Table 6.1: Time acceptance parameters for events in category [Run-I,L0-TOS].

| Knot position | Coefficient | $B_s^0 \rightarrow D_s K\pi\pi$ data | $B_s^0 \rightarrow D_s K\pi\pi$ MC | Ratio |
|---------------|-------------|--------------------------------------|------------------------------------|----------------------|
| 0.4 | v_0 | 0.561 ± 0.038 | 0.546 ± 0.022 | 0.953 ± 0.060 |
| 0.8 | v_1 | 0.826 ± 0.059 | 0.785 ± 0.034 | 0.910 ± 0.066 |
| 1.6 | v_2 | 0.843 ± 0.087 | 0.905 ± 0.056 | 1.055 ± 0.095 |
| 2.5 | v_3 | 1.154 ± 0.036 | 1.118 ± 0.028 | 0.930 ± 0.045 |
| 6.5 | v_4 | 1.0 (fixed) | 1.0 (fixed) | 1.0 (fixed) |
| 10.0 | v_5 | 0.866 (interpolated) | 0.897 (interpolated) | 1.061 (interpolated) |

Table 6.2: Time acceptance parameters for events in category [Run-I,L0-TIS].

| Knot position | Coefficient | $B_s^0 \rightarrow D_s K\pi\pi$ data | $B_s^0 \rightarrow D_s K\pi\pi$ MC | Ratio |
|---------------|-------------|--------------------------------------|------------------------------------|----------------------|
| 0.4 | v_0 | 0.368 ± 0.031 | 0.412 ± 0.020 | 0.955 ± 0.077 |
| 0.8 | v_1 | 0.583 ± 0.050 | 0.648 ± 0.033 | 0.910 ± 0.074 |
| 1.6 | v_2 | 0.939 ± 0.101 | 0.953 ± 0.061 | 0.947 ± 0.096 |
| 2.5 | v_3 | 1.052 ± 0.054 | 1.077 ± 0.035 | 1.003 ± 0.051 |
| 6.5 | v_4 | 1.0 (fixed) | 1.0 (fixed) | 1.0 (fixed) |
| 10.0 | v_5 | 0.954 (interpolated) | 0.932 (interpolated) | 0.998 (interpolated) |

Table 6.3: Time acceptance parameters for events in category [Run-II,L0-TOS].

| Knot position | Coefficient | $B_s^0 \rightarrow D_s K\pi\pi$ data | $B_s^0 \rightarrow D_s K\pi\pi$ MC | Ratio |
|---------------|-------------|--------------------------------------|------------------------------------|----------------------|
| 0.4 | v_0 | 0.486 ± 0.009 | 0.482 ± 0.009 | 1.000 ± 0.000 |
| 0.8 | v_1 | 0.691 ± 0.014 | 0.707 ± 0.015 | 1.000 ± 0.000 |
| 1.6 | v_2 | 0.851 ± 0.024 | 0.926 ± 0.026 | 1.000 ± 0.000 |
| 2.5 | v_3 | 1.061 ± 0.017 | 1.086 ± 0.018 | 1.000 ± 0.000 |
| 6.5 | v_4 | 1.0 (fixed) | 1.0 (fixed) | 1.0 (fixed) |
| 10.0 | v_5 | 0.946 (interpolated) | 0.925 (interpolated) | 1.000 (interpolated) |

Table 6.4: Time acceptance parameters for events in category [Run-II,L0-TIS].

| Knot position | Coefficient | $B_s^0 \rightarrow D_s K\pi\pi$ data | $B_s^0 \rightarrow D_s K\pi\pi$ MC | Ratio |
|---------------|-------------|--------------------------------------|------------------------------------|----------------------|
| 0.4 | v_0 | 0.300 ± 0.007 | 0.482 ± 0.010 | 1.000 ± 0.000 |
| 0.8 | v_1 | 0.476 ± 0.012 | 0.707 ± 0.016 | 1.000 ± 0.000 |
| 1.6 | v_2 | 0.725 ± 0.023 | 0.926 ± 0.026 | 1.000 ± 0.000 |
| 2.5 | v_3 | 1.064 ± 0.019 | 1.086 ± 0.018 | 1.000 ± 0.000 |
| 6.5 | v_4 | 1.0 (fixed) | 1.0 (fixed) | 1.0 (fixed) |
| 10.0 | v_5 | 0.944 (interpolated) | 0.925 (interpolated) | 1.000 (interpolated) |

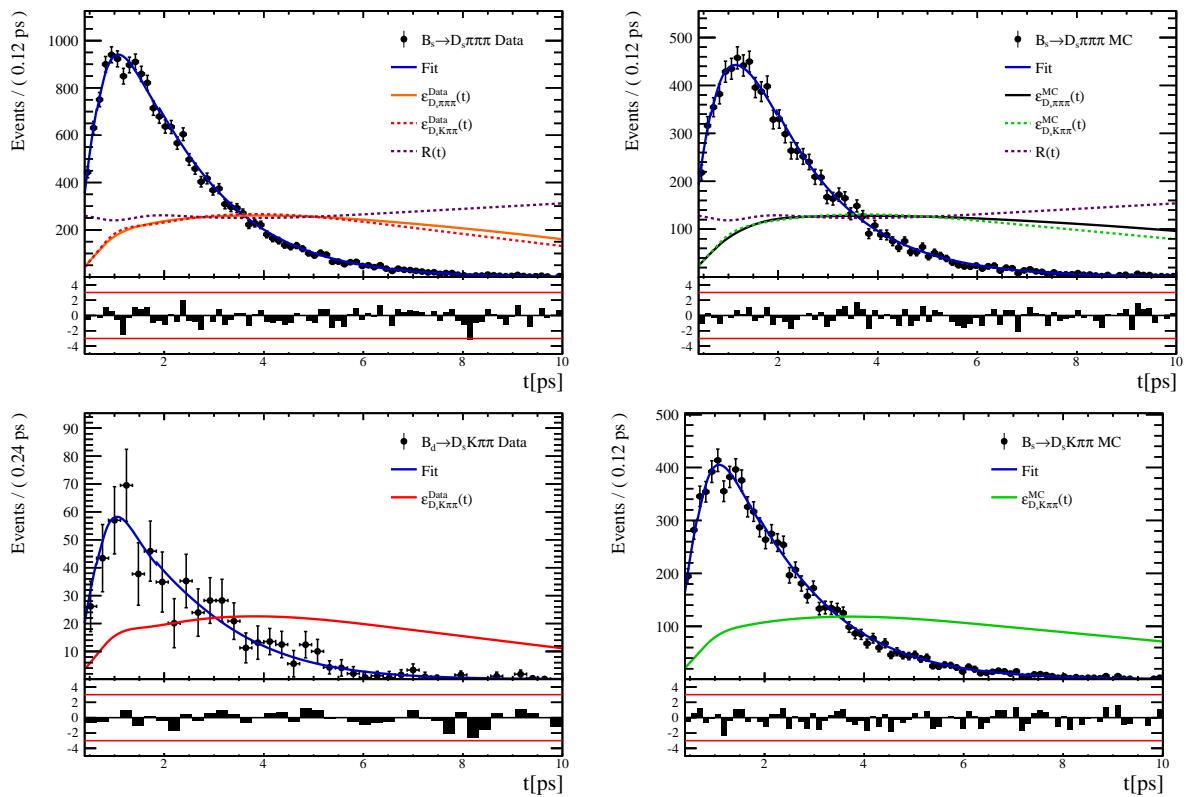


Figure 6.8

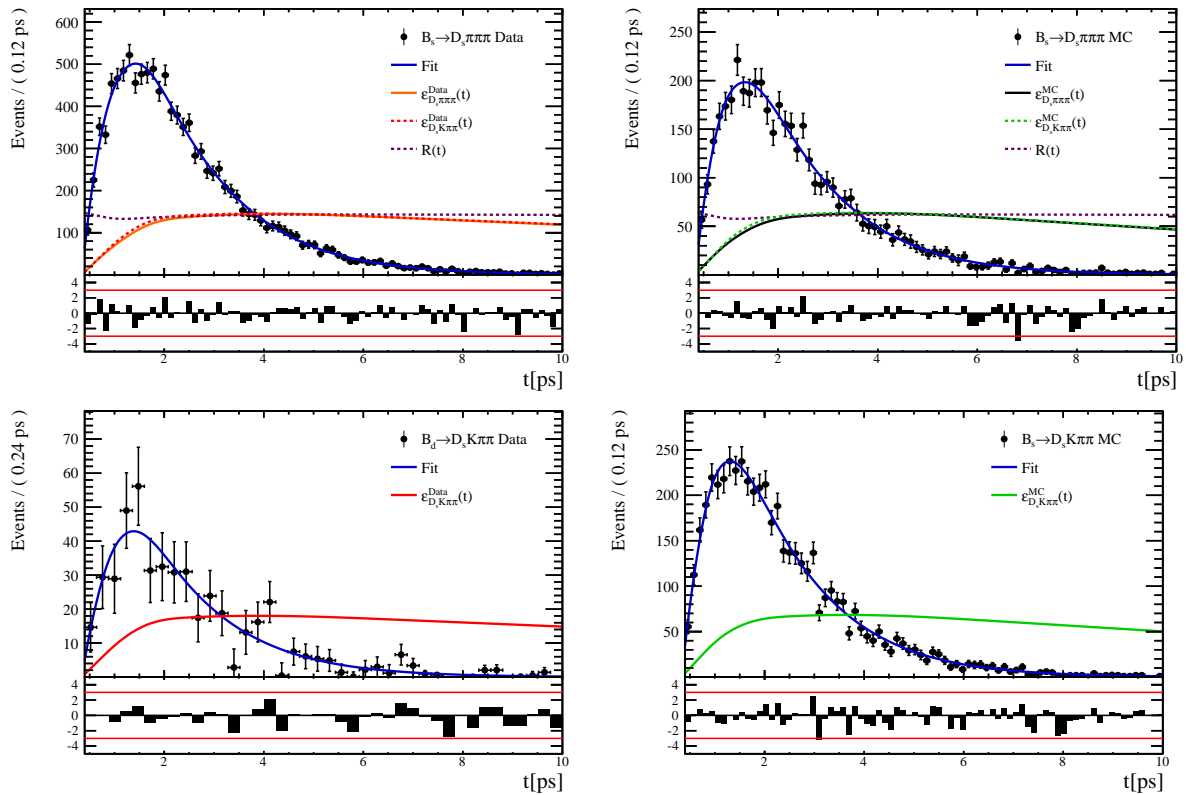


Figure 6.9

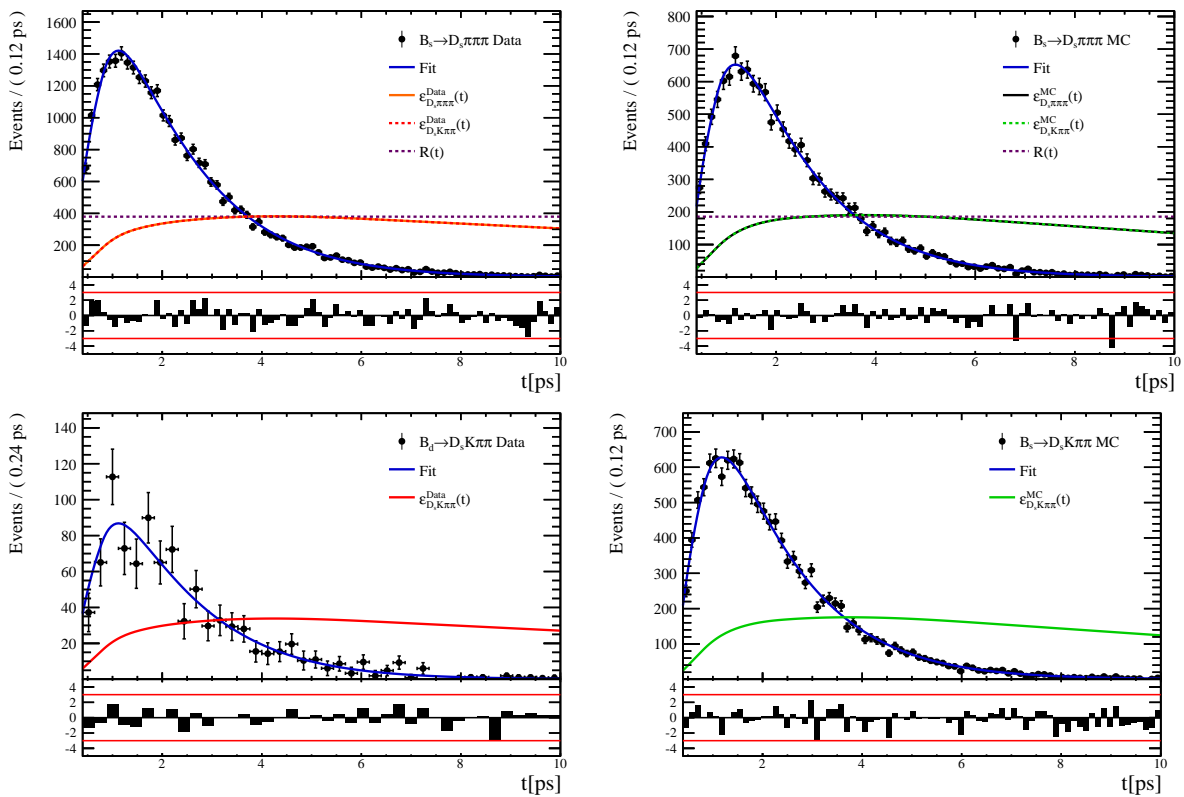


Figure 6.10

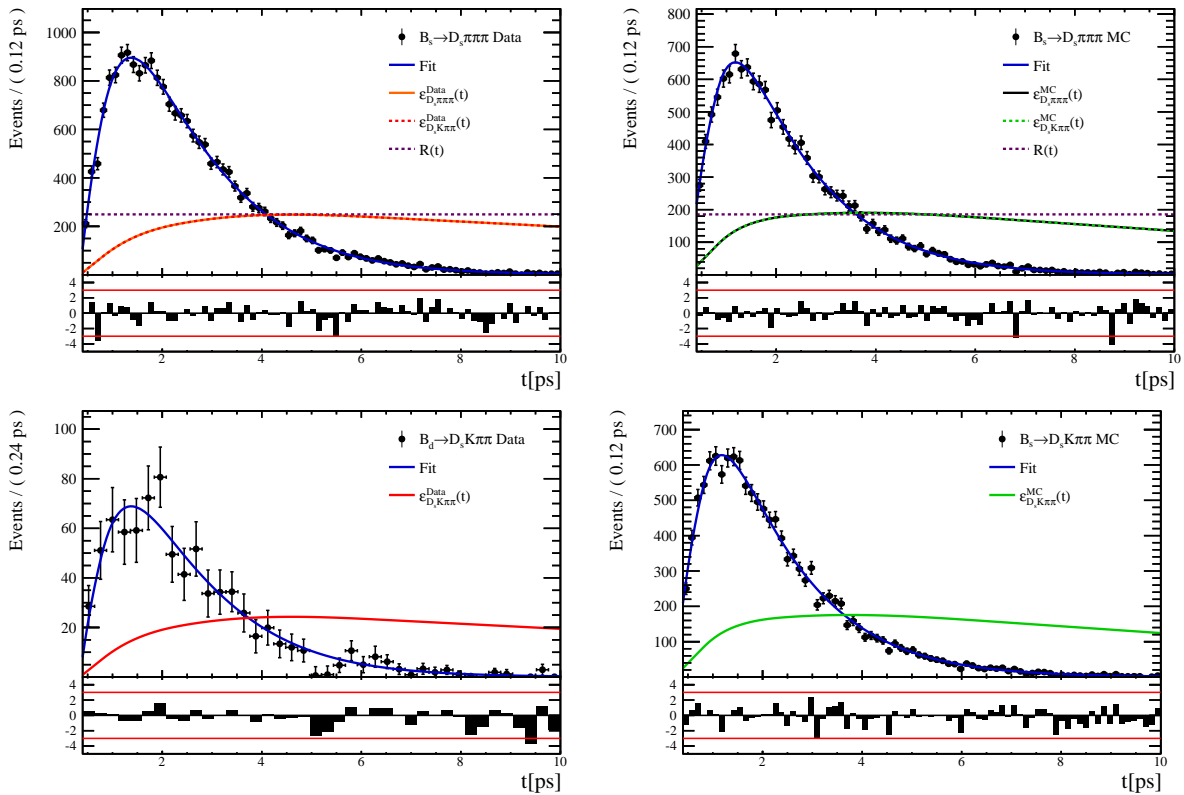


Figure 6.11

⁵⁷⁴ **6.3 Phasespace acceptance**

575 7 Decay-time Resolution

576 The observed oscillation of B mesons is prone to dilution, if the detector resolution is
 577 of similar magnitude as the oscillation period. In the B_s^0 system, considering that the
 578 measured oscillation frequency of the B_s^0 [33] and the average LHCb detector resolution [38]
 579 are both $\mathcal{O}(50 \text{ fs}^{-1})$, this is the case. Therefore, it is crucial to correctly describe the
 580 decay time resolution in order to avoid a bias on the measurement of time dependent CP
 581 violation. Since the time resolution depends on the particular event, especially the decay
 582 time itself, the sensitivity on γ can be significantly improved by using an event dependent
 583 resolution model rather than an average resolution. For this purpose, we use the per-event
 584 decay time error that is estimated based on the uncertainty obtained from the global
 585 kinematic fit of the momenta and vertex positions (DTF) with additional constraints on
 586 the PV position and the D_s mass. In order to apply it correctly, it has to be calibrated.
 587 The raw decay time error distributions for $B_s^0 \rightarrow D_s\pi\pi\pi$ signal candidates are shown in
 588 Figure 7.1 for Run-I and Run-II data. Significant deviations between the two different
 589 data taking periods are observed due to the increase in center of mass energy from Run-I
 590 to Run-II, as well as (among others) new tunings in the pattern and vertex reconstruction.
 591 The decay time error calibration is consequently performed separately for both data taking
 592 periods.

593 For Run-I data, we use the calibration from the closely related $B_s^0 \rightarrow D_s K$ analysis
 594 which was performed on a data sample of prompt- D_s candidates combined with a random
 595 pion track from the PV. We verify the portability to our decay channel on MC.

596 For Run-II data, a new lifetime unbiased stripping line (LTUB) has been implemented
 597 which selects prompt- D_s candidates combined with random $K\pi\pi$ tracks from the PV.

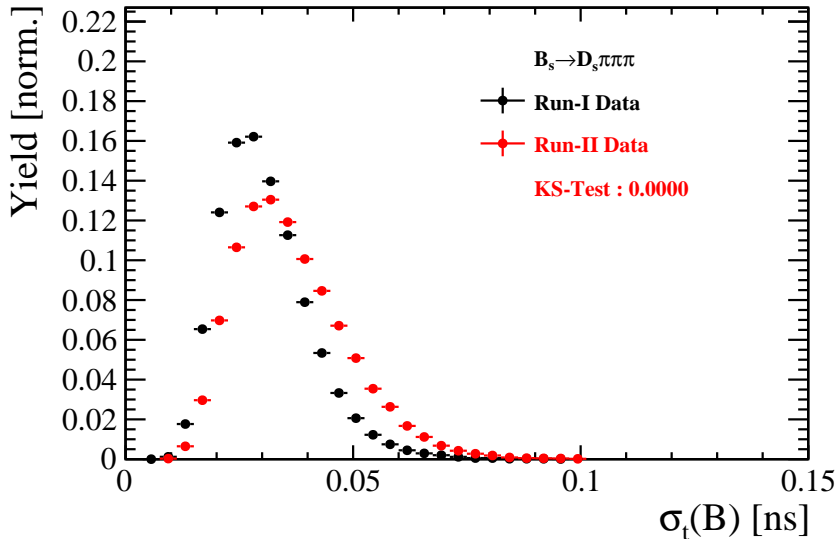


Figure 7.1: Distribution of the decay time error for $B_s^0 \rightarrow D_s\pi\pi\pi$ signal candidates for Run-I (black) and Run-II (red) data (sWeighted).

598 7.1 Calibration for Run-I data

599 For simulated $B_s^0 \rightarrow D_s K \pi\pi$ events, the spread of the differences between reconstructed
600 decay time and true decay time, $\Delta t = t - t_{true}$, is a direct measure of the decay time
601 resolution. The sum of two Gaussian pdfs with common mean but different widths is used
602 to fit the distribution of the decay time difference Δt as shown in Fig. 7.2. The effective
603 damping of the CP amplitudes due to the finite time resolution is described by the dilution
604 \mathcal{D} . In the case of infinite precision, there would be no damping and therefore $\mathcal{D} = 1$ would
605 hold, while for a resolution that is much larger than the B_s^0 oscillation frequency, \mathcal{D} would
606 approach 0. For a double-Gaussian resolution model, the dilution is given by [39]

$$\mathcal{D} = f_1 e^{-\sigma_1^2 \Delta m_s^2 / 2} + (1 - f_1) e^{-\sigma_2^2 \Delta m_s^2 / 2}, \quad (7.1)$$

607 where σ_1 and σ_2 are the widths of the Gaussians, f_1 is the relative fraction of events
608 described by the first Gaussian relative to the second and Δm_s is the oscillation frequency
609 of B_s^0 mesons. An effective single Gaussian width is calculated from the dilution as,

$$\sigma_{eff} = \sqrt{(-2/\Delta m_s^2) \ln \mathcal{D}}, \quad (7.2)$$

610 which converts the resolution into a single-Gaussian function with an effective resolution
611 that causes the same damping effect on the magnitude of the B_s oscillation. For the Run-I
612 $B_s^0 \rightarrow D_s K \pi\pi$ MC sample the effective average resolution is found to be $\sigma_{eff} = 39.1 \pm 0.3$ fs.

613 To analyze the relation between the per-event decay time error δ_t and the actual
614 resolution σ_t , the simulated $B_s^0 \rightarrow D_s K \pi\pi$ sample is divided into equal-statistics slices of
615 δ_t . For each slice, the effective resolution is determined as described above. Details of the
616 fit results in each slice are shown in appendix D. Figure 7.2 shows the obtained values
617 for σ_{eff} as a function of the per-event decay time error σ_t . To account for the variable
618 binning, the bin values are not placed at the bin center but at the weighted mean of the
619 respective per-event-error bin. A linear function is used to parametrize the distribution.
620 The obtained values are

$$\sigma_{eff}^{MC}(\sigma_t) = (0.0 \pm 0.0) \text{ fs} + (1.232 \pm 0.010) \sigma_t \quad (7.3)$$

621 where the offset is fixed to 0. For comparison, the calibration function found for $B_s^0 \rightarrow D_s K$
622 MC is also shown in Figure 7.2 [39]:

$$\sigma_{eff}^{D_s K, MC}(\sigma_t) = (0.0 \pm 0.0) \text{ fs} + (1.201 \pm 0.013) \sigma_t. \quad (7.4)$$

623 Due to the good agreement between the scale factors for $B_s^0 \rightarrow D_s K$ and $B_s^0 \rightarrow D_s K \pi\pi$
624 MC, we conclude that the resolution calibration for $B_s^0 \rightarrow D_s K$ data:

$$\sigma_{eff}^{D_s K}(\sigma_t) = (10.26 \pm 1.52) \text{ fs} + (1.280 \pm 0.042) \sigma_t \quad (7.5)$$

625 can be used for our analysis. The following calibration functions were used in the
626 $B_s^0 \rightarrow D_s K$ analysis to estimate the systematic uncertainty on the decay-time resolution:

$$\sigma_{eff}^{D_s K}(\sigma_t) = (-0.568 \pm 1.570) \text{ fs} + (1.243 \pm 0.044) \sigma_t \quad (7.6)$$

$$\sigma_{eff}^{D_s K}(\sigma_t) = (0.0 \pm 0.0) \text{ fs} + (1.772 \pm 0.012) \sigma_t \quad (7.7)$$

628 The difference of the scale factors observed on $B_s^0 \rightarrow D_s K$ and $B_s^0 \rightarrow D_s K \pi\pi$ MC is
629 assigned as additional systematic uncertainty.

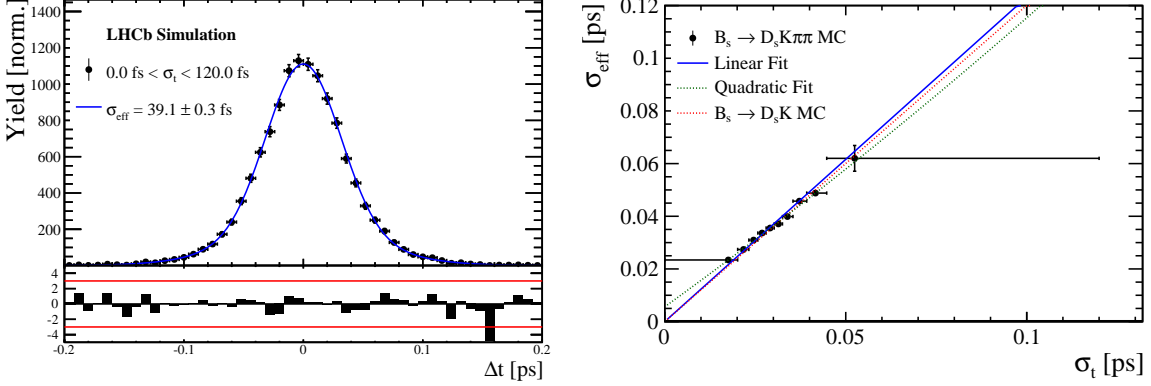


Figure 7.2: (Left) Difference of the true and measured decay time of $B_s^0 \rightarrow D_s K\pi\pi$ MC candidates. (Right) The measured resolution σ_{eff} as function of the per-event decay time error estimate σ_t for $B_s \rightarrow D_s K\pi\pi$ MC (Run-I). The fitted calibration curve is shown in blue.

630 7.2 Calibration for Run-II data

631 For the resolution calibration of Run-II data, a sample of promptly produced D_s candidates
 632 is selected using the B02DsKPiPiLTUBD2HHHBeauty2CharmLine stripping line. This
 633 lifetime-unbiased stripping line does not apply selection requirements related to lifetime
 634 or impact parameter, allowing for a study of the resolution. In order to reduce the rate
 635 of this sample it is pre-scaled in the stripping. Each D_s candidate is combined with a
 636 random kaon track and two random pion tracks which originate from the PV to obtain a
 637 sample of fake B_s candidates with a known true decay-time of $t_{true} = 0$. The difference of
 638 the measured decay time, t , of these candidates with respect to the true decay time is
 639 attributed to the decay time resolution.

640 The offline selection of the fake B_s candidates is summarized in Tab. 7.1. The selection
 641 is similar than the one for real data with the important difference that the D_s candidate
 642 is required to come from the PV by cutting on the impact parameter significance. Even
 643 after the full selection, a significant number of multiple candidates is observed. These
 644 are predominantly fake B_s candidates that share the same D_s candidate combined with
 645 different random tracks from the PV. We select one of these multiple candidates randomly
 646 which retains approximately 20% of the total candidates. The invariant mass distribution
 647 of the selected D_s candidates is shown in Fig. 7.3. To separate true D_s candidates from
 648 random combinations, the `sPlot` method is used to statistically subtract combinatorial
 649 background from the sample.

650 Figure 7.4 shows the `sWeighted` decay-time distribution for fake B_s candidates. Similar
 651 as in the previous section, the decay-time distribution is fitted with a double-Gaussian
 652 resolution model in slices of the per-event decay time error. Since some D_s candidates
 653 might actually originate from true B_s decays, the decay-time distribution of the fake B_s
 654 candidates might show a bias towards positive decay times. Therefore, we determine the
 655 decay-time resolution from the negative decay-time distribution only. Details of the fit
 656 results in each slice are shown in appendix D. The resulting calibration function:

$$\sigma_{eff}^{Data}(\sigma_t) = (9.7 \pm 1.7) \text{ fs} + (0.915 \pm 0.040) \sigma_t \quad (7.8)$$

657 is in good agreement with the one obtained for the $B_s \rightarrow J/\psi\phi$ (Run-II) analysis.

$$\sigma_{eff}^{J/\psi\phi}(\sigma_t) = (12.25 \pm 0.33) \text{ fs} + (0.8721 \pm 0.0080) \sigma_t \quad (7.9)$$

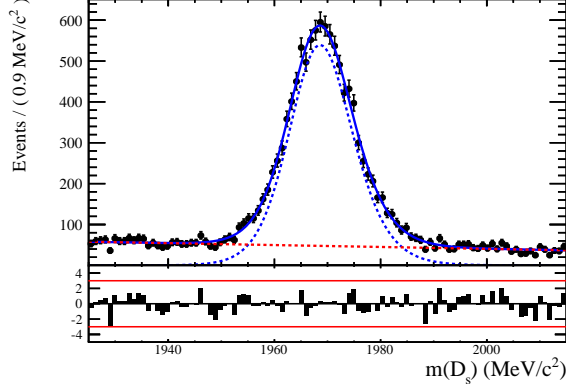


Figure 7.3: The invariant mass distribution for prompt D_s candidates.

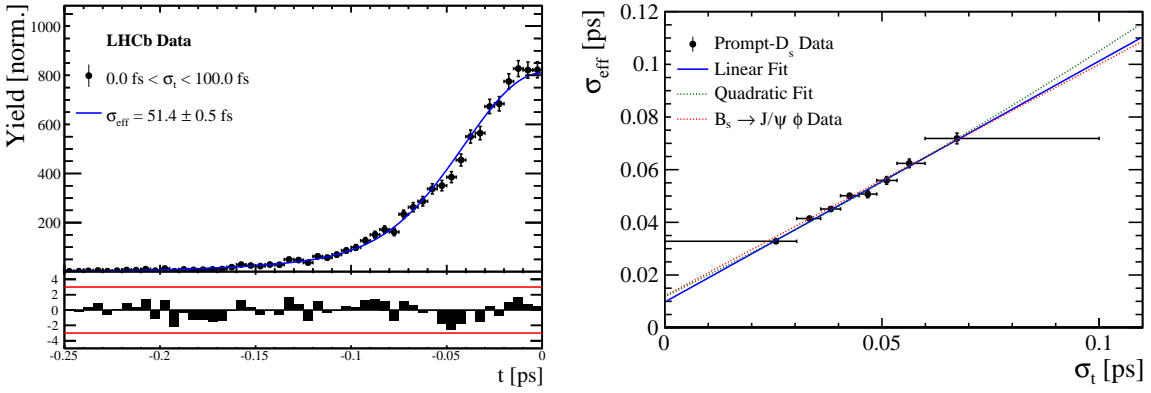


Figure 7.4: (Left) Decay-time distribution for fake B_s candidates from promptly produced D_s candidates, combined with random prompt $K\pi\pi$ bachelor tracks. (Right) The measured resolution σ_{eff} as function of the per-event decay time error estimate σ_t for fake B_s candidates (Run-II data). The fitted calibration curve is shown in blue.

Table 7.1: Offline selection requirements for fake B_s candidates from promptly produced D_s candidates combined with random prompt $K\pi\pi$ bachelor tracks.

| | Description | Requirement |
|------------------------------------|----------------------------|--|
| $B_s \rightarrow D_s K\pi\pi$ | χ^2_{vtx}/ndof | < 8 |
| | χ^2_{DTF}/ndof | < 15 |
| | t | < 0 ps |
| $D_s \rightarrow hhh$ | χ^2_{vtx}/ndof | < 5 |
| | DIRA | > 0.99994 |
| | χ^2_{FD} | > 9 |
| | p_T | > 1800 MeV |
| | χ^2_{IP} | < 9 |
| | $\chi^2_{IP}(h)$ | > 5 |
| | Wrong PV veto | $nPV = 1 \parallel \min(\Delta\chi^2_{IP}) > 20$ |
| $D_s^- \rightarrow KK\pi^-$ | D^0 veto | $m(KK) < 1840$ MeV |
| | D^- veto | $m(K^+K_\pi^-\pi^-) \neq m(D^-) \pm 30$ MeV |
| | Λ_c veto | $m(K^+K_p^-\pi^-) \neq m(\Lambda_c) \pm 30$ MeV |
| $D_s^- \rightarrow \phi\pi^-$ | $m(KK)$ | $= m_\phi \pm 20$ MeV |
| | PIDK(K^+) | > -10 |
| | PIDK(K^-) | > -10 |
| | PIDK(π^-) | < 20 |
| $D_s^- \rightarrow K^*(892)K^-$ | $m(KK)$ | $\neq m_\phi \pm 20$ MeV |
| | $m(K^+\pi^-)$ | $= m_{K^*(892)} \pm 75$ MeV |
| | PIDK(K^+) | > -10 |
| | PIDK(K^-) | > -5 |
| | PIDK(π^-) | < 20 |
| $D_s^- \rightarrow (KK\pi^-)_{NR}$ | $m(KK)$ | $\neq m_\phi \pm 20$ MeV |
| | $m(K^+\pi^-)$ | $\neq m_{K^*(892)} \pm 75$ MeV |
| | PIDK(K^+) | > 5 |
| | PIDK(K^-) | > 5 |
| | PIDK(π^-) | < 10 |
| $D_s \rightarrow \pi\pi\pi$ | PIDK(h) | < 10 |
| | PIDp(h) | < 10 |
| | D^0 veto | $m(\pi^+\pi^-) < 1700$ MeV |
| $X_s \rightarrow K\pi\pi$ | $\chi^2_{IP}(h)$ | < 40 |
| | PIDK(K) | > 10 |
| | PIDK(π) | < 5 |
| | isMuon(h) | False |
| All tracks | p_T | > 500 MeV |

658 **7.3 Cross-checks**

659 **7.3.1 Kinematic dependence**

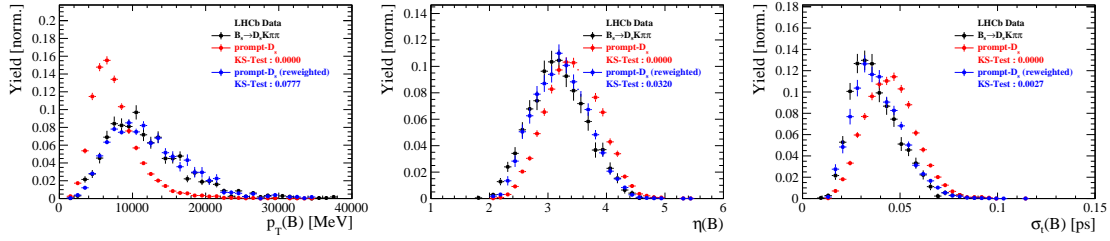


Figure 7.5

660 **7.3.2 DTF constraints**

661 8 Production and Detection Asymmetries

662 8.1 B_s Production Asymmetry

663 The production rates of b and \bar{b} hadrons in pp collisions are not expected to be identical,
 664 therefore this effect must be taken into account when computing CP asymmetries. The
 665 production asymmetry for B_s mesons is defined as:

$$A_p(B_s^0) = \frac{\sigma(\bar{B}_s^0) - \sigma(B_s^0)}{\sigma(\bar{B}_s^0) + \sigma(B_s^0)} \quad (8.1)$$

666 where σ are the corresponding production cross-section. This asymmetry was measured
 667 by LHCb in pp collisions at $\sqrt{s} = 7$ TeV and $\sqrt{s} = 8$ TeV by means of a time-dependent
 668 analysis of $B_s \rightarrow D_s^- \pi^+$ decays [40]. The results in bins of p_T and η of the B_s meson
 669 are shown in Table 8.1. To correct for the different kinematics of $B_s \rightarrow D_s^- \pi^+$ and
 670 $B_s^0 \rightarrow D_s K \pi \pi$ decays, the measured B_s production asymmetries $A_p(p_T, \eta)$ are folded with
 671 the sWeighted p_T, η distribution of our signal channel. The resulting effective production
 672 asymmetries are:

$$A_p(B_s^0)_{2011} = (-0.506 \pm 1.90)\% \quad (8.2)$$

$$A_p(B_s^0)_{2012} = (-0.164 \pm 1.30)\% \quad (8.3)$$

$$A_p(B_s^0)_{\text{Run-I}} = (-0.045 \pm 1.04)\%. \quad (8.4)$$

673 As for Run-II data no measurement is available yet, we determine the production asym-
 674 metry from $B_s \rightarrow D_s \pi \pi \pi$ data together with the tagging parameters.

Table 8.1: B_s production asymmetries in kinematic bins for 2011 and 2012 data. [40]

| p_T [GeV/c] | η | $A_p(B_s^0)_{\sqrt{s}=7 \text{ TeV}}$ | $A_p(B_s^0)_{\sqrt{s}=8 \text{ TeV}}$ |
|-----------------|--------------|---------------------------------------|---------------------------------------|
| (2.00, 7.00) | (2.10, 3.00) | $0.0166 \pm 0.0632 \pm 0.0125$ | $0.0412 \pm 0.0416 \pm 0.0150$ |
| (2.00, 7.00) | (3.00, 3.30) | $0.0311 \pm 0.0773 \pm 0.0151$ | $-0.0241 \pm 0.0574 \pm 0.0079$ |
| (2.00, 7.00) | (3.30, 4.50) | $-0.0833 \pm 0.0558 \pm 0.0132$ | $0.0166 \pm 0.0391 \pm 0.0092$ |
| (7.00, 9.50) | (2.10, 3.00) | $0.0364 \pm 0.0479 \pm 0.0068$ | $0.0482 \pm 0.0320 \pm 0.0067$ |
| (7.00, 9.50) | (3.00, 3.30) | $0.0206 \pm 0.0682 \pm 0.0127$ | $0.0983 \pm 0.0470 \pm 0.0155$ |
| (7.00, 9.50) | (3.30, 4.50) | $0.0058 \pm 0.0584 \pm 0.0089$ | $-0.0430 \pm 0.0386 \pm 0.0079$ |
| (9.50, 12.00) | (2.10, 3.00) | $-0.0039 \pm 0.0456 \pm 0.0121$ | $0.0067 \pm 0.0303 \pm 0.0063$ |
| (9.50, 12.00) | (3.00, 3.30) | $0.1095 \pm 0.0723 \pm 0.0179$ | $-0.1283 \pm 0.0503 \pm 0.0171$ |
| (9.50, 12.00) | (3.30, 4.50) | $0.1539 \pm 0.0722 \pm 0.0212$ | $-0.0500 \pm 0.0460 \pm 0.0104$ |
| (12.00, 30.00) | (2.10, 3.00) | $-0.0271 \pm 0.0336 \pm 0.0061$ | $-0.0012 \pm 0.0222 \pm 0.0050$ |
| (12.00, 30.00) | (3.00, 3.30) | $-0.0542 \pm 0.0612 \pm 0.0106$ | $0.0421 \pm 0.0416 \pm 0.0162$ |
| (12.00, 30.00) | (3.30, 4.50) | $-0.0586 \pm 0.0648 \pm 0.0150$ | $0.0537 \pm 0.0447 \pm 0.0124$ |

675 8.2 $K^-\pi^+$ Detection Asymmetry

676 The presented measurement of the CKM-angle γ using $B_s^0 \rightarrow D_s K\pi\pi$ decays is sensitive
 677 to a possible charge asymmetry of the kaon. This effect can be detector induced, because
 678 kaons are known to have a nuclear cross-section which is asymmetrically dependent on
 679 the sign of their charge. It is indispensable to determine the detector induced charge
 680 asymmetry of the kaon, as fitting without taking this effect into account would introduce
 681 a 'fake' CP violation. Instead of determining the single track detection asymmetry of a
 682 kaon, it is found that the combined two track asymmetry of a kaon-pion pair is much
 683 easier to access [41]. Therefore the two track asymmetry is used, which is defined as

$$A^{det}(K^-\pi^+) = \frac{\epsilon^{det}(K^-\pi^+) - \epsilon^{det}(K^+\pi^-)}{\epsilon^{det}(K^-\pi^+) + \epsilon^{det}(K^+\pi^-)}. \quad (8.5)$$

684 This asymmetry can be measured from the difference in asymmetries in the $D^+ \rightarrow K^-\pi^+\pi^+$
 685 and $D^+ \rightarrow K_s^0\pi^+$ modes [42]:

$$\begin{aligned} A^{det}(K^-\pi^+) &= \frac{N(D^+ \rightarrow K^-\pi^+\pi^+) - N(D^- \rightarrow K^+\pi^-\pi^-)}{N(D^+ \rightarrow K^-\pi^+\pi^+) + N(D^- \rightarrow K^+\pi^-\pi^-)} \\ &\quad - \frac{N(D^+ \rightarrow K_s^0\pi^+) - N(D^- \rightarrow K_s^0\pi^-)}{N(D^+ \rightarrow K_s^0\pi^+) + N(D^- \rightarrow K_s^0\pi^-)} \\ &\quad - A(K^0), \end{aligned} \quad (8.6)$$

686 where possible CP violation in the $D^+ \rightarrow K_s^0\pi^+$ mode is predicted to be smaller than
 687 10^{-4} in the Standard Model [43]. The asymmetry in the neutral kaon system, $A(K^0)$, has
 688 to be taken into account as a correction.

689 We use a dedicated LHCb tool to determine $A^{det}(K^-\pi^+)$ for all data taking periods
 690 used in this analysis. A detailed description can be found in [42]. The tool provides
 691 large calibration samples of $D^\pm \rightarrow K^\pm\pi^\pm\pi^\pm$ and $D^\pm \rightarrow K_s^0\pi^\pm$ decays, which are used to
 692 determine the asymmetry following Eq. 8.6. Several weighting steps are performed to
 693 match the kinematics of the calibration samples to our signal decay sample:

694 First, weights are assigned to the K^\pm and π^\pm of the $D^\pm \rightarrow K^\pm\pi^\pm\pi^\pm$ sample, using
 695 p, η of the K^\pm and p_T, η of the π^\pm from our $B_s^0 \rightarrow D_s K\pi\pi$ signal decay. Then, weights
 696 are assigned to the $D^\pm (p_T, \eta)$ and the $\pi^\pm (p_T)$ of the $D^\pm \rightarrow K_s^0\pi^\pm$ sample to match
 697 the corresponding, weighted distributions of the $D^\pm \rightarrow K^\pm\pi^\pm\pi^\pm$ sample. In a last
 698 step, weights are assigned to match the bachelor pions ϕ distributions between the two
 699 calibration samples.

700 After the samples are weighted, fits are performed to the invariant
 701 $m(K^-\pi^+\pi^+)/m(K^+\pi^-\pi^-)$ and $m(K_s^0\pi^+)/m(K_s^0\pi^-)$ distributions to determine
 702 $A^{det}(K^-\pi^+)$. The PDFs used to describe the invariant mass distributions consist of
 703 gaussian functions for the signal component and exponentials describing the residual
 704 background.

705 The detection asymmetry is determined separately for every year and (since it is a
 706 charge asymmetry effect) magnet polarity. Serving as an example for Run-I and Run-
 707 II, the fits used to determine $N(D^+ \rightarrow K^-\pi^+\pi^+)/N(D^- \rightarrow K^+\pi^-\pi^-)$ and $N(D^+ \rightarrow$
 708 $K_s^0\pi^+)/N(D^- \rightarrow K_s^0\pi^-)$ for 2011, magnet up data and 2015, magnet up data are shown
 709 in Fig. 8.1 and 8.2 respectively. The obtained values of $A^{det}(K^-\pi^+) + A(K^0)$ for all years
 710 and polarities are shown in Table 8.2.

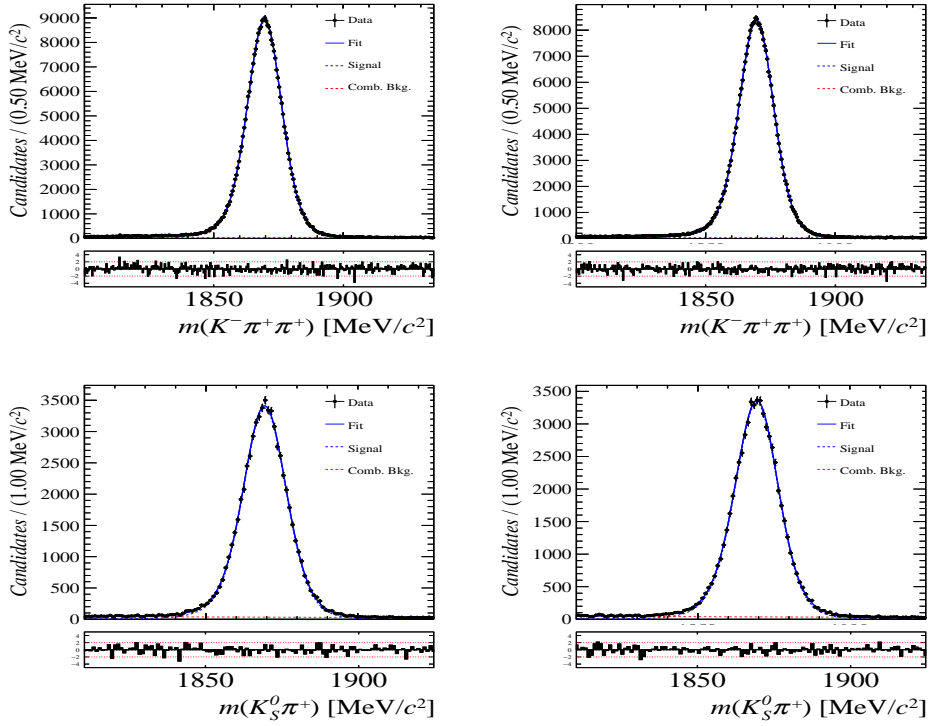


Figure 8.1: Distributions of the invariant mass of (top) $D^\pm \rightarrow K^\pm \pi^\pm \pi^\pm$ and (bottom) $D^\pm \rightarrow K_s^0 \pi^\pm$ candidates for Run-I data from the calibration samples. A fit described in the text is overlaid.

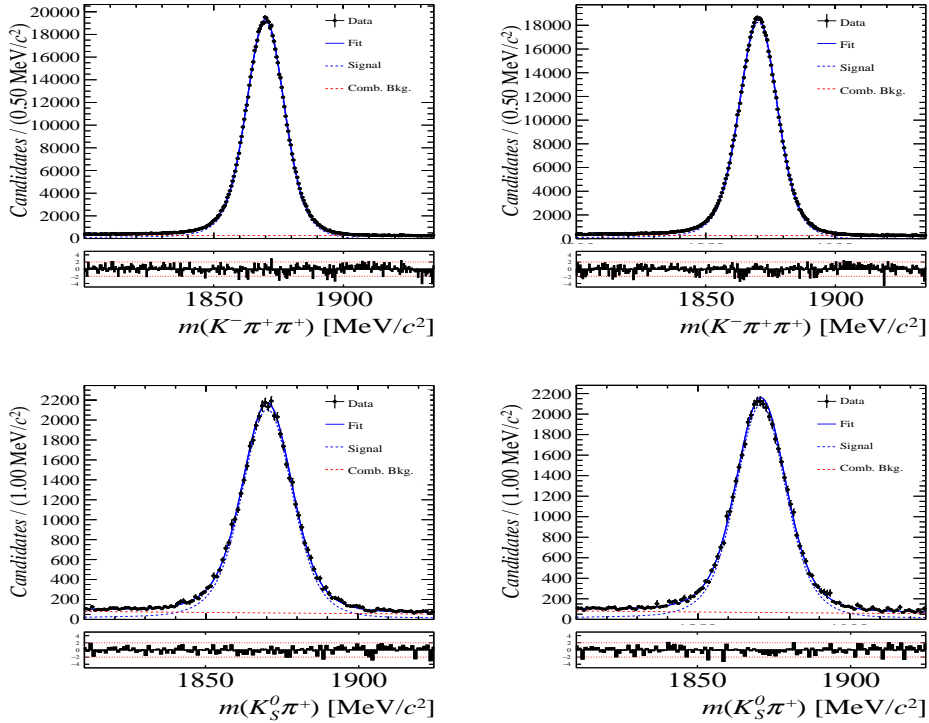


Figure 8.2: Distributions of the invariant mass of (top) $D^\pm \rightarrow K^\pm \pi^\pm \pi^\pm$ and (bottom) $D^\pm \rightarrow K_s^0 \pi^\pm$ candidates for Run-II data from the calibration samples. A fit described in the text is overlaid.

| Data sample | $A^{det}(K^-\pi^+) + A(K^0)$ [%] |
|-----------------|----------------------------------|
| Run-I | |
| 2011, mag. up | -2.01 \pm 0.32 |
| 2011, mag. down | -0.16 \pm 0.28 |
| 2011, average | -1.09 \pm 0.21 |
| 2012, mag. up | -0.90 \pm 0.20 |
| 2012, mag. down | -1.01 \pm 0.22 |
| 2012, average | -0.96 \pm 0.15 |
| Run-II | |
| 2015, mag. up | -1.36 \pm 0.36 |
| 2015, mag. down | -0.96 \pm 0.24 |
| 2015, average | -1.16 \pm 0.22 |
| 2016, mag. up | 0.50 \pm 0.88 |
| 2016, mag. down | 1.23 \pm 0.72 |
| 2016, average | 0.87 \pm 0.57 |

Table 8.2: Summary of the $K^-\pi^+$ detection asymmetry obtained from the fits to the Run-I and Run-II calibration samples.

9 Time dependent fit

This section will cover the phasespace integrated, time dependent fit to $B_s^0 \rightarrow D_s h\pi\pi$ data, which is described by the PDF formulated in Eq. 2.6. For the phasespace integrated fit to $B_s^0 \rightarrow D_s K\pi\pi$ data, the sensitivity to the CKM phase γ will depend on the magnitude of the coherence factor κ , defined in Eq. 2.10, which is added as an additional fit parameter. In order to avoid any pollution of the final data samples by background events, both samples are weighted using the sWeights obtained by the fits to the invariant mass distributions, described in Sec. 4. This fit approach is commonly known as *sFit*. As additional input to the fit, the tagging information (Sec. 5), as well as the decay time acceptance (Sec. 6) and resolution (Sec. 7) is used and fixed to the values obtained by the dedicated studies. Taking all inputs into account, the final time dependent fit PDF is given by

$$\mathcal{P}\mathcal{D}\mathcal{F}(t, \vec{\lambda}) = \left(\epsilon(t) \cdot \int P(x, t, q_t, q_f) dx \right) \times \mathcal{R}(t - t'), \quad (9.1)$$

where $\int P(x, t, q_t, q_f) dx$ is the PDF given by Eq. 2.6, $\epsilon(t)$ is the efficiency due to the time acceptance effects and $\mathcal{R}(t - t')$ is the Gaussian time resolution function.

9.1 sFit to $B_s^0 \rightarrow D_s \pi\pi\pi$ data

The phasespace-integrated, time-dependent fit is performed to the full sWeighted sample of selected candidates from Run I and 2015+2016 Run II data, containing both possible magnet polarities and D_s final states. In the fit, the values of Γ_s and $\Delta\Gamma_s$ are fixed to the latest PDG report. All tagging parameters are fixed to the central values found in the tagging calibration, described in Sec. 5. Due to the fact that the $B_s^0 \rightarrow D_s \pi\pi\pi$ decay is flavour specific, the CP-coefficients can be fixed to $C = 1$ and $D_f = D_{\bar{f}} = S_f = S_{\bar{f}} = 0$, reducing Eq. 2.6 to

$$\int P(x, t, q_t, q_f) dx = [\cosh\left(\frac{\Delta\Gamma t}{2}\right) + q_t q_f C \cos(m_s t)] e^{-\Gamma t}. \quad (9.2)$$

Note that in this case, the dependence on the coherence factor κ is dropped and the same relation as found for $B_s^0 \rightarrow D_s \pi$ decays is recovered. Therefore, the only free fit parameter left is Δm_s . The data distribution with the overlaid fit is shown in Fig.

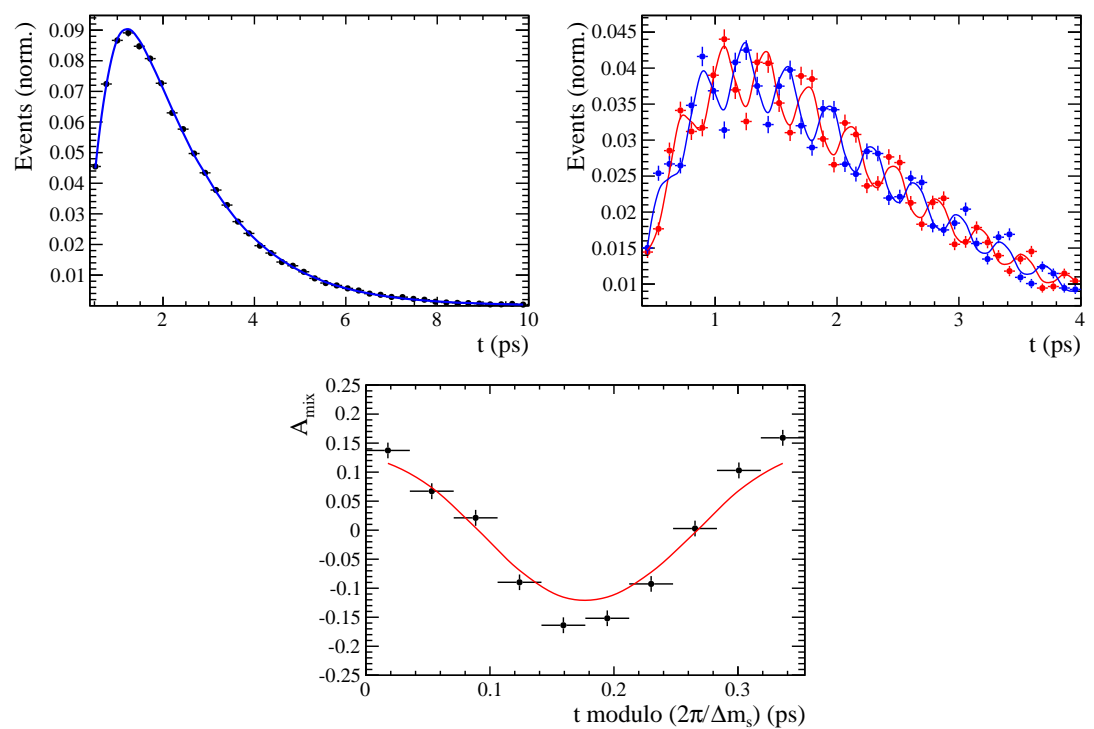


Figure 9.1

Table 9.1: Result of the phase-space integrated fit to $B_s \rightarrow D_s\pi\pi\pi$ data.

| Fit parameter | Value |
|---------------------------------|---|
| Run-I | p_0^{OS} 0.3896 ± 0.0101 |
| | p_1^{OS} 0.8883 ± 0.1074 |
| | Δp_0^{OS} 0.0161 ± 0.0104 |
| | Δp_1^{OS} 0.0005 ± 0.1095 |
| | $\epsilon_{tag}^{\text{OS}}$ 0.3851 ± 0.0031 |
| | $\Delta\epsilon_{tag}^{\text{OS}}$ 0.0069 ± 0.0123 |
| | p_0^{SS} 0.4465 ± 0.0075 |
| | p_1^{SS} 1.0748 ± 0.1012 |
| | Δp_0^{SS} -0.0190 ± 0.0076 |
| | Δp_1^{SS} 0.1016 ± 0.1063 |
| | $\epsilon_{tag}^{\text{SS}}$ 0.6882 ± 0.0029 |
| | $\Delta\epsilon_{tag}^{\text{SS}}$ -0.0076 ± 0.0117 |
| | A_p -0.0004 ± 0.0000 |
| Run-II | p_0^{OS} 0.3669 ± 0.0074 |
| | p_1^{OS} 0.9298 ± 0.0761 |
| | Δp_0^{OS} 0.0118 ± 0.0085 |
| | Δp_1^{OS} 0.0234 ± 0.0855 |
| | $\epsilon_{tag}^{\text{OS}}$ 0.3525 ± 0.0023 |
| | $\Delta\epsilon_{tag}^{\text{OS}}$ 0.0105 ± 0.0085 |
| | p_0^{SS} 0.4532 ± 0.0055 |
| | p_1^{SS} 0.9125 ± 0.0656 |
| | Δp_0^{SS} -0.0123 ± 0.0060 |
| | Δp_1^{SS} 0.1374 ± 0.0757 |
| | $\epsilon_{tag}^{\text{SS}}$ 0.6804 ± 0.0023 |
| | $\Delta\epsilon_{tag}^{\text{SS}}$ 0.0076 ± 0.0083 |
| | A_p -0.0042 ± 0.0091 |
| Δm_s xx.xx ± 0.0110 | |

₇₃₆ **9.2 sFit to $B_s^0 \rightarrow D_s K\pi\pi$ data**

Table 9.2: Result of the phase-space integrated fit to $B_s \rightarrow D_s K\pi\pi$ data.

| Fit parameter | Value |
|---------------|-------------------|
| C | xx.xx \pm 0.166 |
| D | xx.xx \pm 0.359 |
| \bar{D} | xx.xx \pm 0.333 |
| S | xx.xx \pm 0.247 |
| \bar{S} | xx.xx \pm 0.219 |

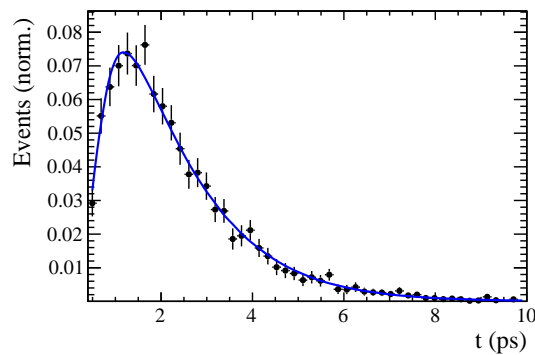


Figure 9.2

737 10 Time dependent amplitude fit

738 10.1 Signal Model Construction

739 The light meson spectrum comprises multiple resonances which are expected to contribute
 740 to $B_s \rightarrow D_s K\pi\pi$ decays as intermediate states. Apart from clear contributions coming
 741 from resonances such as $K_1(1270)$, $K_1(1400)$ $\rho(770)$ and $K^*(892)^0$, the remaining structure
 742 is impossible to infer due to the cornucopia of broad, overlapping and interfering resonances
 743 within the phase space boundary. The complete list of considered amplitudes can be
 744 found in Appendix F.

745 To build the amplitude model, one could successively add amplitudes on top of one
 746 another until a reasonable agreement between data and fit was achieved. However, this
 747 step-wise approach is not particularly suitable for amplitude analyses as discussed in
 748 Ref. [44]. Instead, we include the whole pool of amplitudes in the first instance and use
 749 the Least Absolute Shrinkage and Selection Operator [44, 45] (LASSO) approach to limit
 750 the model complexity. In this method, the event likelihood is extended by a penalty term

$$-2 \log \mathcal{L} \rightarrow -2 \log \mathcal{L} + \lambda \sum_i \sqrt{\int |a_i A_i(\mathbf{x})|^2 d\Phi_4}, \quad (10.1)$$

751 which shrinks the amplitude coefficients towards zero. The amount of shrinkage is
 752 controlled by the parameter λ , to be tuned on data. Higher values for λ encourage sparse
 753 models, *i.e.* models with only a few non-zero amplitude coefficients. The optimal value
 754 for λ is found by minimizing the Bayesian information criteria [46] (BIC),

$$\text{BIC}(\lambda) = -2 \log \mathcal{L} + r \log N_{\text{Sig}}, \quad (10.2)$$

755 where N_{Sig} is the number of signal events and r is the number of amplitudes with a decay
 756 fraction above a certain threshold. In this way, the optimal λ balances the fit quality
 757 ($-2 \log \mathcal{L}$) against the model complexity. The LASSO penalty term is only used to select
 758 the model. Afterwards, this term must be discarded in the final amplitude fit with the
 759 selected model, otherwise the parameter uncertainties would be biased.

760 The set of amplitudes is selected using the optimal value of $\lambda = 28$, and is henceforth
 761 called the LASSO model; Figure ??(a) shows the distribution of BIC values obtained by
 762 scanning over λ where we choose the decay fraction threshold to be 0.5%. In addition, we
 763 repeated the model selection procedure under multiple different conditions:

- 764 1. The fit fraction threshold for inclusion in the final model was varied within the
 765 interval [0.05, 5]%. The set of selected amplitudes is stable for thresholds between
 766 0.1% and 1%. Other choices result in marginally different models containing one
 767 component more or less.
 - 768 2. Instead of BIC, the Akaike information criteria ($\text{AIC}(\lambda) = -2 \log \mathcal{L} + 2r$ [47]) was
 769 used to optimize λ . For a given threshold, the AIC method tends to prefer lower
 770 λ values. However, the set of models obtained varying the threshold within the
 771 interval [0.05, 5]% is identical to the BIC method.
 - 772 3. The amplitudes selected under nominal conditions were excluded one-by-one from
 773 the set of all amplitudes considered.
- 774 From that we obtained a set of alternative models shown in Appendix ??.

775 **10.2 Results**

Table 10.1: Result of the time-dependent amplitude fit to $B_s \rightarrow D_s K\pi\pi$ data.

| Fit parameter | Value |
|---------------|-------------------|
| x_- | xx.xx \pm 0.352 |
| y_- | xx.xx \pm 0.159 |
| x_+ | xx.xx \pm 0.210 |
| y_+ | xx.xx \pm 0.162 |

Table 10.2: Fit fractions for $B_s \rightarrow D_s K\pi\pi$ data.

| Decay channel | Fraction [%] |
|---|-------------------|
| $B_s \rightarrow K(1)(1400)^+ (\rightarrow K^*(892) (\rightarrow K^+ \pi^-) \pi^+) D_s^-$ | 41.89 ± 5.17 |
| $B_s \rightarrow K(1)(1270)^+ (\rightarrow K(0)^*(1430) (\rightarrow K^+ \pi^-) \pi^+) D_s^-$ | 8.39 ± 1.53 |
| $B_s \rightarrow K(1)(1270)^+ (\rightarrow K^*(892) (\rightarrow K^+ \pi^-) \pi^+) D_s^-$ | 15.10 ± 3.24 |
| $B_s \rightarrow K(1)(1270)^+ (\rightarrow \rho(770)^0 (\rightarrow \pi^+ \pi^-) K^+) D_s^-$ | 13.31 ± 2.03 |
| $B_s \rightarrow K^*(1410)^+ (\rightarrow K^*(892) (\rightarrow K^+ \pi^-) \pi^+) D_s^-$ | 17.17 ± 1.62 |
| $B_s \rightarrow K^*(1410)^+ (\rightarrow \rho(770)^0 (\rightarrow \pi^+ \pi^-) K^+) D_s^-$ | 7.08 ± 0.93 |
| Sum | 102.95 ± 7.22 |

Table 10.3: Fit fractions for $B_s \rightarrow D_s K\pi\pi$ data.

| Decay channel | Fraction [%] |
|---|--------------------|
| $B_s \rightarrow K(1)(1400)^+ (\rightarrow K^*(892) (\rightarrow K^+ \pi^-) \pi^+) D_s^-$ | 72.16 ± 24.64 |
| $B_s \rightarrow K(1460)^+ (\rightarrow K^*(892) (\rightarrow K^+ \pi^-) \pi^+) D_s^-$ | 16.10 ± 10.42 |
| $B_s \rightarrow NonResS0 (\rightarrow D_s^- \pi^+) K^*(892) (\rightarrow K^+ \pi^-)$ | 23.96 ± 9.43 |
| Sum | 112.23 ± 11.30 |

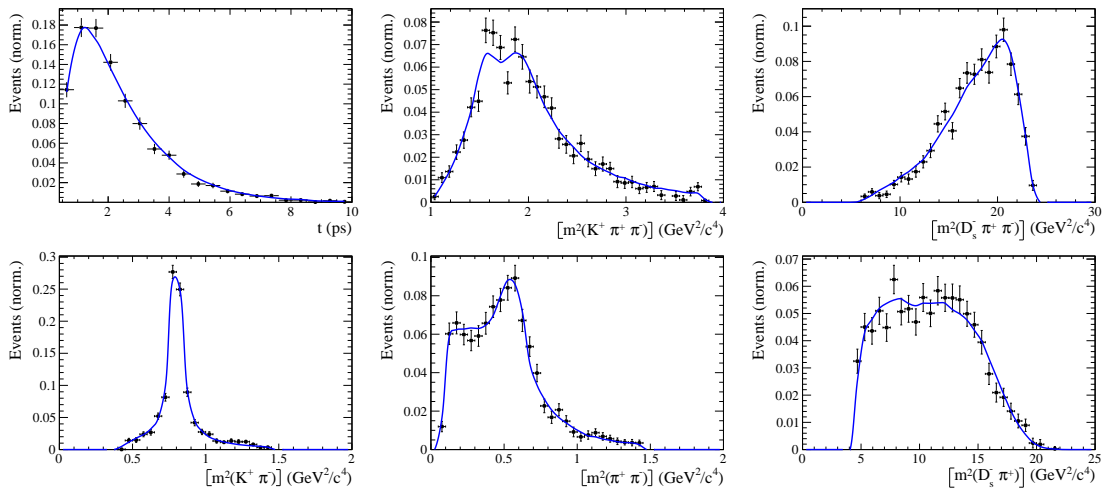


Figure 10.1

776 A Stripping and Trigger cuts

777 The following text describes variables which are used in Table 1.1 and might be ambiguous,
 778 or which benefits are not straight forward. Where noted, different cut values are applied
 779 for Run1 & Run2 data.

780 In Table 1.1, DOCA is the abbreviation for distance of closest approach. This variable
 781 is used to ensure that all D_s and $X_{s,d}$ daughters originate from the same vertex. The
 782 minimal flight distance (FD) χ^2 is a measure on how likely a particle traveled some
 783 distance before it decayed. A cut on this variable is employed to reject prompt background
 784 for D_s and $X_{s,d}$ candidates. DIRA is the abbreviation for the cosine of the angle θ between
 785 the hadron's flight direction \vec{x} and its corresponding momentum vector \vec{p} , $\cos \theta_{\vec{x}-\vec{p}}$. For
 786 signal hadrons this variable is expected to be very close to one, while it can be arbitrary
 787 distributed for background.

| Variable | Stripping Cut |
|--|--|
| Track χ^2/nDoF | < 3 |
| Track p | > 1000 MeV/c |
| Track p_T | > 100 MeV/c |
| Track IP χ^2 | > 4 |
| D_s Daughter p_T | $\sum_{i=1}^3 p_i > 1800$ MeV/c |
| D_s Daughter DOCA | < 0.5 mm |
| D_s mass m_{D_s} | ± 50 (40) MeV/ c^2 of PDG value (Run2) |
| D_s Vertex χ^2/nDoF | < 10 |
| D_s min FD χ^2 | > 36 |
| D_s FD χ^2 | > 2 to any PV |
| X_d Daughter p_T | > 2 GeV/c |
| $X_{s,d}$ Daughter DOCA | < 0.4 mm |
| $X_{s,d}$ Daughter p_T | $\sum_{i=1}^3 p_{t,i} > 1250$ MeV/c |
| $X_{s,d}$ Vertex χ^2/nDoF | < 8 |
| $X_{s,d}$ min FD χ^2/nDoF | > 16 |
| $X_{s,d}$ DIRA | > 0.98 |
| $X_{s,d}$ $\Delta\rho$ (vertex displacement perpendicular to z-axis) | > 0.1 mm |
| $X_{s,d}$ ΔZ (vertex displacement along z-axis) | > 2.0 mm |
| B_s^0 mass (only for Run2) | $5000 \text{ MeV}/c^2 < m_{B_s^0} < 6000 \text{ MeV}/c^2$ |
| B_s^0 DIRA | > 0.98 (> 0.999 for Run2) |
| B_s^0 min IP χ^2 | < 25 (< 20 for Run2) |
| B_s^0 Vertex χ^2/nDoF | < 10 (< 8 for Run2) |
| B_s^0 $\tau_{B_s^0}$ | > 0.2 ps |
| K DLL $_{K\pi}$ | > -10 |
| π DLL $_{K\pi}$ | < 10 (< 8 for Run2) |

Table 1.1: Summary of the stripping selections for $B_s^0 \rightarrow D_s K \pi \pi$ decays.

788 Table 1.2 summarizes the trigger requirements imposed by the HLT1 line used in this
 789 analysis for Run 1. At least one of the six decay particles must pass the listed requirements
 790 in order for the event to be stored for further analysis. For Run 2, this trigger line was
 791 updated and uses a multivariate classifier which takes the variables listed in Table 1.2 as

792 input, rather than directly cutting on them.

| Quantity | Hlt1TrackAllL0 requirement |
|------------------------------------|----------------------------|
| Track IP [mm] | > 0.1 |
| Track IP χ^2 | > 16 |
| Track χ^2/nDoF | < 2.5 |
| Track p_T | > 1.7 GeV/c |
| Track p | > 10 GeV/c |
| Number VELO hits/track | > 9 |
| Number missed VELO hits/track | < 3 |
| Number OT+IT \times 2 hits/track | > 16 |

Table 1.2: Summary of the cuts applied by the Hlt1TrackAllL0 trigger for Run 1. At least one of the six decay particles must pass this requirements, in order for the event to be accepted.

793 The HLt2 2, 3 and 4-body topological lines use a Boosted Decision Tree based on the
794 b-hadron p_T , its flight distance χ^2 from the nearest PV and the sum of the B_s^0 and D_s
795 vertex χ^2 divided by the sum of their number of degrees of freedom.
796 Table 1.3 summarizes the cuts applied by the inclusive ϕ trigger, which requires that a
797 $\phi \rightarrow KK$ candidate can be formed out of two tracks present in the event.

| Quantity | Hlt2IncPhi requirement |
|------------------------------------|---|
| ϕ mass | $m_\phi \pm 12$ MeV/c 2 of PDG value |
| ϕp_T | > 2.5 GeV/c |
| ϕ vertex χ^2/nDoF | < 20 |
| ϕ IP χ^2 to any PV | > 5 |

Table 1.3: Summary of the cuts applied by the Hlt2 inclusive ϕ trigger. A $\phi \rightarrow KK$ candidate, formed by two tracks in the event, must pass this requirements in order for the event to be accepted.

798 B Details of multivariate classifier

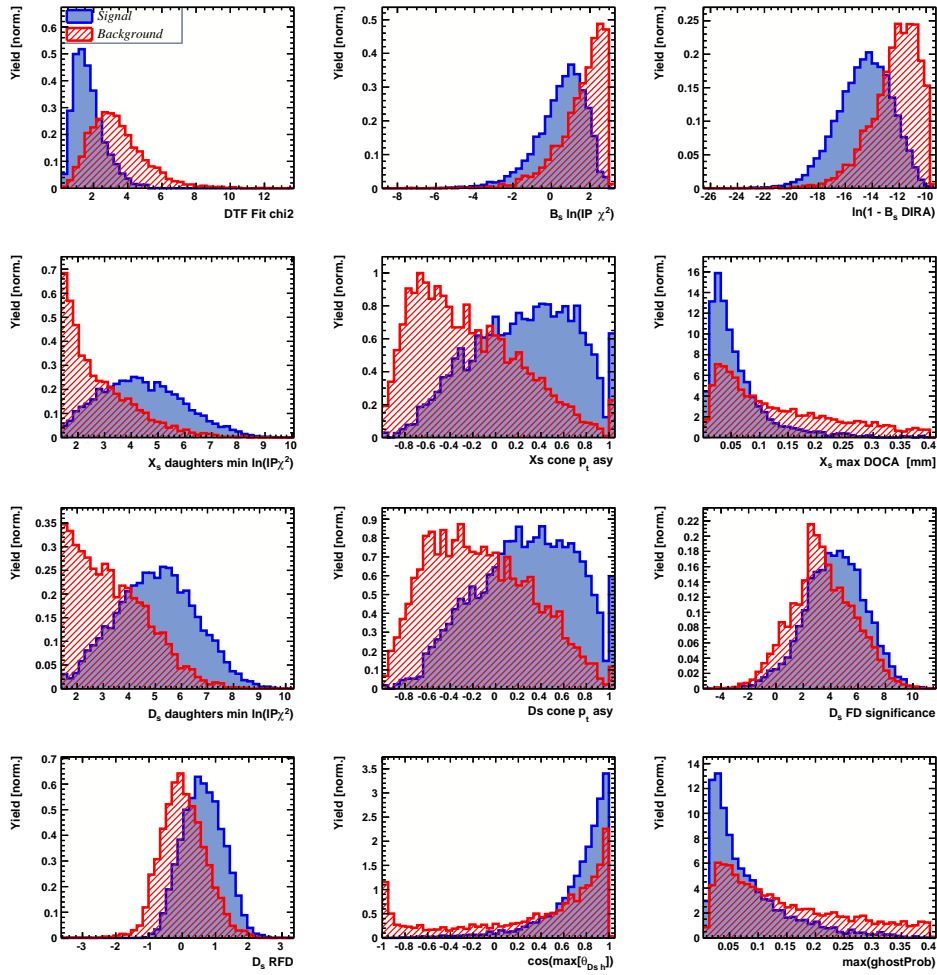


Figure A.1: Variables used to train the BDTG.

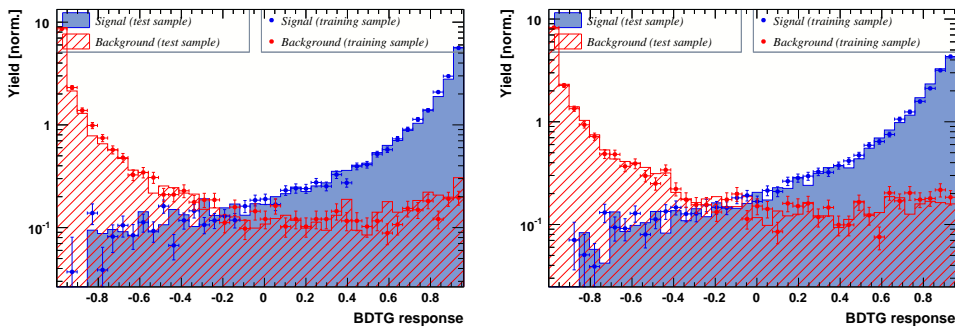


Figure A.2: Response of the classifier trained on the even (left) and odd (right) sample.

799 C Detailed mass fits

800 In this section, all fits to the mass distribution of $B_s^0 \rightarrow D_s\pi\pi\pi$ and $B_s^0 \rightarrow D_sK\pi\pi$
 801 candidates are shown. The fits are performed simultaneously in run period (Run-I, Run-
 802 II), D_s final state ($D_s \rightarrow KK\pi$ non-resonant, $D_s \rightarrow \phi\pi$, $D_s \rightarrow K^*K$, or $D_s \rightarrow \pi\pi\pi$) and
 803 L0 trigger category.

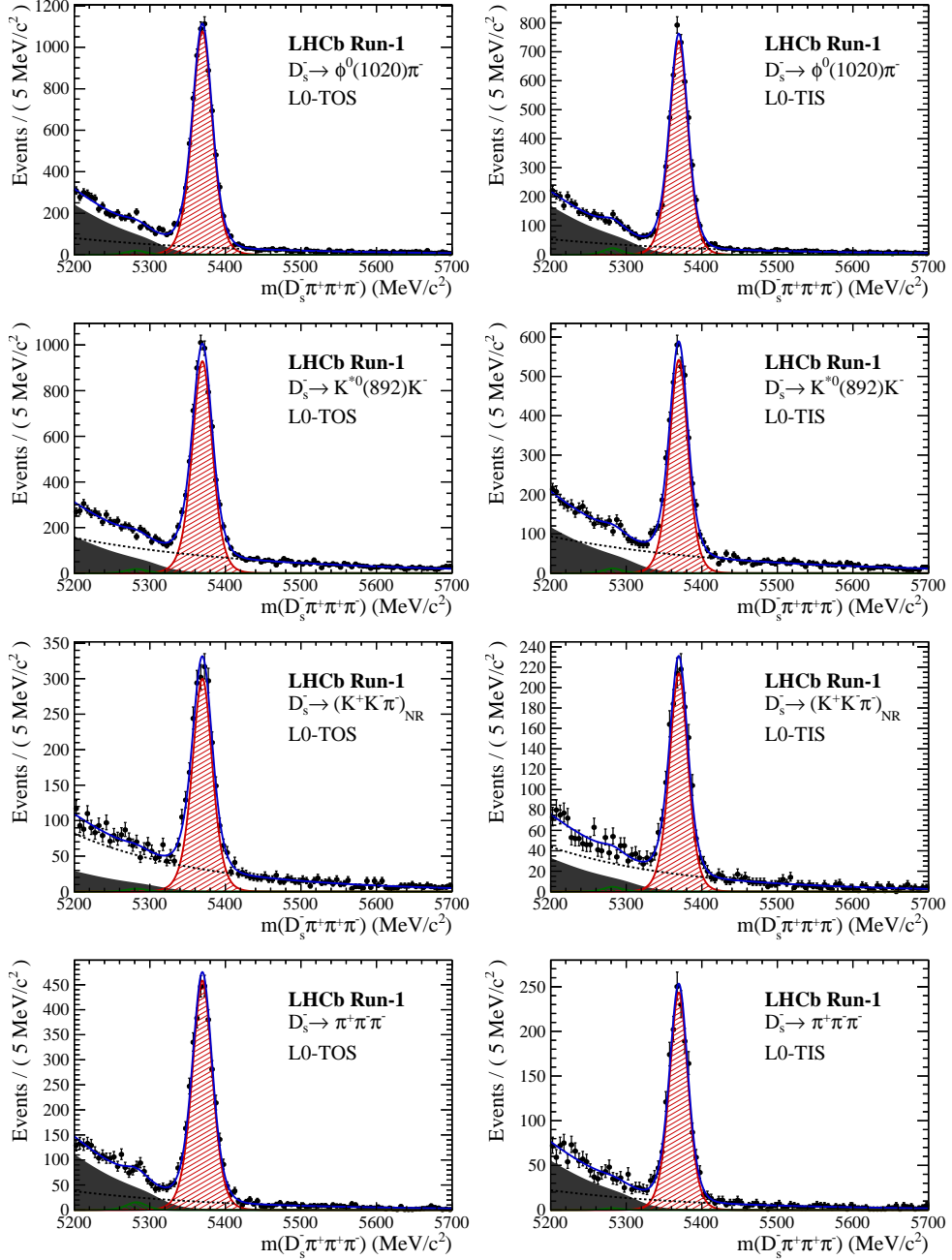


Figure B.1: Invariant mass distributions of $B_s^0 \rightarrow D_s\pi\pi\pi$ candidates for Run-I data.

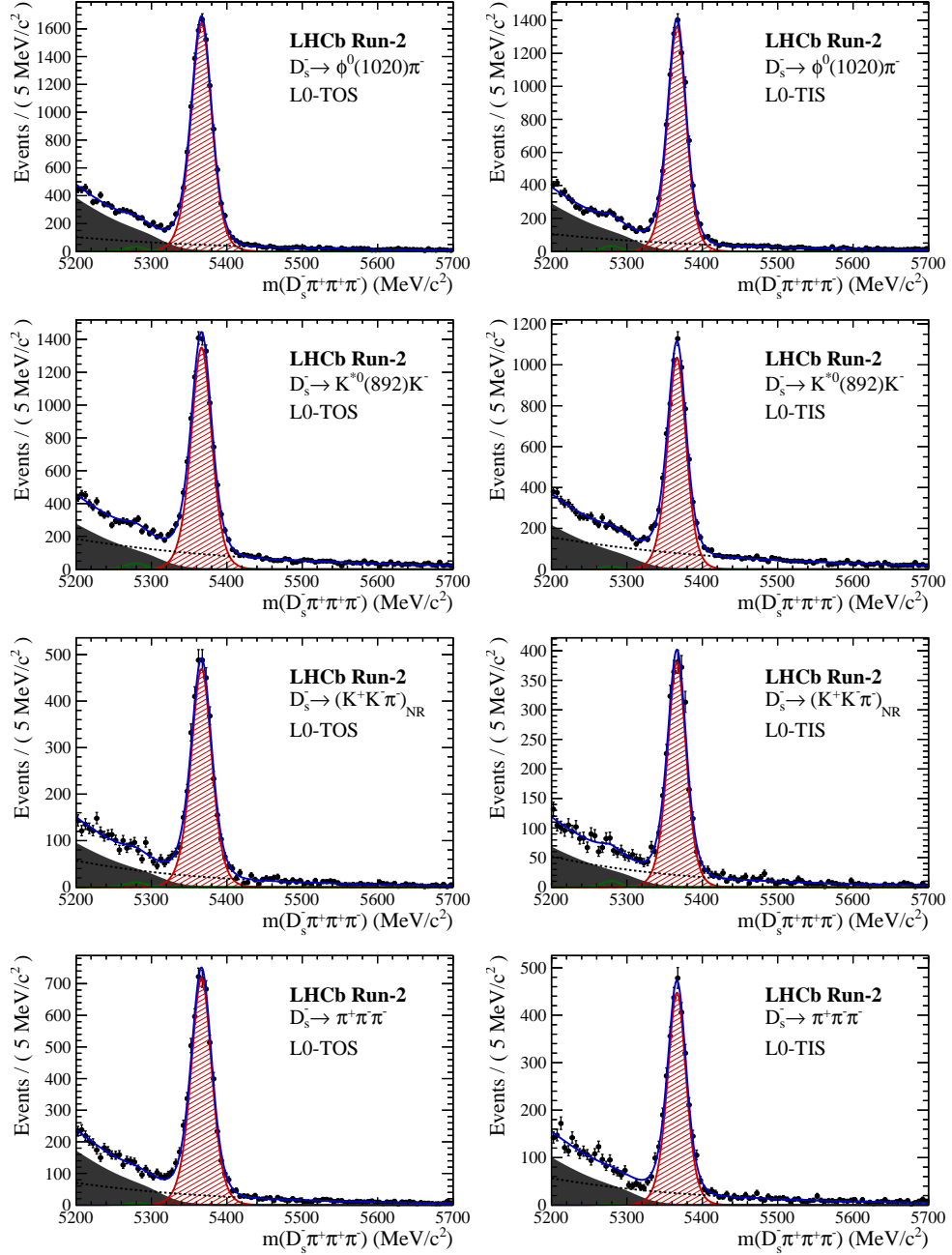


Figure B.2: Invariant mass distributions of $B_s^0 \rightarrow D_s \pi \pi \pi$ candidates for Run-II data.

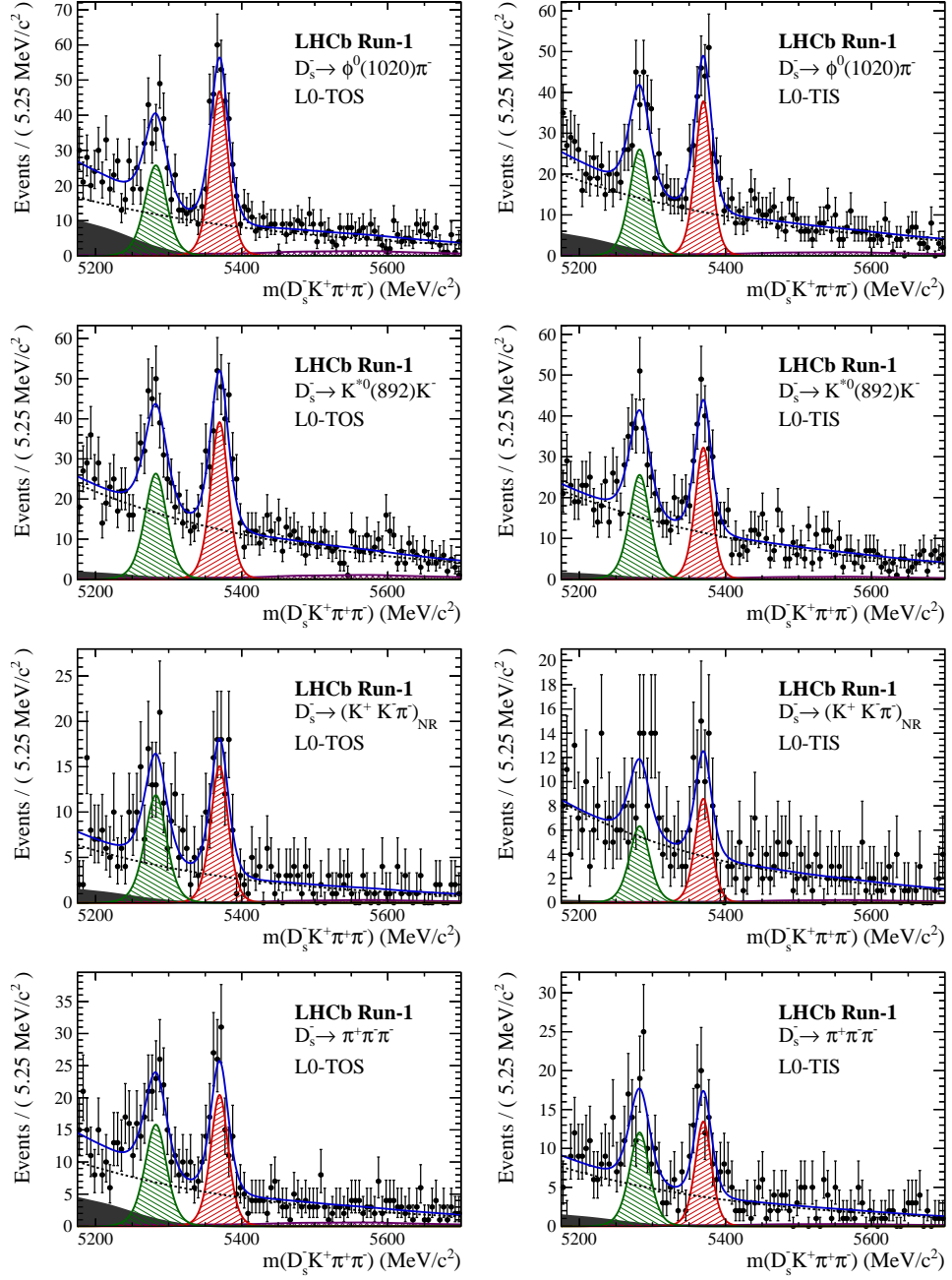


Figure B.3: Invariant mass distributions of $B_s^0 \rightarrow D_s K \pi \pi$ candidates for Run-I data.

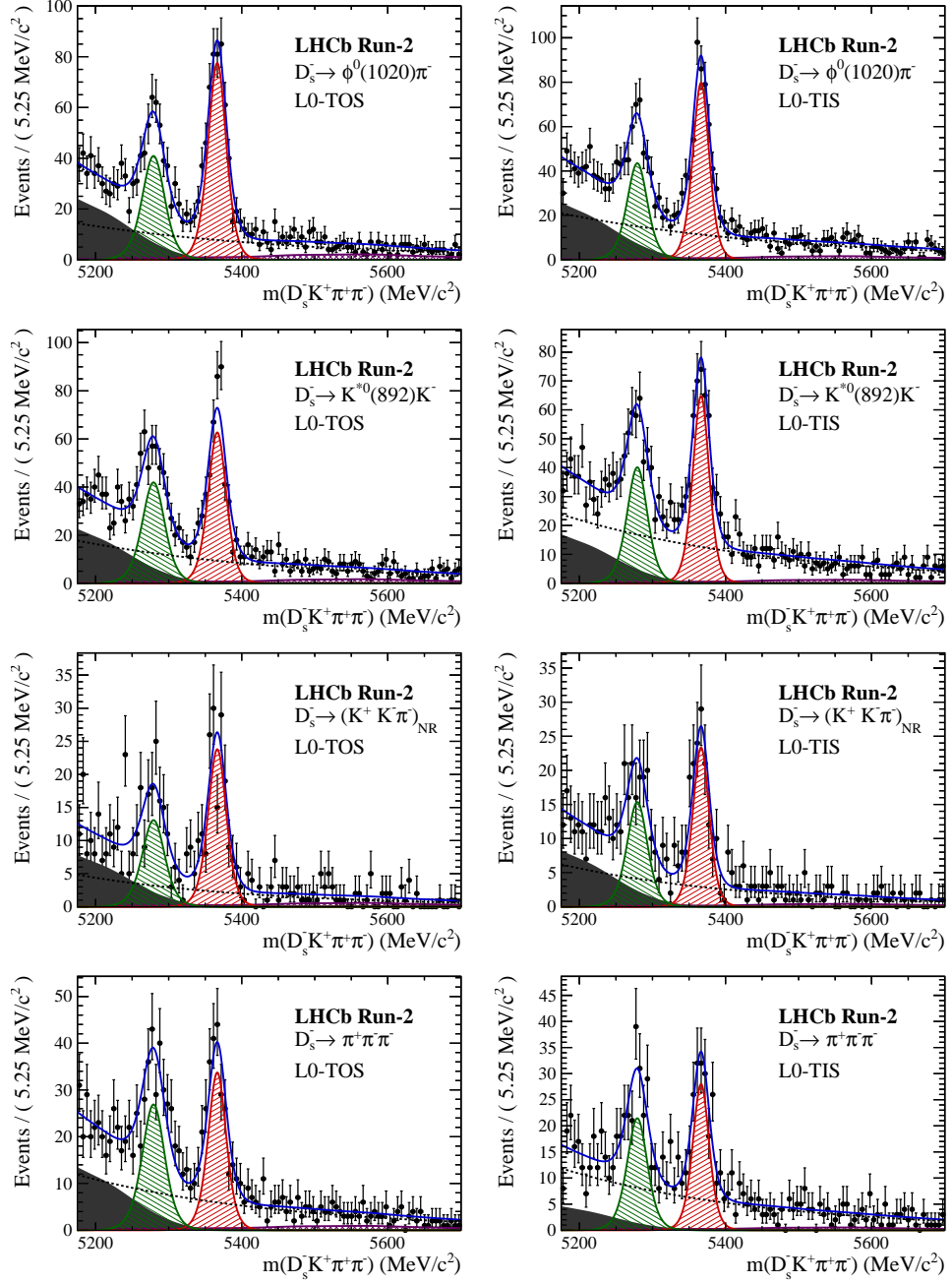


Figure B.4: Invariant mass distributions of $B_s^0 \rightarrow D_s^- K^+ \pi^+ \pi^-$ candidates for Run-II data.

804 D Decay-time Resolution fits

805 This section contains all fits to the distributions of the decay time difference Δt between
 806 the true and the reconstructed decay time of the truth-matched B_s^0 candidates on MC.
 807 The fits are performed in bins of the decay time error σ_t , where an adaptive binning
 808 scheme is used to ensure that approximately the same number of events are found in each
 809 bin.

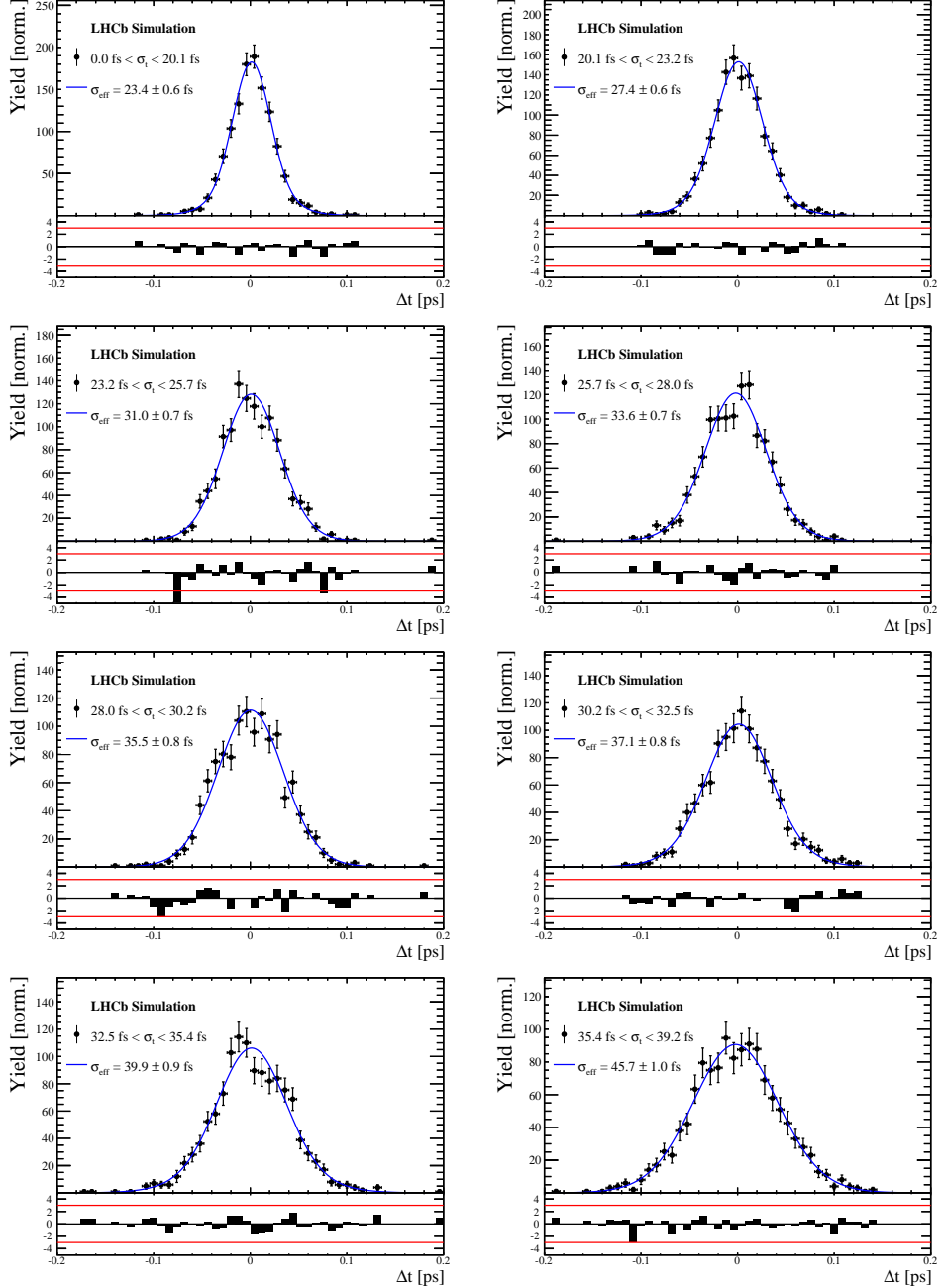


Figure C.1: Difference of the true and measured decay time of $B_s^0 \rightarrow D_s K\pi\pi$ MC candidates in bins of the per-event decay time error estimate..

| σ_t Bin [fs] | σ_1 [fs] | σ_2 [fs] | f_1 | D | σ_{eff} [fs] |
|---------------------|-----------------|-----------------|--------------|---------------------|---------------------|
| 0.0 - 20.1 | 19 ± 0.675 | 33.8 ± 1.77 | 0.75 ± 0 | 0.917 ± 0.00406 | 23.4 ± 0.599 |
| 20.1 - 23.2 | 23.4 ± 0.86 | 37.4 ± 1.95 | 0.75 ± 0 | 0.888 ± 0.00477 | 27.4 ± 0.621 |
| 23.2 - 25.7 | 28.1 ± 1.02 | 38.7 ± 2.32 | 0.75 ± 0 | 0.86 ± 0.00563 | 31 ± 0.671 |
| 25.7 - 28.0 | 30.1 ± 1.12 | 43.2 ± 2.56 | 0.75 ± 0 | 0.837 ± 0.00651 | 33.6 ± 0.734 |
| 28.0 - 30.2 | 32.4 ± 1.12 | 44.2 ± 2.59 | 0.75 ± 0 | 0.819 ± 0.00694 | 35.5 ± 0.756 |
| 30.2 - 32.5 | 32.6 ± 1.38 | 49.2 ± 3.04 | 0.75 ± 0 | 0.805 ± 0.00792 | 37.1 ± 0.841 |
| 32.5 - 35.4 | 34.4 ± 1.19 | 54.7 ± 2.85 | 0.75 ± 0 | 0.778 ± 0.0086 | 39.9 ± 0.879 |
| 35.4 - 39.2 | 41.9 ± 1.8 | 56.9 ± 4.18 | 0.75 ± 0 | 0.719 ± 0.00997 | 45.7 ± 0.962 |
| 39.2 - 44.7 | 42.2 ± 1.56 | 68.1 ± 4.01 | 0.75 ± 0 | 0.687 ± 0.0114 | 48.8 ± 1.08 |
| 44.7 - 120.0 | 55.5 ± 2.59 | 83 ± 14.7 | 0.75 ± 0 | 0.546 ± 0.0521 | 62 ± 4.89 |

Table 4.1: Measured time resolution for $B_s \rightarrow D_s K\pi\pi$ MC in bins of the per-event decay time error estimate.

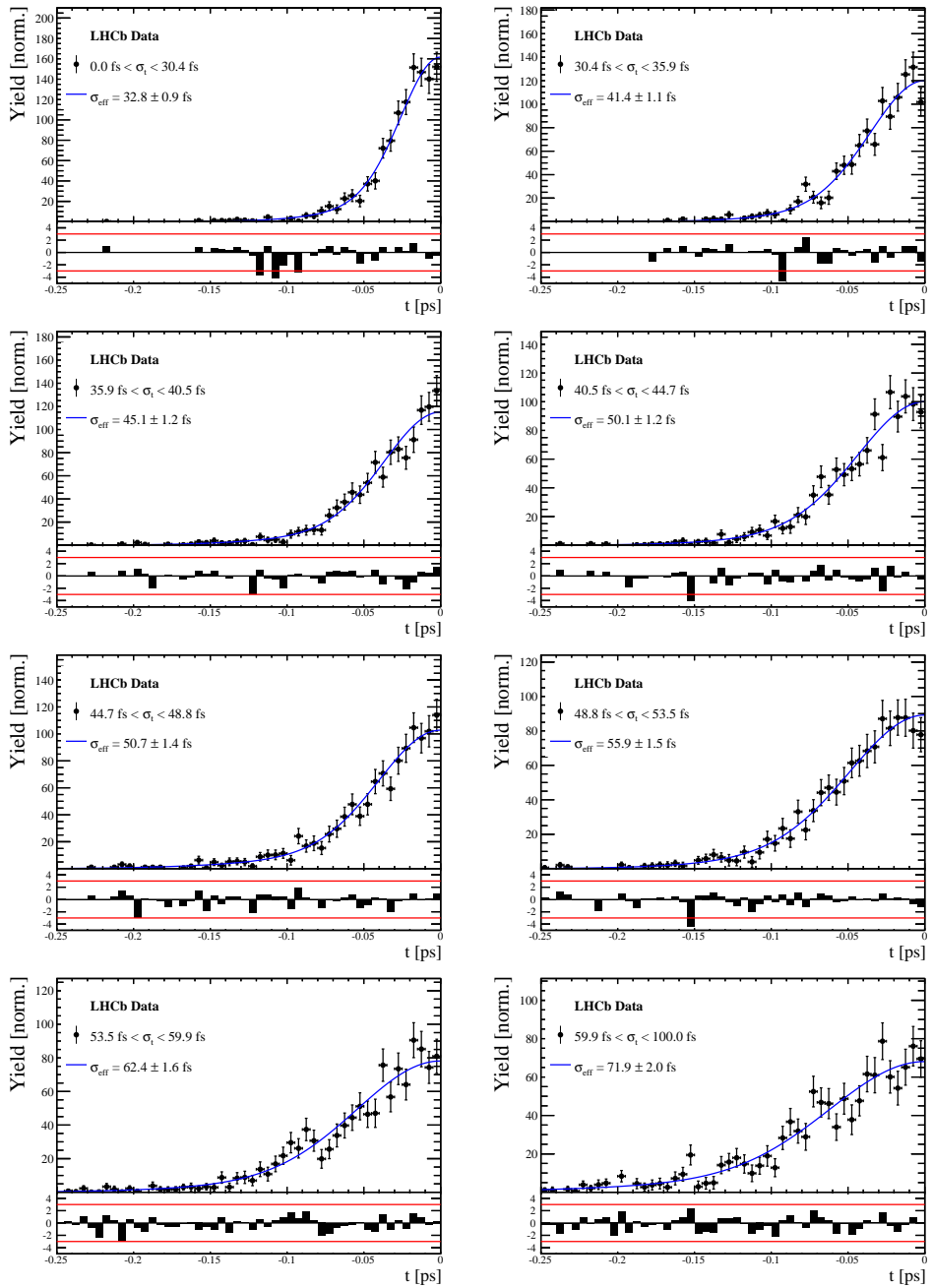


Figure C.2: Decay-time distribution for fake B_s candidates from promptly produced D_s candidates, combined with random prompt $K\pi\pi$ bachelor tracks, for bins in the per-event decay time error estimate.

| σ_t Bin [fs] | σ_1 [fs] | σ_2 [fs] | f_1 | D | σ_{eff} [fs] |
|---------------------|-----------------|-----------------|--------------|---------------------|---------------------|
| 0.0 - 30.4 | 25.4 ± 1.03 | 50.7 ± 2.77 | 0.75 ± 0 | 0.844 ± 0.00822 | 32.8 ± 0.942 |
| 30.4 - 35.9 | 34.5 ± 1.46 | 60.2 ± 3.48 | 0.75 ± 0 | 0.763 ± 0.0108 | 41.4 ± 1.08 |
| 35.9 - 40.5 | 35.6 ± 1.35 | 71.3 ± 3.84 | 0.75 ± 0 | 0.726 ± 0.0121 | 45.1 ± 1.18 |
| 40.5 - 44.7 | 42.3 ± 1.65 | 73.3 ± 4.21 | 0.75 ± 0 | 0.673 ± 0.0132 | 50.1 ± 1.24 |
| 44.7 - 48.8 | 39.6 ± 1.64 | 84.8 ± 5.07 | 0.75 ± 0 | 0.666 ± 0.0145 | 50.7 ± 1.36 |
| 48.8 - 53.5 | 47.6 ± 1.94 | 82.4 ± 5.48 | 0.75 ± 0 | 0.611 ± 0.0157 | 55.9 ± 1.46 |
| 53.5 - 59.9 | 53 ± 2.15 | 95.3 ± 6.84 | 0.75 ± 0 | 0.541 ± 0.0174 | 62.4 ± 1.63 |
| 59.9 - 100.0 | 60.5 ± 2.8 | 125 ± 14 | 0.75 ± 0 | 0.443 ± 0.0204 | 71.9 ± 2.03 |

Table 4.2: Measured time resolution for prompt- D_s data in bins of the per-event decay time error estimate.

E Spin Amplitudes

The spin factors used for $B \rightarrow P_1 P_2 P_3 P_4$ decays are given in Table 5.1.

Table 5.1: Spin factors for all topologies considered in this analysis. In the decay chains, S , P , V , A , T and PT stand for scalar, pseudoscalar, vector, axial vector, tensor and pseudotensor, respectively. If no angular momentum is specified, the lowest angular momentum state compatible with angular momentum conservation and, where appropriate, parity conservation, is used.

| Number | Decay chain | Spin amplitude |
|--------|--|--|
| 1 | $B \rightarrow (P P_1)$, $P \rightarrow (S P_2)$, $S \rightarrow (P_3 P_4)$ | 1 |
| 2 | $B \rightarrow (P P_1)$, $P \rightarrow (V P_2)$, $V \rightarrow (P_3 P_4)$ | $L_{(1)\alpha}(P) L_{(1)}^\alpha(V)$ |
| 3 | $B \rightarrow (A P_1)$, $A \rightarrow (V P_2)$, $V \rightarrow (P_3 P_4)$ | $L_{(1)\alpha}(B) P_{(1)}^{\alpha\beta}(A) L_{(1)\beta}(V)$ |
| 4 | $B \rightarrow (A P_1)$, $A[D] \rightarrow (P_2 V)$, $V \rightarrow (P_3 P_4)$ | $L_{(1)\alpha}(B) L_{(2)}^{\alpha\beta}(A) L_{(1)\beta}(V)$ |
| 5 | $B \rightarrow (A P_1)$, $A \rightarrow (S P_2)$, $S \rightarrow (P_3 P_4)$ | $L_{(1)\alpha}(B) L_{(1)}^\alpha(A)$ |
| 6 | $B \rightarrow (A P_1)$, $A \rightarrow (T P_2)$, $T \rightarrow (P_3 P_4)$ | $L_{(1)\alpha}(B) L_{(1)\beta}(A) L_{(2)}^{\alpha\beta}(T)$ |
| 7 | $B \rightarrow (V_1 P_1)$, $V_1 \rightarrow (V_2 P_2)$, $V_2 \rightarrow (P_3 P_4)$ | $L_{(1)\mu}(B) P_{(1)}^{\mu\alpha}(V_1) \epsilon_{\alpha\beta\gamma\delta} L_{(1)}^\beta(V_1) p_{V_1}^\gamma L_{(1)}^\delta(V_2)$ |
| 8 | $B \rightarrow (PT P_1)$, $PT \rightarrow (V P_2)$, $V \rightarrow (P_3 P_4)$ | $L_{(2)\alpha\beta}(B) P_{(2)}^{\alpha\beta\gamma\delta}(PT) L_{(1)\gamma}(PT) L_{(1)\delta}(V)$ |
| 9 | $B \rightarrow (PT P_1)$, $PT \rightarrow (S P_2)$, $S \rightarrow (P_3 P_4)$ | $L_{(2)\alpha\beta}(B) L_{(2)}(PT)^{\alpha\beta}$ |
| 10 | $B \rightarrow (PT P_1)$, $PT \rightarrow (T P_2)$, $T \rightarrow (P_3 P_4)$ | $L_{(2)\alpha\beta}(B) P_{(2)}^{\alpha\beta\gamma\delta}(PT) L_{(2)\gamma\delta}(T)$ |
| 11 | $B \rightarrow (T P_1)$, $T \rightarrow (V P_2)$, $V \rightarrow (P_3 P_4)$ | $L_{(2)\mu\nu}(B) P_{(2)}^{\mu\nu\rho\alpha}(T) \epsilon_{\alpha\beta\gamma\delta} L_{(2)\rho}^\beta(T) p_T^\gamma P_{(1)}^{\delta\sigma}(T) L_{(1)\sigma}(V)$ |
| 12 | $B \rightarrow (T_1 P_1)$, $T_1 \rightarrow (T_2 P_2)$, $T_2 \rightarrow (P_3 P_4)$ | $L_{(2)\mu\nu}(B) P_{(2)}^{\mu\nu\rho\alpha}(T_1) \epsilon_{\alpha\beta\gamma\delta} L_{(1)}^\beta(T_1) p_{T_1}^\gamma L_{(2)\rho}^\delta(T_2)$ |
| 13 | $B \rightarrow (S_1 S_2)$, $S_1 \rightarrow (P_1 P_2)$, $S_2 \rightarrow (P_3 P_4)$ | 1 |
| 14 | $B \rightarrow (V S)$, $V \rightarrow (P_1 P_2)$, $S \rightarrow (P_3 P_4)$ | $L_{(1)\alpha}(B) L_{(1)}^\alpha(V)$ |
| 15 | $B \rightarrow (V_1 V_2)$, $V_1 \rightarrow (P_1 P_2)$, $V_2 \rightarrow (P_3 P_4)$ | $L_{(1)\alpha}(V_1) L_{(1)}^\alpha(V_2)$ |
| 16 | $B[P] \rightarrow (V_1 V_2)$, $V_1 \rightarrow (P_1 P_2)$, $V_2 \rightarrow (P_3 P_4)$ | $\epsilon_{\alpha\beta\gamma\delta} L_{(1)}^\alpha(B) L_{(1)}^\beta(V_1) L_{(1)}^\gamma(V_2) p_B^\delta$ |
| 17 | $B[D] \rightarrow (V_1 V_2)$, $V_1 \rightarrow (P_1 P_2)$, $V_2 \rightarrow (P_3 P_4)$ | $L_{(2)\alpha\beta}(B) L_{(1)}^\alpha(V_1) L_{(1)}^\beta(V_2)$ |
| 18 | $B \rightarrow (T S)$, $T \rightarrow (P_1 P_2)$, $S \rightarrow (P_3 P_4)$ | $L_{(2)\alpha\beta}(B) L_{(2)}^{\alpha\beta}(T)$ |
| 19 | $B \rightarrow (V T)$, $T \rightarrow (P_1 P_2)$, $V \rightarrow (P_3 P_4)$ | $L_{(1)\alpha}(B) L_{(2)}^{\alpha\beta}(T) L_{(1)\beta}(V)$ |
| 20 | $B[D] \rightarrow (TV)$, $T \rightarrow (P_1 P_2)$, $V \rightarrow (P_3 P_4)$ | $\epsilon_{\alpha\beta\delta\gamma} L_2^{\alpha\mu}(B) L_{2\mu}^\beta L_{(1)}^\gamma(V) p_B^\delta$ |
| 21 | $B \rightarrow (T_1 T_2)$, $T_1 \rightarrow (P_1 P_2)$, $T_2 \rightarrow (P_3 P_4)$ | $L_{(2)\alpha\beta}(T_1) L_{(2)}^{\alpha\beta}(T_2)$ |
| 22 | $B[P] \rightarrow (T_1 T_2)$, $T_1 \rightarrow (P_1 P_2)$, $T_2 \rightarrow (P_3 P_4)$ | $\epsilon_{\alpha\beta\gamma\delta} L_{(1)}^\alpha(B) L_{(2)}^{\beta\mu}(T_1) L_{(2)\mu}^\gamma(T_2) p_B^\delta$ |
| 23 | $B[D] \rightarrow (T_1 T_2)$, $T_1 \rightarrow (P_1 P_2)$, $T_2 \rightarrow (P_3 P_4)$ | $L_{(2)\alpha\beta}(B) L_{(2)}^{\alpha\gamma}(T_1) L_{(2)\gamma}^\beta(T_2)$ |

F Considered Decay Chains

The various decay channels considered in the model building are listed in Table 6.1.

Table 6.1: Decays considered in the LASSO model building.

| Decay channel |
|---|
| $B_s \rightarrow D_s^- [K_1(1270)^+ [S, D] \rightarrow \pi^+ K^*(892)^0]$ |
| $B_s \rightarrow D_s^- [K_1(1270)^+ \rightarrow \pi^+ K^*(1430)^0]$ |
| $B_s \rightarrow D_s^- [K_1(1270)^+ [S, D] \rightarrow K^+ \rho(770)^0]$ |
| $B_s \rightarrow D_s^- [K_1(1270)^+ [S, D] \rightarrow K^+ \omega(782)]$ |
| $B_s \rightarrow D_s^- [K_1(1400)^+ [S, D] \rightarrow \pi^+ K^*(892)^0]$ |
| $B_s \rightarrow D_s^- [K_1(1400)^+ [S, D] \rightarrow K^+ \rho(770)^0]$ |
| $B_s \rightarrow D_s^- [K(1460)^+ \rightarrow \pi^+ \kappa]$ |
| $B_s \rightarrow D_s^- [K(1460)^+ \rightarrow K^+ \sigma]$ |
| $B_s \rightarrow D_s^- [K(1460)^+ \rightarrow \pi^+ K^*(892)^0]$ |
| $B_s \rightarrow D_s^- [K(1460)^+ \rightarrow K^+ \rho(770)^0]$ |
| $B_s \rightarrow D_s^- [K^*(1410)^+ \rightarrow \pi^+ K^*(892)^0]$ |
| $B_s \rightarrow D_s^- [K^*(1410)^+ \rightarrow K^+ \rho(770)^0]$ |
| $B_s \rightarrow D_s^- [K_2^*(1430)^+ \rightarrow \pi^+ K^*(892)^0]$ |
| $B_s \rightarrow D_s^- [K_2^*(1430)^+ \rightarrow K^+ \rho(770)^0]$ |
| $B_s \rightarrow D_s^- [K^*(1680)^+ \rightarrow \pi^+ K^*(892)^0]$ |
| $B_s \rightarrow D_s^- [K^*(1680)^+ \rightarrow K^+ \rho(770)^0]$ |
| $B_s \rightarrow D_s^- [K_2(1770)^+ \rightarrow \pi^+ K^*(892)^0]$ |
| $B_s \rightarrow D_s^- [K_2(1770)^+ \rightarrow K^+ \rho(770)^0]$ |
| $B_s \rightarrow \sigma^0 (D_s^- K^+)_S$ |
| $B_s [S, P, D] \rightarrow \sigma^0 (D_s^- K^+)_V$ |
| $B_s \rightarrow \rho(770)^0 (D_s^- K^+)_S$ |
| $B_s [S, P, D] \rightarrow \rho(770)^0 (D_s^- K^+)_V$ |
| $B_s \rightarrow K^*(892)^0 (D_s^- \pi^+)_S$ |
| $B_s [S, P, D] \rightarrow K^*(892)^0 (D_s^- \pi^+)_V$ |
| $B_s \rightarrow (D_s^- K^+)_S (\pi^+ \pi^-)_S$ |

814 G MC corrections

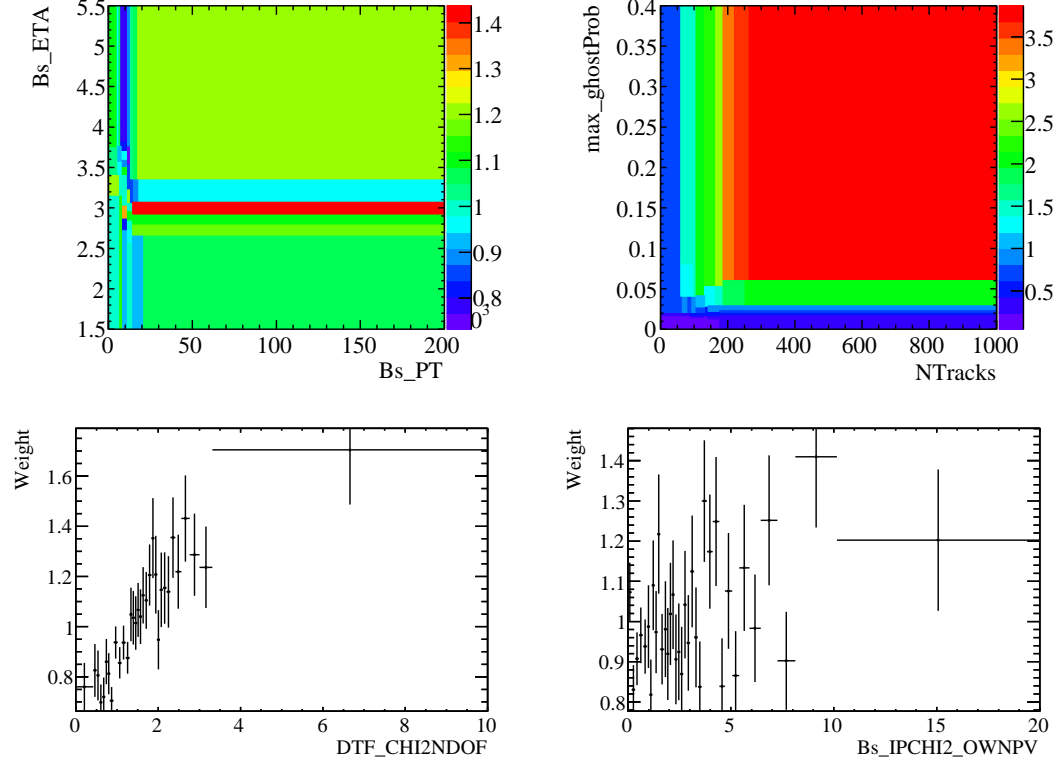


Figure C.1: Weights applied to correct for Data/MC differences.

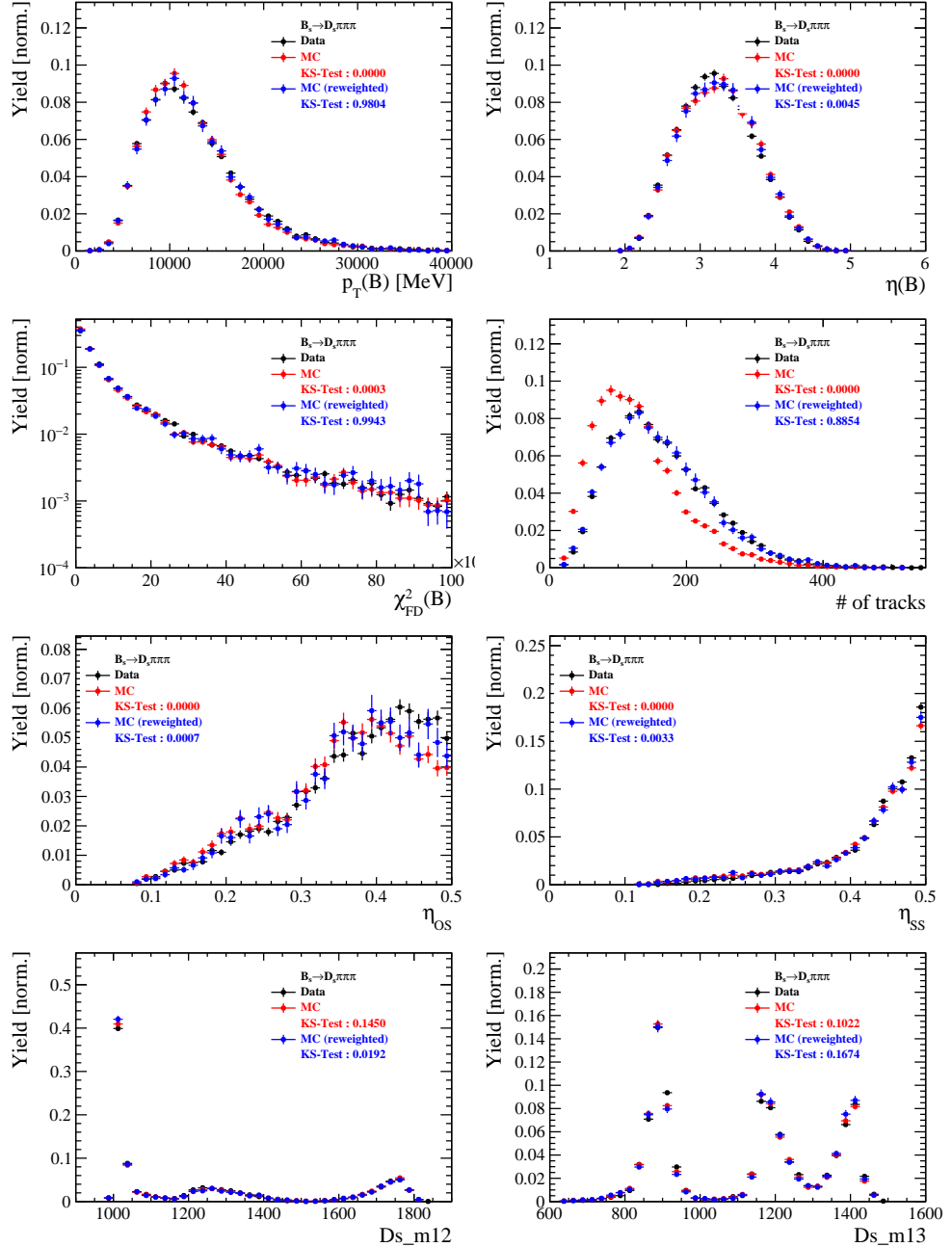


Figure C.2: Comparison of selected variables for $B_s \rightarrow D_s \pi\pi\pi$ decays.

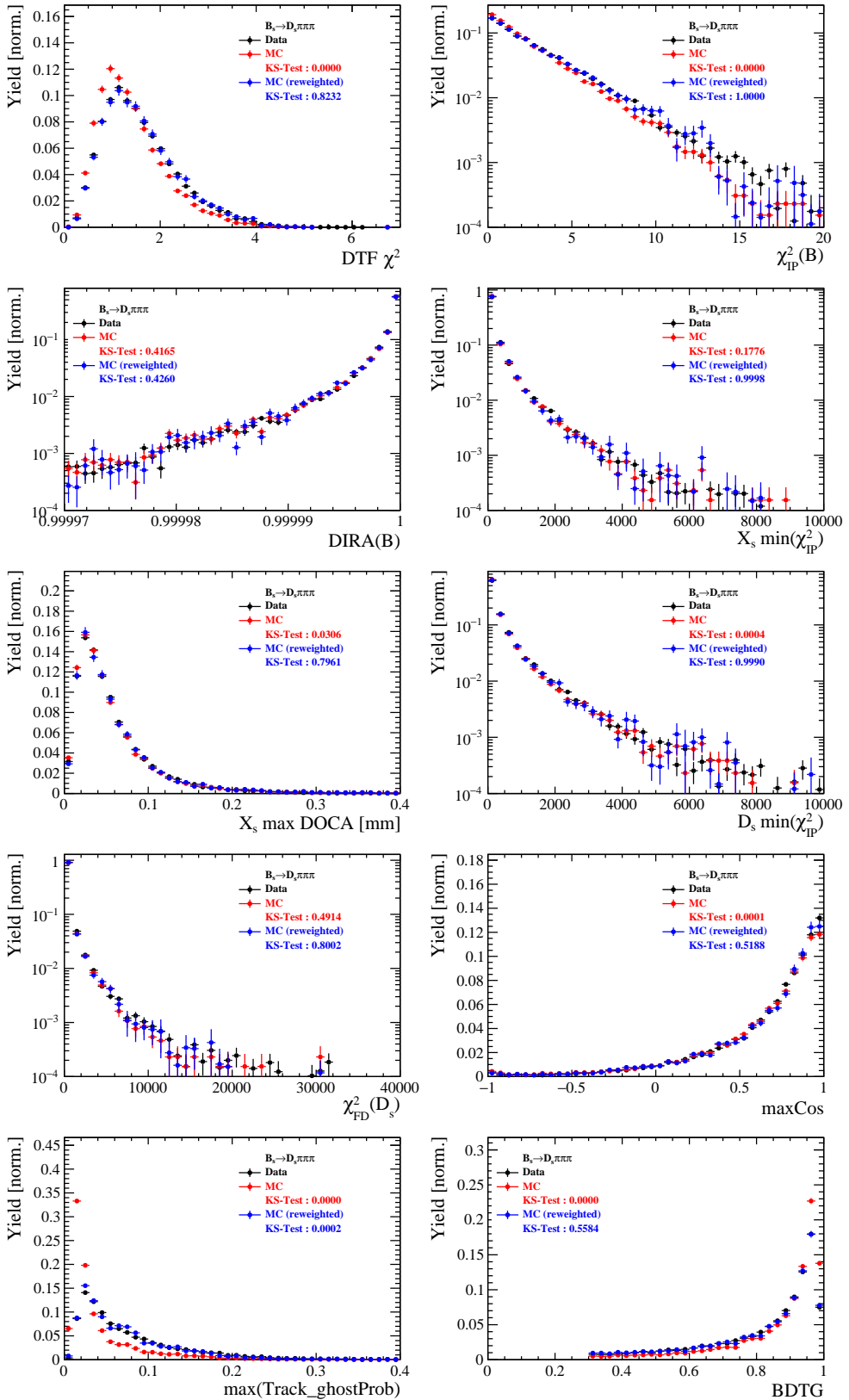


Figure C.3: Comparison of BDTG input variables and classifier response for $B_s \rightarrow D_s \pi\pi\pi$ decays.

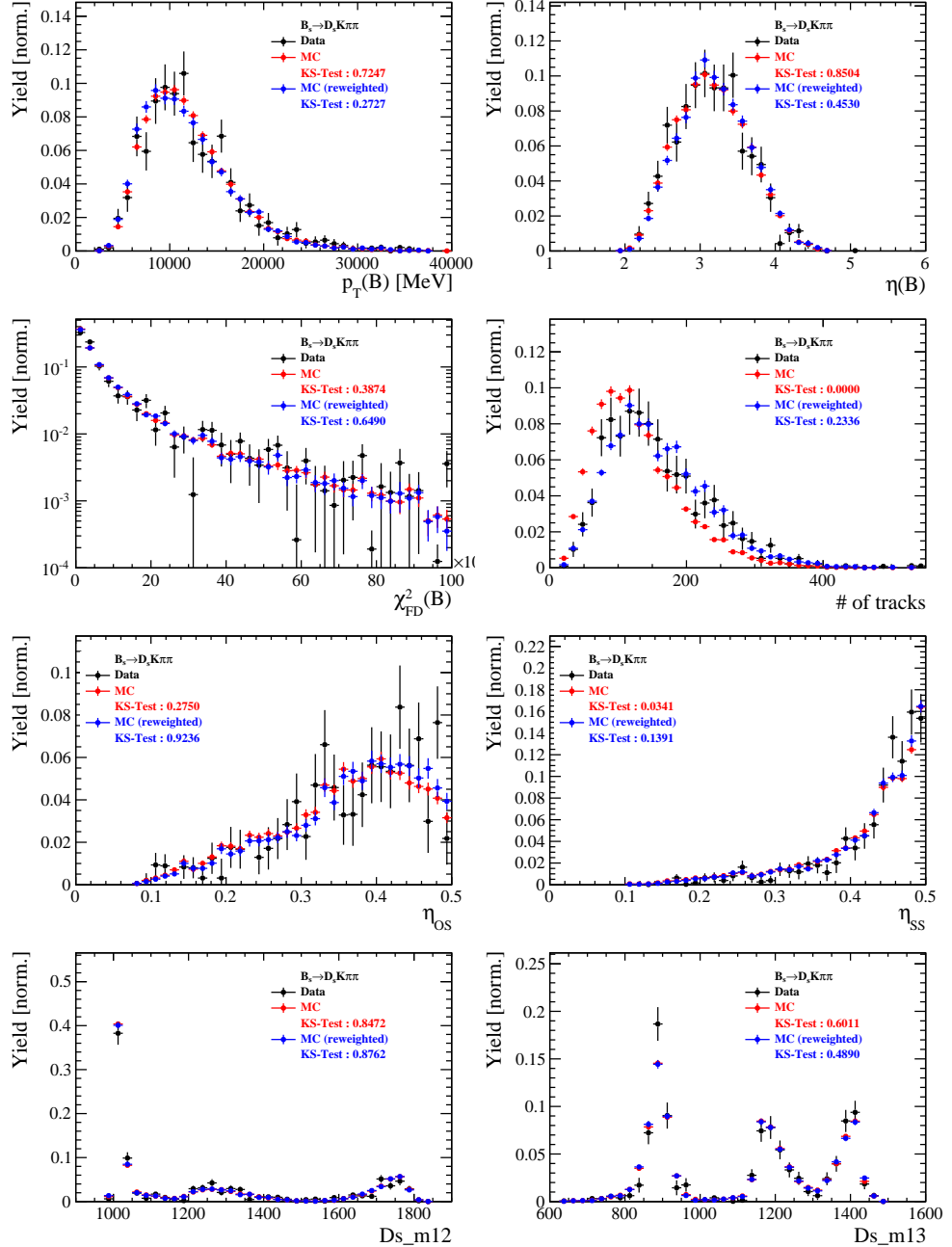


Figure C.4: Comparison of selected variables for $B_s \rightarrow D_s K\pi\pi$ decays.

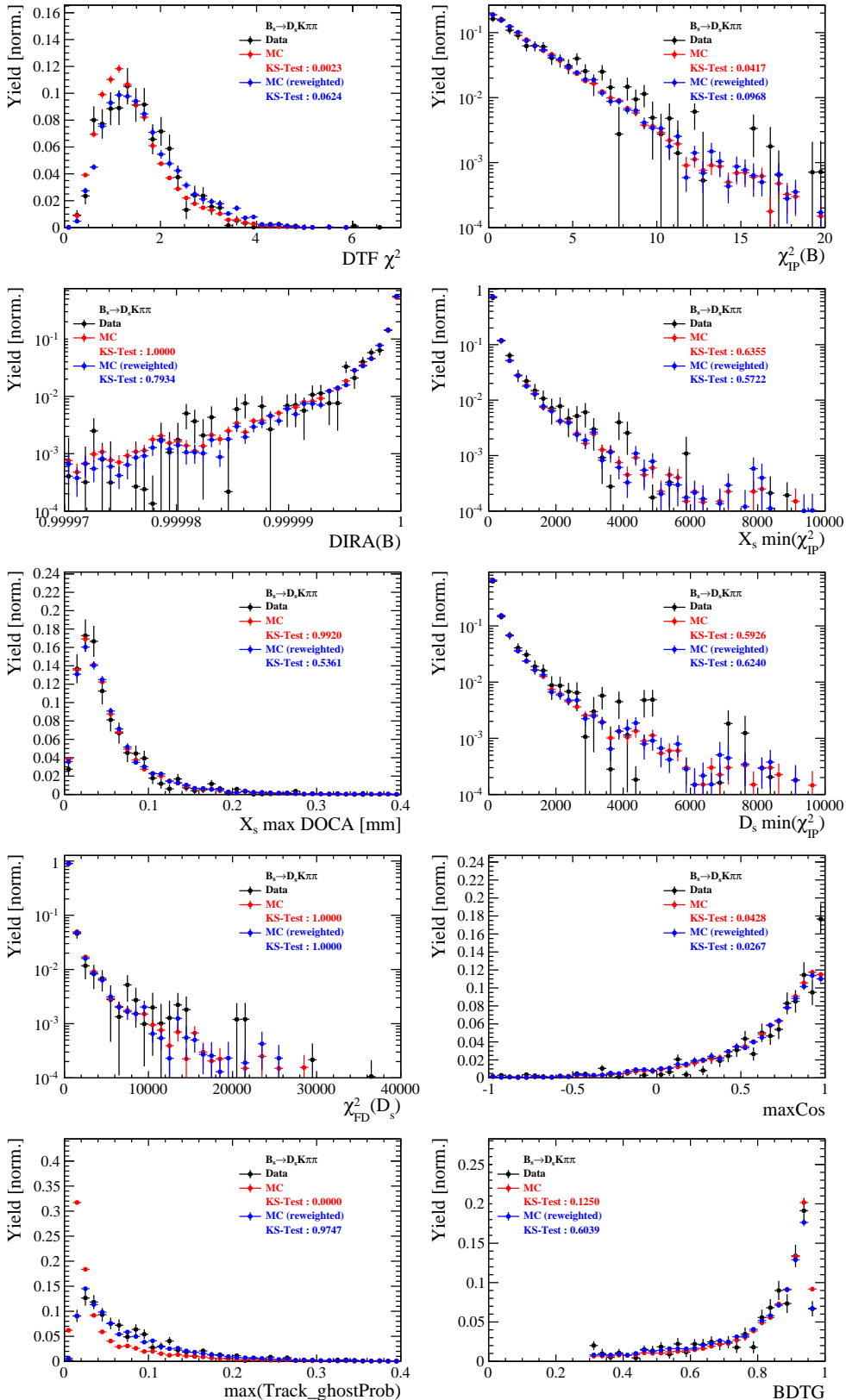


Figure C.5: Comparison of BDTG input variables and classifier response for $B_s \rightarrow D_s K\pi\pi$ decays.

815 H Data distributions

816 H.1 Comparison of signal and calibration channel

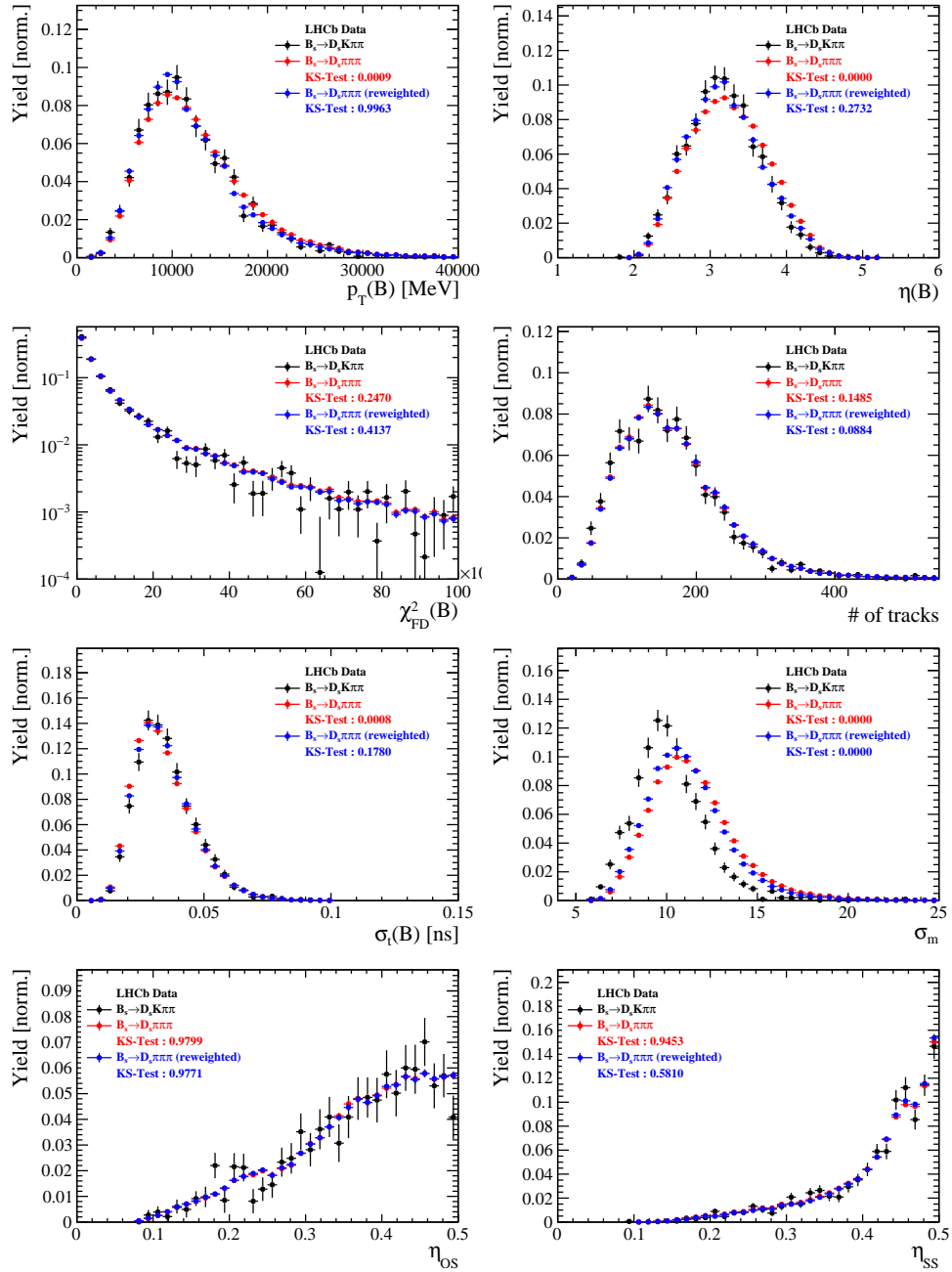


Figure C.1: Comparison of selected variables.

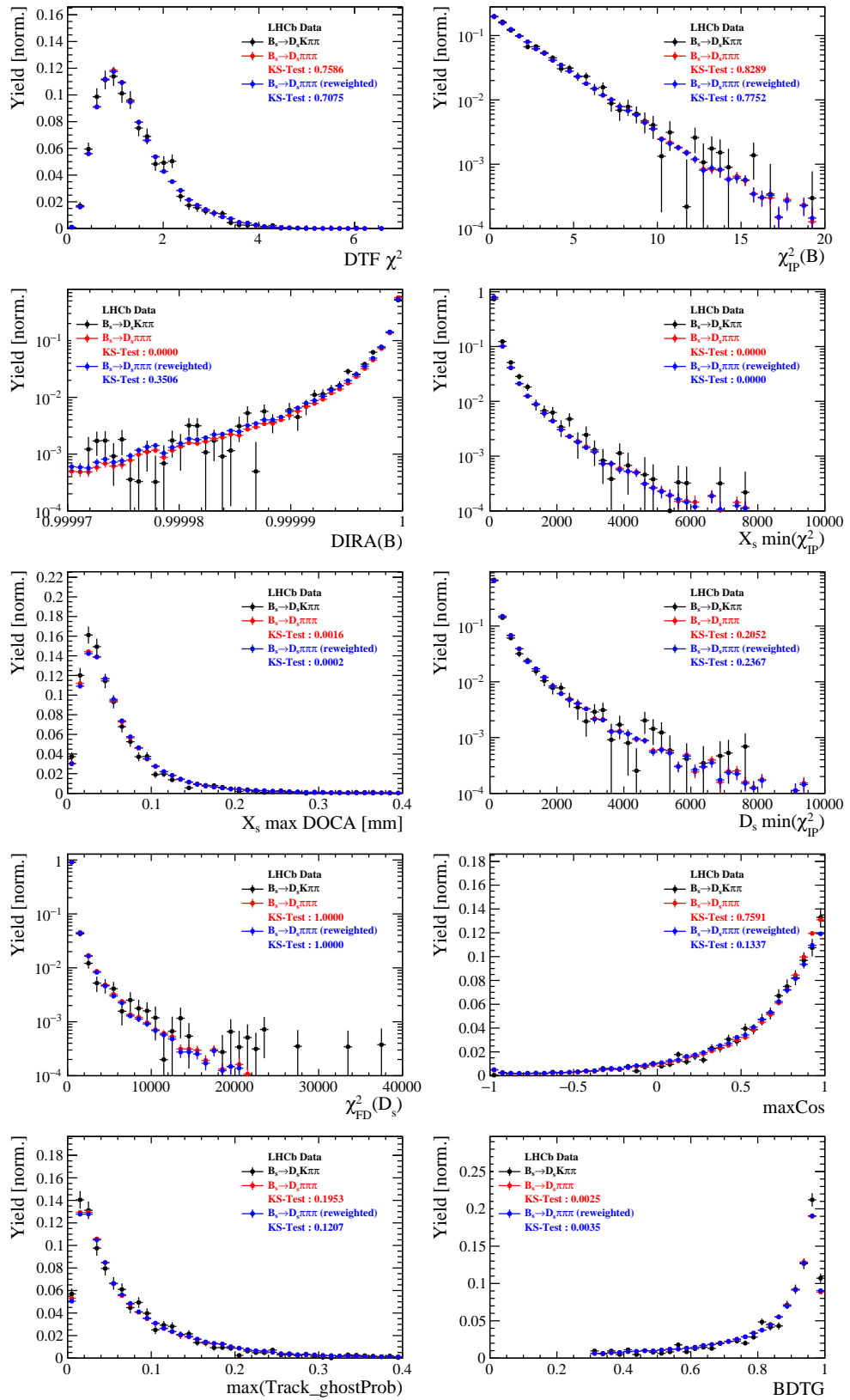


Figure C.2: Comparison of BDTG input variables and classifier response.

817 H.2 Comparison of Run-I and Run-II data

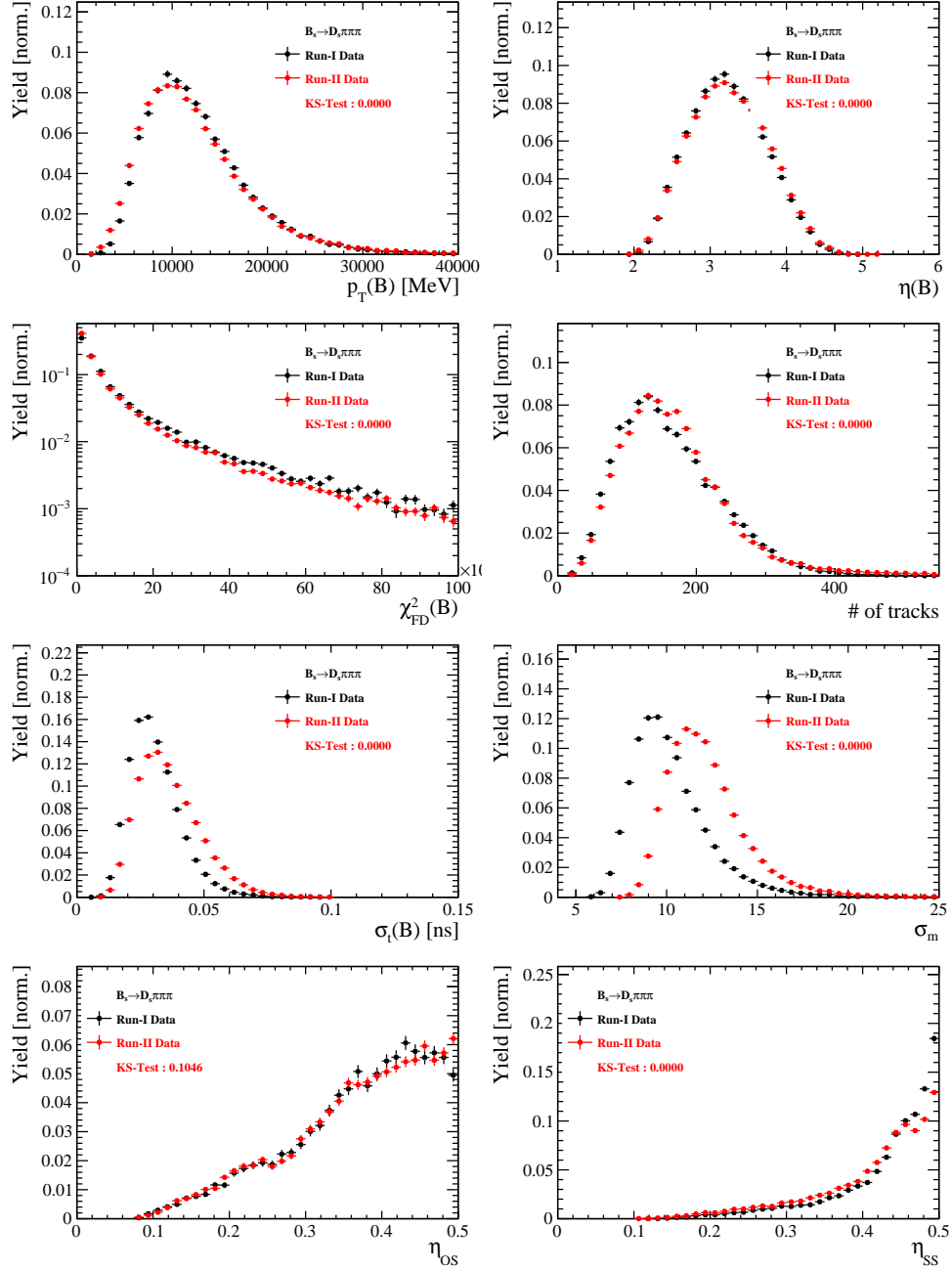


Figure C.3: Comparison of selected variables.

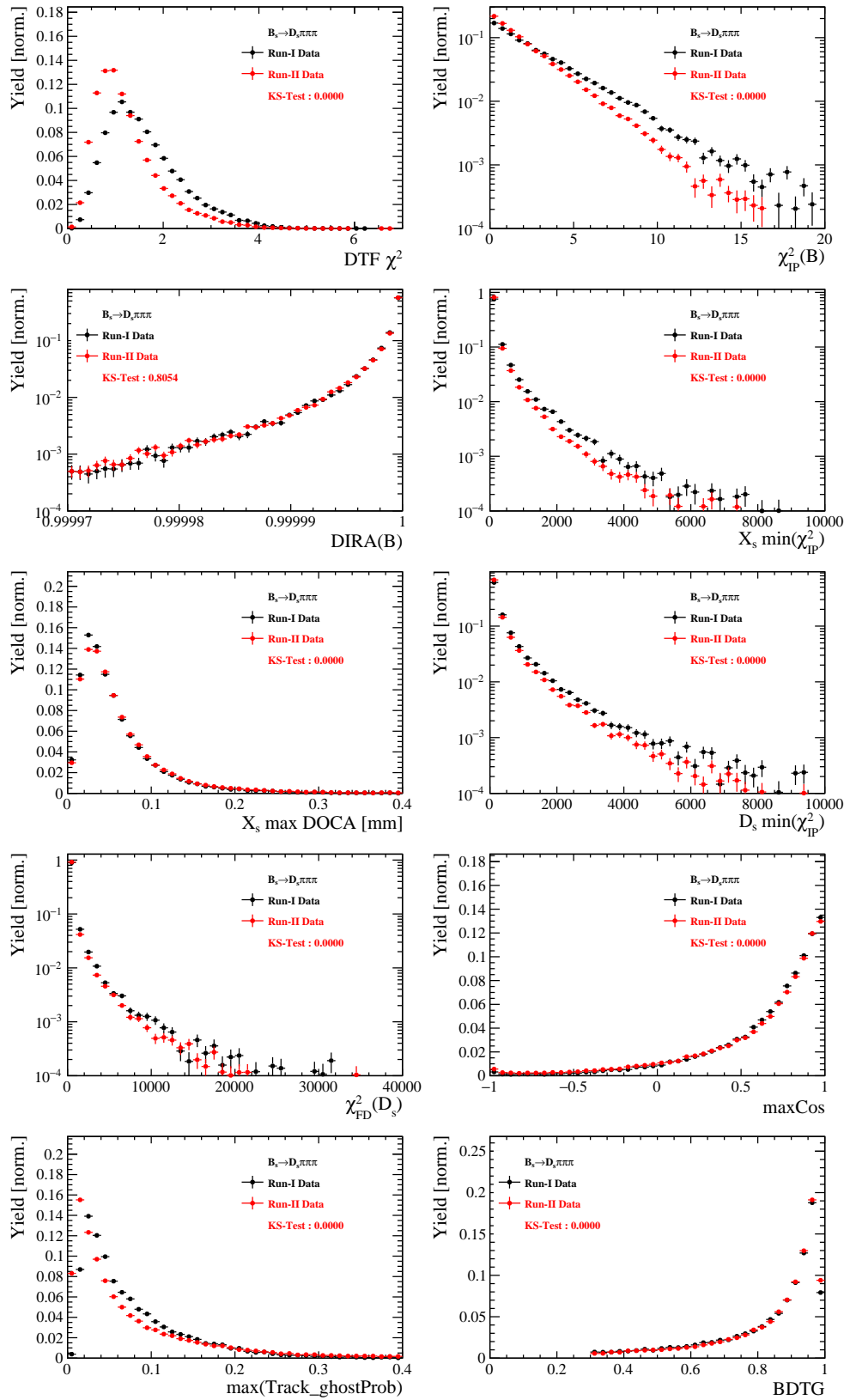


Figure C.4: Comparison of BDTG input variables and classifier response.

818 H.3 Comparison of D_s final states

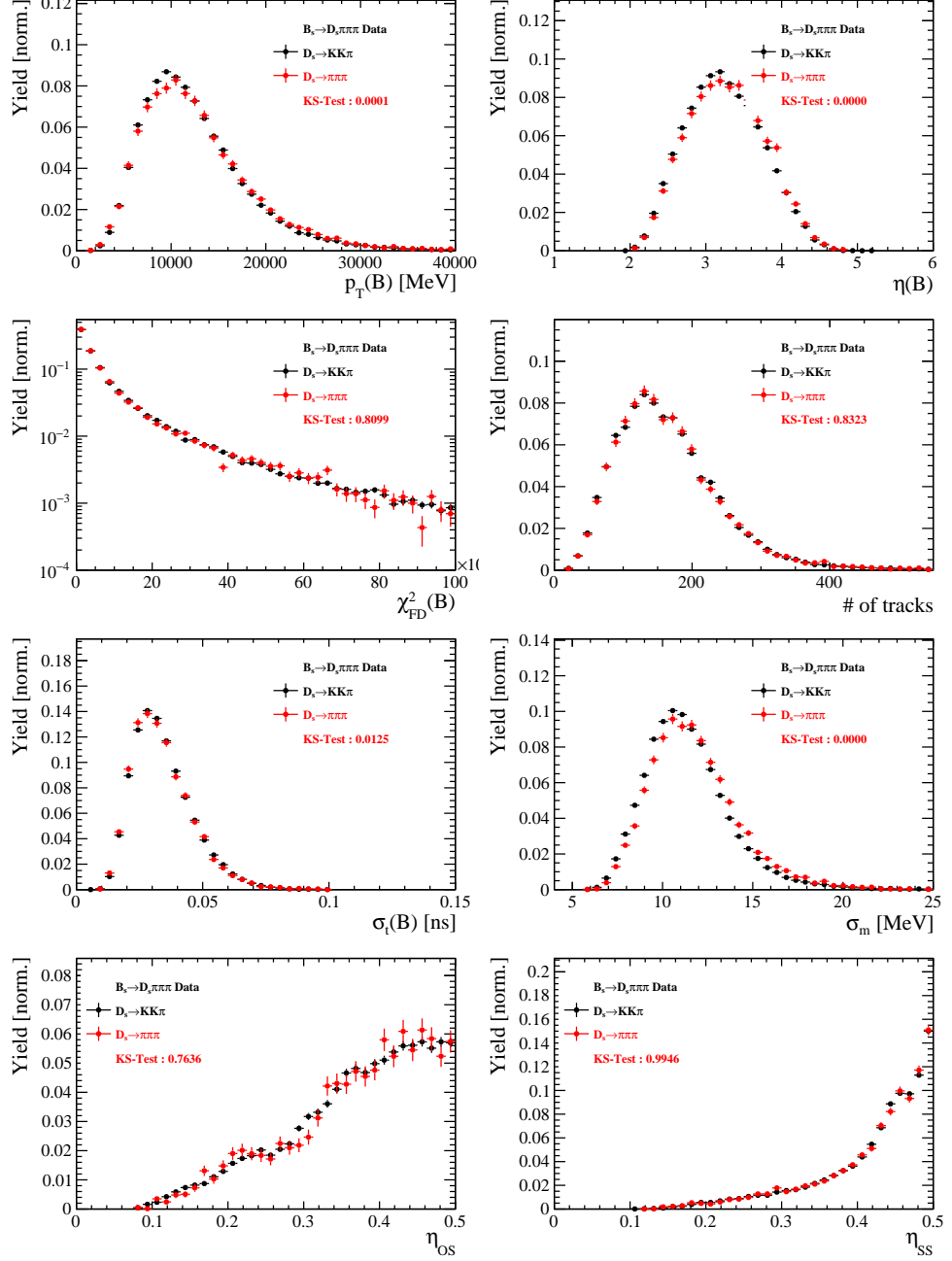


Figure C.5: Comparison of selected variables.

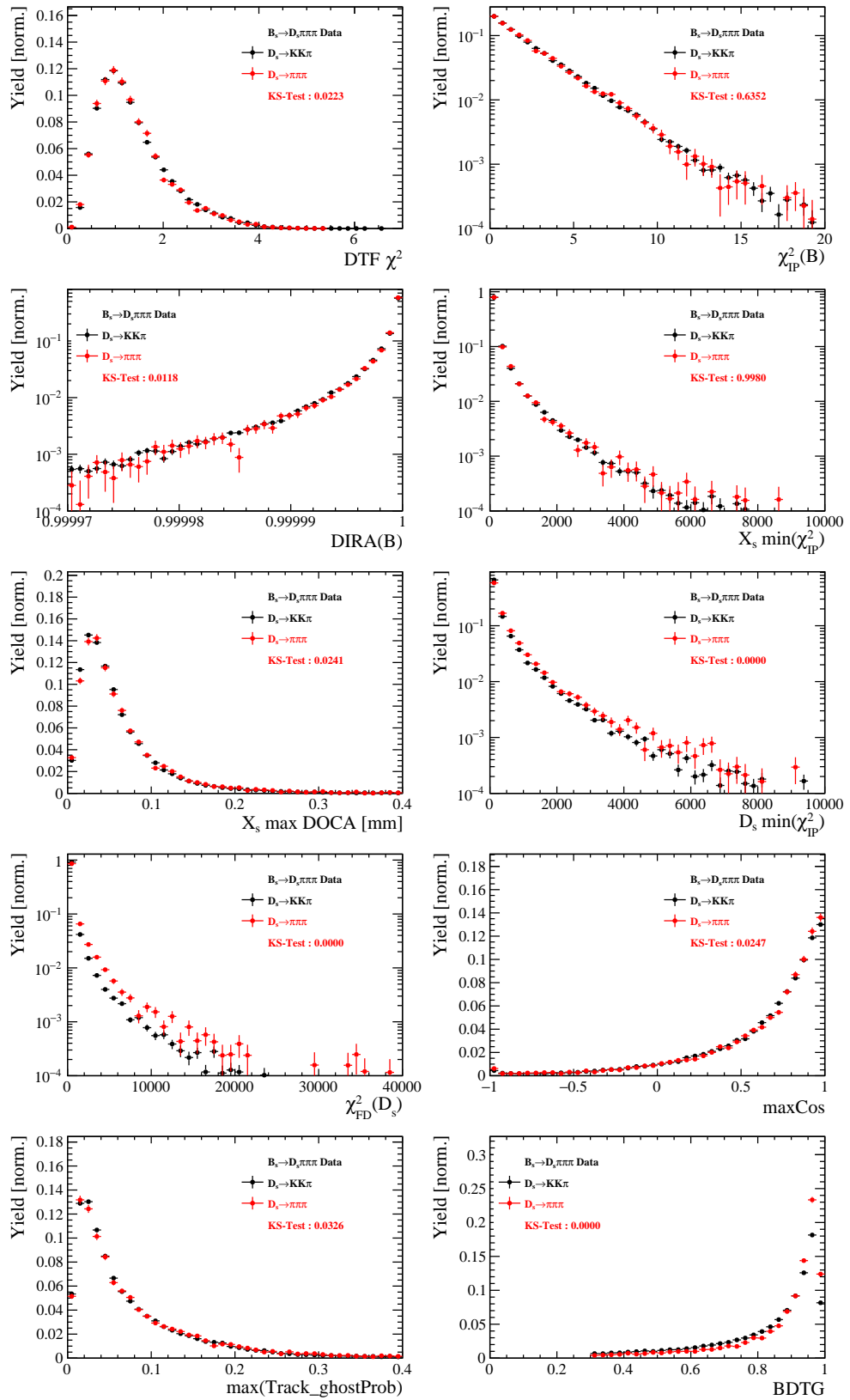


Figure C.6: Comparison of BDTG input variables and classifier response.

819 H.4 Comparison of trigger categories

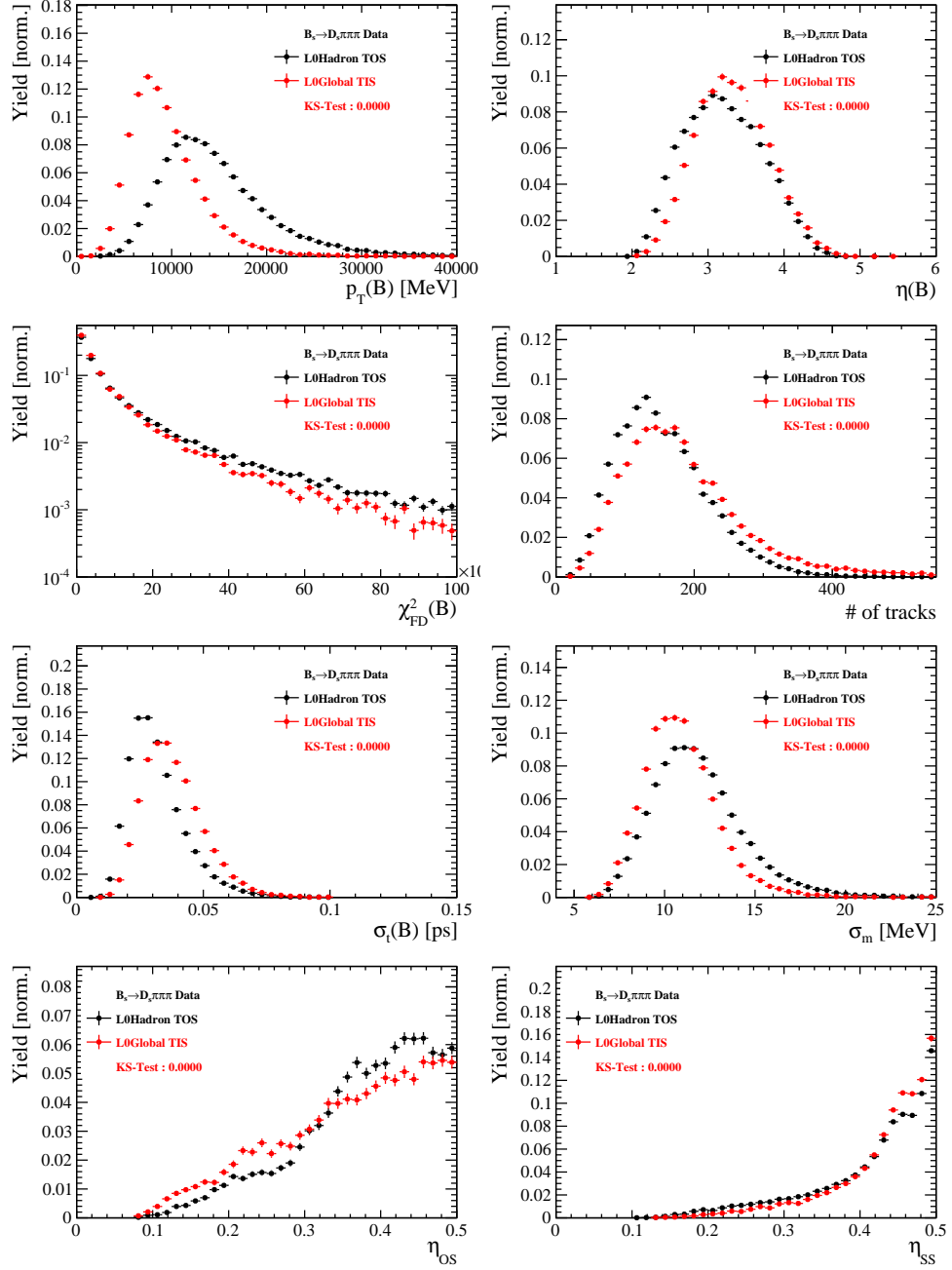


Figure C.7: Comparison of selected variables.

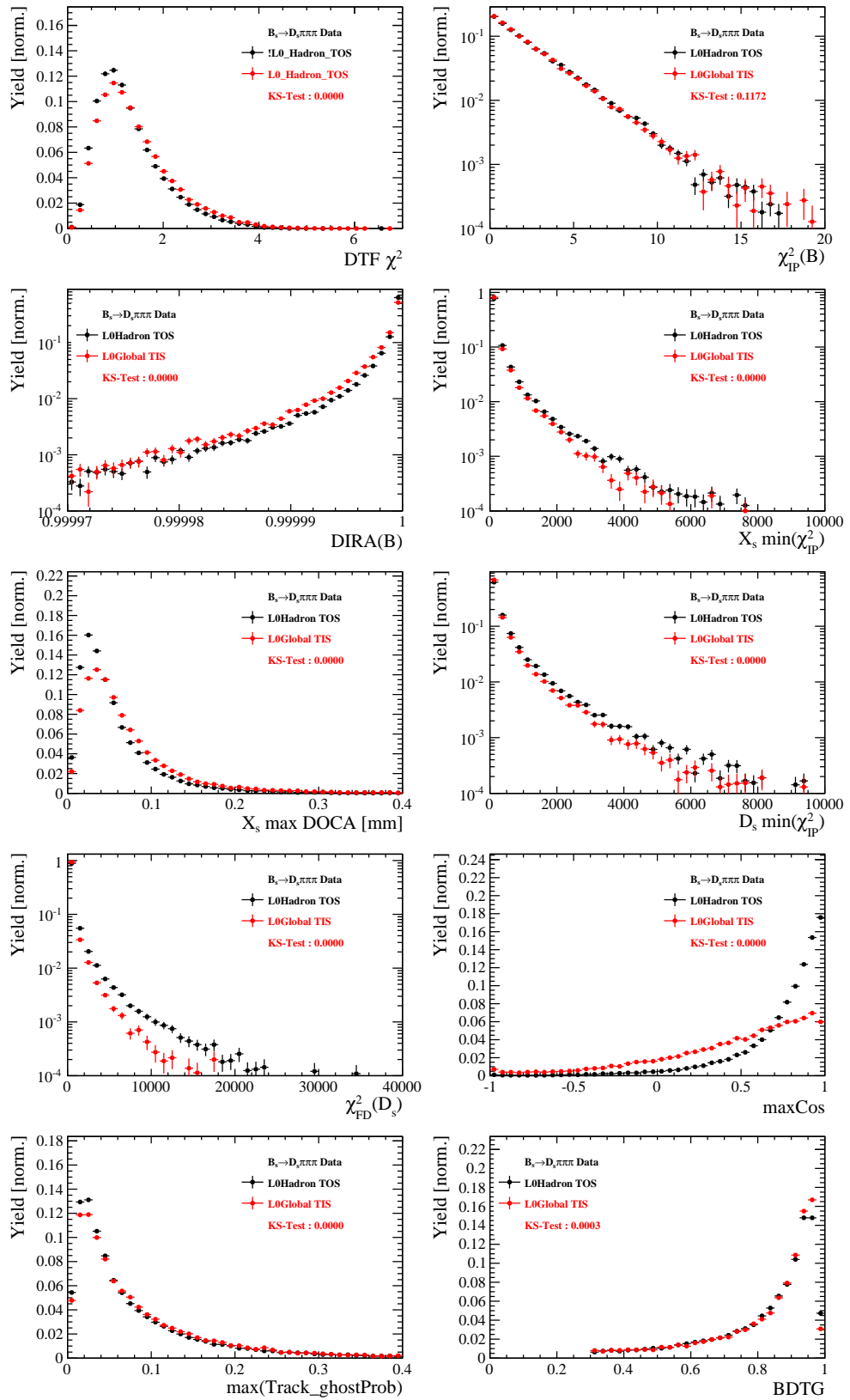


Figure C.8: Comparison of BDTG input variables and classifier response.

820 H.5 Comparison of B_s and B_d decays

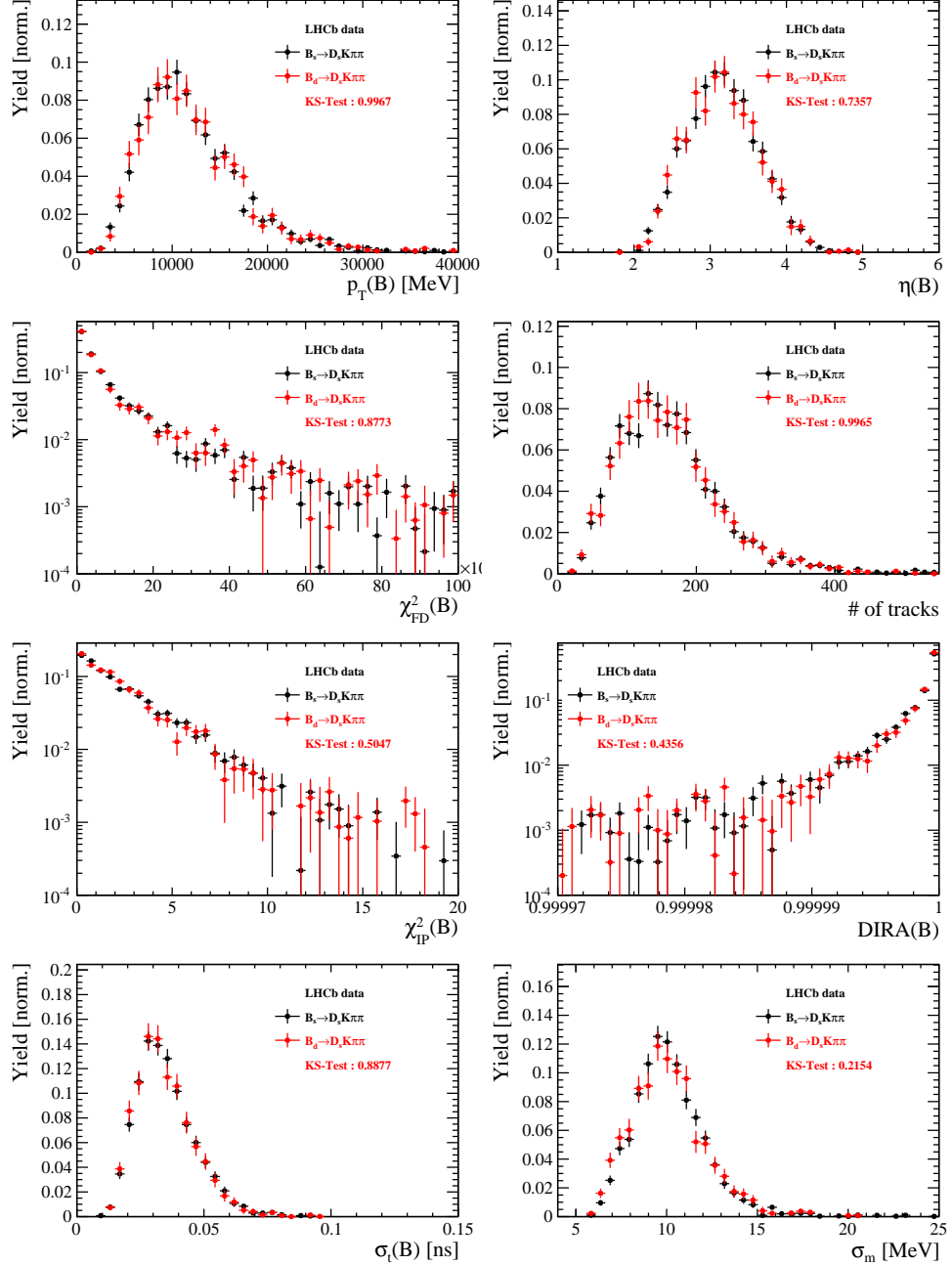


Figure C.9: Comparison of selected variables.

821 References

- 822 [1] R. Fleischer, *New strategies to obtain insights into CP violation through $B(s) \rightarrow D(s) \pi^\pm$, $D(s)^* \pi^\pm$, ... and $B(d) \rightarrow D \pi^\pm$, $D^* \pi^\pm$, ... decays*, Nucl. Phys. **B671** (2003) 459, [arXiv:hep-ph/0304027](#).
- 823 [2] K. De Bruyn *et al.*, *Exploring $B_s \rightarrow D_s^{(*)\pm} K^\mp$ Decays in the Presence of a Sizable Width Difference $\Delta\Gamma_s$* , Nucl. Phys. **B868** (2013) 351, [arXiv:1208.6463](#).
- 824 [3] S. Blusk, *First observations and measurements of the branching fractions for the decays $\bar{B}_s^0 \rightarrow D_s^+ K^- \pi^+ \pi^-$ and $\bar{B}^0 \rightarrow D_s^+ K^- \pi^+ \pi^-$* .
- 825 [4] LHCb, S. Blusk, *Measurement of the CP observables in $\bar{B}_s^0 \rightarrow D_s^+ K^-$ and first observation of $\bar{B}_{(s)}^0 \rightarrow D_s^+ K^- \pi^+ \pi^-$ and $\bar{B}_s^0 \rightarrow D_{s1}(2536)^+ \pi^-$* , 2012. [arXiv:1212.4180](#).
- 826 [5] M. E. Peskin and D. V. Schroeder, *An Introduction To Quantum Field Theory (Frontiers in Physics)*, Westview Press, 1995.
- 827 [6] E. Byckling and K. Kajantie, *Particle Kinematics*, John Wiley & Sons, 1973.
- 828 [7] S. Mandelstam, J. E. Paton, R. F. Peierls, and A. Q. Sarker, *Isobar approximation of production processes*, Annals of Physics **18** (1962), no. 2 198 .
- 829 [8] D. J. Herndon, P. Söding, and R. J. Cashmore, *Generalized isobar model formalism*, Phys. Rev. D **11** (1975) 3165.
- 830 [9] J. J. Brehm, *Unitarity and the isobar model: Two-body discontinuities*, Annals of Physics **108** (1977), no. 2 454 .
- 831 [10] F. von Hippel and C. Quigg, *Centrifugal-barrier effects in resonance partial decay widths, shapes, and production amplitudes*, Phys. Rev. D **5** (1972) 624.
- 832 [11] J. D. Jackson, *Remarks on the phenomenological analysis of resonances*, Il Nuovo Cimento Series 10 **34** (1964), no. 6 1644.
- 833 [12] Particle Data Group, C. Patrignani *et al.*, *Review of Particle Physics*, Chin. Phys. **C40** (2016), no. 10 100001.
- 834 [13] D. V. Bugg, *The mass of the σ pole*, Journal of Physics G Nuclear Physics **34** (2007) 151, [arXiv:hep-ph/0608081](#).
- 835 [14] G. J. Gounaris and J. J. Sakurai, *Finite-width corrections to the vector-meson-dominance prediction for $\rho \rightarrow e^+ e^-$* , Phys. Rev. Lett. **21** (1968) 244.
- 836 [15] S. M. Flatté, *Coupled-channel analysis of the $\pi\eta$ and KK systems near KK threshold*, Physics Letters B **63** (1976), no. 2 224 .
- 837 [16] BES Collaboration, M. Ablikim *et al.*, *Resonances in $J/\psi \rightarrow \phi\pi^+\pi^-$ and ϕK^+K^-* , Phys. Lett. **B607** (2005) 243, [arXiv:hep-ex/0411001](#).
- 838 [17] D. V. Bugg, *A study in depth of $f_0(1370)$* , Eur. Phys. J. **C52** (2007) 55, [arXiv:0706.1341](#).

- [856] [18] LHCb Collaboration, R. Aaij *et al.*, *Analysis of the resonant components in $B_s \rightarrow J/\psi \pi^+ \pi^-$* , Phys. Rev. **D86** (2012) 052006, [arXiv:1204.5643](#).
- [858] [19] C. Zemach, *Use of angular momentum tensors*, Phys. Rev. **140** (1965) B97.
- [859] [20] W. Rarita and J. Schwinger, *On a theory of particles with half integral spin*, Phys. Rev. **60** (1941) 61.
- [861] [21] S. U. Chung, *General formulation of covariant helicity-coupling amplitudes*, Phys. Rev. D **57** (1998) 431.
- [863] [22] B. S. Zou and D. V. Bugg, *Covariant tensor formalism for partial wave analyses of ψ decay to mesons*, Eur. Phys. J. **A16** (2003) 537, [arXiv:hep-ph/0211457](#).
- [865] [23] V. Filippini, A. Fontana, and A. Rotondi, *Covariant spin tensors in meson spectroscopy*, Phys. Rev. **D51** (1995) 2247.
- [867] [24] J.-J. Zhu, *Explicit expressions of spin wave functions*, [arXiv:hep-ph/9906250](#).
- [868] [25] P. d'Argent *et al.*, *Amplitude Analyses of $D^0 \rightarrow \pi^+ \pi^- \pi^+ \pi^-$ and $D^0 \rightarrow K^+ K^- \pi^+ \pi^-$ Decays*, JHEP **05** (2017) 143, [arXiv:1703.08505](#).
- [870] [26] M. Williams, *Numerical Object Oriented Quantum Field Theory Calculations*, Comput. Phys. Commun. **180** (2009) 1847, [arXiv:0805.2956](#).
- [872] [27] LHCb, R. Aaij *et al.*, *Studies of the resonance structure in $D^0 \rightarrow K^\mp \pi^\pm \pi^\pm \pi^\mp$ decays*, Submitted to: Eur. Phys. J. C (2017) [arXiv:1712.08609](#).
- [874] [28] D. J. Lange, *The EvtGen particle decay simulation package*, Nucl. Instrum. Meth. **A462** (2001) 152.
- [876] [29] *Gammacombo package*, 2014.
- [877] [30] A. Hoecker *et al.*, *TMVA: Toolkit for Multivariate Data Analysis*, PoS **ACAT** (2007) 040, [arXiv:physics/0703039](#).
- [879] [31] M. Pivk and F. R. Le Diberder, *sPlot: A statistical tool to unfold data distributions*, Nucl. Instrum. Meth. **A555** (2005) 356, [arXiv:physics/0402083](#).
- [881] [32] N. L. Johnson, *Systems of frequency curves generated by methods of translation*, Biometrika **36** (1949), no. 1/2 149.
- [883] [33] Particle Data Group, K. A. Olive *et al.*, *Review of Particle Physics*, Chin. Phys. **C38** (2014) 090001.
- [885] [34] LHCb, R. Aaij *et al.*, *A new algorithm for identifying the flavour of B_s^0 mesons at LHCb*, JINST **11** (2016), no. 05 P05010, [arXiv:1602.07252](#).
- [887] [35] LHCb collaboration, R. Aaij *et al.*, *Opposite-side flavour tagging of B mesons at the LHCb experiment*, Eur. Phys. J. **C72** (2012) 2022, [arXiv:1202.4979](#).

- [36] Heavy Flavor Averaging Group, Y. Amhis *et al.*, *Averages of b -hadron, c -hadron, and τ -lepton properties as of summer 2014*, arXiv:1412.7515, updated results and plots available at <http://www.slac.stanford.edu/xorg/hfag/>.
- [37] T. M. Karbach, G. Raven, and M. Schiller, *Decay time integrals in neutral meson mixing and their efficient evaluation*, arXiv:1407.0748.
- [38] LHCb collaboration, R. Aaij *et al.*, *LHCb detector performance*, Int. J. Mod. Phys. **A30** (2015) 1530022, arXiv:1412.6352.
- [39] LHCb, R. Aaij *et al.*, *Measurement of CP asymmetry in $B_s^0 \rightarrow D_s^\mp K^\pm$ decays*, Submitted to: JHEP (2017) arXiv:1712.07428.
- [40] LHCb, R. Aaij *et al.*, *Measurement of B^0 , B_s^0 , B^+ and Λ_b^0 production asymmetries in 7 and 8 TeV proton-proton collisions*, Phys. Lett. **B774** (2017) 139, arXiv:1703.08464.
- [41] H. Gordon, R. W. Lambert, J. van Tilburg, and M. Vesterinen, *A Measurement of the $K\pi$ Detection Asymmetry*, Tech. Rep. LHCb-INT-2012-027. CERN-LHCb-INT-2012-027, CERN, Geneva, Feb, 2013.
- [42] A. Davis *et al.*, *Measurement of the instrumental asymmetry for $K^- \pi^+$ -pairs at LHCb in Run 2*, Tech. Rep. LHCb-PUB-2018-004. CERN-LHCb-PUB-2018-004, CERN, Geneva, Mar, 2018.
- [43] I. I. Y. Bigi and H. Yamamoto, *Interference between Cabibbo allowed and doubly forbidden transitions in $D \rightarrow K(S)$, $K(L) + \pi$'s decays*, Phys. Lett. **B349** (1995) 363, arXiv:hep-ph/9502238.
- [44] B. Guegan, J. Hardin, J. Stevens, and M. Williams, *Model selection for amplitude analysis*, JINST **10** (2015), no. 09 P09002, arXiv:1505.05133.
- [45] R. Tibshirani, *Regression shrinkage and selection via the Lasso*, Journal of the Royal Statistical Society, Series B **58** (1994) 267.
- [46] G. Schwarz, *Estimating the dimension of a model*, Ann. Statist. **6** (1978) 461.
- [47] H. Akaike, *A new look at the statistical model identification*, IEEE Transactions on Automatic Control **19** (1974) 716.